SPATIAL DISTRIBUTION OF RIFT-RELATED FRACTURES: FIELD OBSERVATIONS, EXPERIMENTAL MODELING, AND INFLUENCE ON DRAINAGE NETWORKS

BY ROLF V. ACKERMANN

A Dissertation submitted to the

Graduate School - New Brunswick

Rutgers, The State University of New Jersey

in partial fulfillment of the requirements

for the degree of

Doctor of Philosophy

Graduate Program in Geological Sciences

Written under the direction of

Professor Roy W. Schlische

and approved by

Roy Schlische

Peter A. Roma

Michael R. Sidl

Martha Wahjach

New Brunswick, New Jersey

October, 1997

ABSTRACT OF THE THESIS

SPATIAL DISTRIBUTION OF RIFT-RELATED FRACTURES: FIELD OBSERVATIONS, EXPERIMENTAL MODELING, AND INFLUENCE ON DRAINAGE NETWORKS

by ROLF V. ACKERMANN

Dissertation Director:

Professor Roy W. Schlische

Knowledge of the spatial distribution of fractures within a rock volume is integral to our understanding of the processes of faulting, as well as the construction of effective fractured hydrocarbon and groundwater reservoir models. The mode of fracturing (mode I, mixed mode II/III, or mixed mode I/II/III) is governed by the strength of the rock, such that in interbedded lithologies of contrasting mechanical character an apparently predictable mechanical stratigraphy based on relative abundances of strong vs. weak minerals arises. If strain accommodation among the different lithologies is roughly comparable, and there is an absence of bedding-parallel detachments, a Mohr-Coulomb model for semi-coeval macroscopic failure can be constructed. The mechanical characteristics of the rocks not only govern the stratigraphic (vertical) distribution of structures, but also the lateral distribution. The distribution of neo-formed normal faults (shear or Mixed Mode II/III fractures) is governed by the long- and short-range elastic interaction of structures, giving rise to a correlated spatial distribution and power-law distribution of fault sizes. Mechanical layer thickness appears to be an important factor in these distributions, such that when the layer is exceeded, the stress-reduction shadows around normal faults (which are the means by which they elastically interact) cannot expand. This retards the long-range interaction of structures, suppressing spatial correlations. This in turn leads to a quasi-regular distribution

(spacing) of structures and exponential size distributions. All of these factors combine to produce the populations of fractures we see in outcrop and at the regional level, where fractures heavily influence and interact with the processes shaping the landscape. A fundamental mechanism for landscape evolution is fluvial denudation, commonly in the form of channel incision into bedrock. The mechanics and details of this process are not yet thoroughly understood, but it appears that the stream power of a channel is generally positively correlated with its ability to override the influence of the geologic structures in the underlying bedrock.

PREFACE

I know of no more encouraging fact than the unquestionable
ability of man to elevate himself by a concious endeavor.

- H.D. Thoreau

ACKNOWLEDGMENTS

First and foremost I would like to thank my parents, Rolf and Ginny Ackermann, for their their undying support and encouragement during the course of my education and in all facets of my life, and for being my #1 fans. I would also like to thank my advisor and friend, Roy W. Schlische, for his support and encouragement during all phases of the work presented here. I am very grateful for the intellectual freedom he has allowed me.

I am extremely appreciative to the Department of Geological Sciences and my Dissertation Committee (Michele A. Seidl, Martha O. Withjack, and Peter Rona) for their support during my time spent at Rutgers, as well as to the Structural Geology Team at Mobil Technology Company (Arlene Anderson, Gloria Eisenstadt, Peter Hennings, John Krueger, Kris Meisling, and Martha Withjack) for their insights, support, and encouragement during my time there. I am also appreciative to the Department of Geology at Dickinson College for teaching me the fundamentals of geology and for cultivating my curiosity and wonder.

Because science does not march forth without financial support, I would like to thank Mobil Technology Company for funding aspects of my research and for permitting me to utilize the scaled physical modeling facility at the Dallas Research Lab in Texas. This research was also generously supported by the Virginia Museum of Natural History, Sigma Xi, the Rutgers Research Council, and the Department of Geological Sciences at Rutgers University. Alison Lighthart at Tulane University kindly and expertly made numerous thin sections. George DeMarco kindly prepared a large rock sample for serial sectioning, generously donating a diamond blade in the process.

I greatly appreciate Greg Herman's assistance and patience while compiling, parsing, and formatting the stream channel file on the New Jersey Geological Survey Geographic Information System. Thank you to C.H. Gover and the Virginia Solite Corporation for their support of this and other research conducted at the Solite Quarry. Anu

Gupta, MaryAnn Malinconico, and Mike Viersma generously shared unpublished data. Mike Carr, Lois Johnson, Jeff Niemitz, Lina Patiño, and Gene Yogodzinski provided advice regarding the analytical geochemistry and x-ray diffraction; their guidance is greatly appreciated. Assistance from Charlie Wall and Selena Dixon was critical during the modeling process.

I would like to thank Gail Ashley, Karen Bemis, Jim Carpenter, Amy Clifton, Patience Cowie, Nancye Dawers, Gloria Eisenstadt, Nick Frasier, Mike Gross, Anu Gupta, Peter Hennings, Kris Meisling, Paul Olsen, Roy Schlische, Chris Scholz, Bruce Shaw, Michele Seidl, ShayMaria Silvestri, Mike Viersma, Martha Withjack, and Scott Young for field assistance and/or many engrossing and enlightening discussions regarding the features at Solite, fault population systematics, scaled physical modelling, bedrock channels, and the Mesozoic rift system in general. These discussions were not the only source of learning for me; I must thank the students in my Structural Geology and Field Geology classes for teaching me how to learn and share, and for allowing me to share in their wonder and discovery of geology.

Finally, I am grateful to my friends, old and new. You know who you are.

DEDICATION

This dissertation is dedicated to:

Rolf and Ginny Ackermann

My parents, whose undying support does not go unappreciated

Maria Krause-Ackermann

Meine liebe Oma

Dr. Henry Hanson

A mentor; a friend

TABLE OF CONTENTS

ABSTRACT OF THE THESIS ii

PREFACE iv

ACKNOWLEDGMENTS v

DEDICATION vii

TABLE OF CONTENTS viii

INTRODUCTION 1

CHAPTER ONE: FRACTURES AND MODERN DRAINAGE NETWORKS 3

SYNOPSIS 3

INTRODUCTION 4

FIELD SETTING 6

METHODS 7

RESULTS 10

DISCUSSION 13

SUMMARY 15

CHAPTER TWO: RIFT-RELATED STRUCTURES AT THE SOLITE QUARRY . . 31

SYNOPSIS 31

INTRODUCTION 32

GEOLOGIC SETTING 33

STRUCTURES PRESENT WITHIN THE QUARRY 34
Brittle/Discontinuous Deformation - Extension 34
Mode I Fractures 34
Hybrid Fractures 35
Shear Fractures (Small Normal Faults) 35
Ductile Deformation - Extension 38
Brittle/Ductile Deformation - Compression/Inversion 38
Neotectonic Structures 39
VERTICAL DISTRIBUTION OF STRUCTURES 39
LATERAL DISTRIBUTION OF STRUCTURES 44
Mode I 44
Small Normal Faults 45
SUMMARY AND CONCLUSIONS 46

CHAPTER THREE: ANTICLUSTERING OF SMALL NORMAL FAULTS 66
SYNOPSIS 66
INTRODUCTION 66
POPULATION SYSTEMATICS 67
DEFORMATION FIELDS AND STRESS-REDUCTION SHADOWS 71
DISCUSSION 73

CHAPTER FOUR: SYSTEMATICS OF AN EVOLVING FAULT POPULATION
. . . . 81
SYNOPSIS 81
INTRODUCTION 82
EXPERIMENTAL AND ANALYTICAL METHOD 83
RESULTS 88

DISCUSSION . . . 92

The shift from power-law to exponential distribution and mechanical layer thickness . . . 92

Fault generation zone width vs. mechanical layer thickness . . . 94

$\overline{L}$ vs. <L> . . . 95

Spatial distribution of fault centroids . . . 96

Modeling artifacts . . . 97

SUMMARY AND CONCLUSIONS . . . 99

REFERENCES CITED . . . 125

CURRICULUM VITAE . . . 135

INTRODUCTION

Fractures are ubiquitous within the Earth's crust, forming in response to a wide range of far and near-field forces and deformation mechanisms, from continental rifting to contracting lava as it cools. Fractures can be observed over a wide scale range, from micro-fractures in sandstones recovered in cores to continental lineaments. They provide pathways for fluid migration (e.g. groundwater and hydrocarbons) in the subsurface, and heavily influence the weathering of bedrock at the Earth's surface. Continental rift basins form as a result of far-field tension due to continental break-up. In effect, the border fault system of a rift basin is nothing more than a very large shear fracture. Our understanding of the evolution of continental rifts and the structures they contain is frequently hampered by poor exposure and complex basin architecture. The goal of this dissertation is to address four questions related to continental rifts, all of which are concerned with the spatial distribution of fractures in an extensional system.

Chapter One addresses the issue of how bedrock structures (primarily fractures) affect modern fluvial denudation of the basin fill of an ancient rift. It is generally accepted that bedrock structure plays a role in channel incision into bedrock, but until now there have been a limited number of studies that address the issue specifically and at the regional scale. Chapter One is a preliminary study of first-order, regional structural controls on modern drainages in the Newark rift basin on the east coast of North America, and will be submitted as a manuscript to the *Journal of Geology*. The ideas in Chapter One and the discussion of how fractures influence channel incision lead to the questions, "How did the fractures form, and why are they distributed as they are?" Chapters Two through Four systematically address these questions.

Chapter Two examines the brittle deformation of a sequence of sedimentary rocks in the Danville rift basin, which belongs to the same rift system as the Newark basin. The field locality is at the Solite Quarry, and provides a comprehensive suite of neo-formed and re-activated rift-related brittle structures. The analysis focuses on the vertical (stratigraphic) distribution of these structures, and reveals that mineralogy is a key factor in their formation, which must have occurred under a specific set of conditions. An expanded version of Chapter Two has been submitted in manuscript form to the *Triassic-Jurassic Rift Basin Geoscience Special Volume* (P. LeTourneau and P. Olsen, eds., Columbia University Press). Chapter Three takes a specific subset of the features (small neo-formed normal faults) described in Chapter Two and provides a rigorous analysis of their spatial distribution within the rock volume. The results of the analysis have important implications for the distribution of stresses in the volume surrounding a fault, the elastic interaction of faults with each other, and the temporal evolution of neo-formed normal fault systems. Chapter Three will be published in the journal *Geology* in late 1997 or early 1998.

Chapter Four will be submitted to the *Journal of Structural Geology*, and takes up the question of the temporal evolution of neo-formed normal fault systems using scaled physical (wet clay) models. The model discussed is of simple extension of a single mechanically homogeneous brittle layer, and is analyzed using fault population systematics. Fault population systematics integrates data on strain accommodation, fault geometries, scaling relationships, and the size and spatial distributions of faults. The systematics of a structural system reflect its framework and history, both of which are crucial to petroleum and groundwater investigations; studies of fault populations have recently received considerable attention (see Cowie et al., 1996). Chapter Four brings the dissertation full circle by examining the spatial distribution of fractures from the onset of deformation to structural maturity.

CHAPTER ONE: REGIONAL STRUCTURAL CONTROLS ON MODERN DRAINAGE MORPHOLOGIES IN THE MESOZOIC NEWARK BASIN OF EASTERN NORTH AMERICA

SYNOPSIS

The geometries and forms of drainage networks in the (Mesozoic) Newark basin on the east coast of North America reflect the underlying geologic structures. The Newark basin lies on a passive margin in a temperate climate, and is drained by streams floored with bedrock and a veneer of bedrock chips and slabs. The goal of this study is to determine if there is a first-order relationship between drainage network form and geologic structure. The data suggest that there is a general correlation between stream order and structural controls, such that lower order streams tend to be moderately to strongly influenced by geologic structures, whereas high order streams (high values of stream power) tend to override their influence. The influence can be muted by factors such as thick overburden (e.g. glacial deposits) and structural complexity.

INTRODUCTION

A fundamental rate-limiting process in landscape evolution is the incision of stream channels into bedrock (e.g. Seidl et al., 1997). Hillslopes respond to bedrock channel incision in terms of both form and process (e.g. Burbank et al., 1996). An important issue is the role of structural and lithologic controls on channel morphology and the geometry of drainage networks. Although it is generally agreed that geologic structure is important, it is not yet clear what control that the underlying bedrock structure does or does not exert on channel form and process (e.g. Harden, 1985; Horton, 1945; Howard, 1967; Miller, 1991; Schumm et al., 1987; Seidl and Dietrich, 1992; Wolman et al., 1990; Wohl, 1990; 1992; 1993; Wohl et al., 1994).

Rock strength or resistance to erosion can determine flow patterns, channel morphology, knickpoint migration, and channel incision (e.g. Howard and Kerby, 1983; Baker, 1984; and Wohl et al., 1994). Part of the Nelson River valley in Canada follows a topographic break or trough in the raised arc of the Precambrian shield surrounding Hudson Bay (Wolman et al., 1990). The St. Lawrence River reflects hydrologic control by the Great Lakes, but within a geologic path determined by the contact between crystalline and sedimentary rocks (Wolman et al., 1990). Marked differences in channel form and the dimensions of meanders have been attributed to differences in the relative erodability of bedrock (e.g. Abrahams, 1985; Braun, 1983). Others have concluded that rock strength plays a minimal role in determining channel form (e.g. Harden, 1985; Miller, 1991; Seidl and Dietrich, 1992; Wohl, 1993).

Bedrock-influenced or controlled stream channel morphology has been found by several workers to be related to the structure of the rocks. Miller (1991) correlated channel gradient and bedding plane orientation (relative to flow) to knickpoints, and Schumm et al. (1987) found that sinuosity increases when a stream flows up-the-dip of the underlying bedrock. Harden (1985) determined that bedrock structure was the only significant factor that discriminated between straight and meandering reaches in the central Colorado plateau.

Fractures in bedrock are common to most all geologic settings, and seem to exert varying degrees of influence on stream channels. There are joint controlled drainage patterns (e.g. Baker, 1984; Howard, 1967; Myrick et al., 1988; Nelson, 1988; Yelderman et al., 1988; Zernitz, 1932), and fractures in bedrock have been found to control stream channel and/or valley orientation (e.g. Fisher et al., 1988; Johnson, 1988; Steele et al., 1988; Canavan and Kochel, 1990). Wohl (1990) and Miller (1991) concluded that joints can be conducive to plucking and quarrying by stream flows when oriented normal to flow, and fracturing may be conducive to erosion and knickpoint formation (Wohl et al., 1994).

Pools and riffles can be associated with areas where a river channel crosses local and regional fracture zones (Dolan et al., 1978). Other studies have concluded that bedrock structure plays a minimal, if any, role in bedrock-influenced or controlled channel morphology (e.g. Seidl and Dietrich, 1992; Wohl, 1993).

There are clearly a variety of observations about the effects of geologic structure on bedrock channel form and erosional processes. Until now, most studies have focused in detail on one channel or a small drainage network of channels (e.g. Seidl and Dietrich, 1992; Seidl et al., 1994; Wohl, 1990; 1992; 1993; Wohl et al., 1994), and most of the work has been in either fairly arid regions (e.g. Wohl, 1993, 1994), or in tectonically active areas (e.g. Seidl and Dietrich, 1992; Seidl et al., 1994; Burbank et al., 1996), where denudation rates can be assessed. There have been very few regional studies (e.g. Horton, 1945; Miller, 1991) that address the question systematically from a structural geology point of view, in such a way that local structural perturbations are evened out. Hence, the question of structural controls at the regional level remains relatively open and frustrating. Since drainage network form can be used as a proxy for channel form, a regional analysis of the interplay between bedrock architecture and drainage networks would prove useful for studies of landscape evolution (e.g. Burbank et al., 1996; Seidl et al., 1997). In addition, drainage networks are a convenient starting point for regional studies. Drainage networks have been studied as a proxy for the underlying geology since the time of Playfair, as well as in modern quantitative work (e.g. Horten, 1945; Howard, 1967).

This chapter approaches the problem of structural and lithologic controls on modern drainage networks within the Triassic-Jurassic Newark rift basin of New Jersey from a structural geology perspective. A comparison of drainage morphology with local structures shows that in most parts of the basin, the stream channels generally parallel the underlying structures in a systematic manner. Horton (1945) used several drainages in the Newark basin to derive empirical relationships between channel length, number of streams, and stream order. Horton (1945) then went on to show how geological controls affect these relationships. This basin is ideal for this investigation not only because of Horton's previous work, but also because (1) maps of the streams (coded by stream order) are available in digital form; (2) the stratigraphy and structural geology of the basin is known in great detail; and (3) the basin can be subdivided into a number of domains, the boundaries of which are objectively delineated on the basis of stratigraphy and uniformity of geologic structure.

FIELD SETTING

This study focuses on the modern drainages of the Piedmont physiographic province (known locally as the Triassic-Jurassic lowlands) in New Jersey, USA. The province is defined by the structural and stratigraphic boundaries of the Newark rift basin, which is well understood in terms of both its structure and stratigraphy (e.g. Olsen et al., 1996; Schlische, 1992, 1993). The Newark basin is one of a series of ancient half graben rifts on the east coast of North America (Figure 1.1), which formed in response of the separation of Africa and North America during the Mesozoic break-up of the Pangean landmass. These basins have complex internal architecture that stems from the processes of fault growth, linkage, and overall basin and crustal evolution (e.g. Anders and Schlische, 1994; Olsen et al., 1996; Schlische, 1992). Because the study area is located in a geologic setting structurally characterized by the term "basin", in this chapter "basin" will refer to the ancient rift structure (Newark basin), its sedimentary fill, and the geologic structures expressed in that fill, not to any modern topographic or hydrologic division.

The Newark basin is bounded by a southeast-dipping normal fault system (border fault system) on its northwestern margin, and contains a number of southeast-dipping intrabasinal normal faults (Figure 1.1). The basin fill generally dips gently to the northwest, consisting of sandstones, well-bedded mudstones, massive siltstones, and shales (Stockton, Lockatong, Passaic, Feltville, Towaco, and Boonton Formations). These sedimentary facies are interspersed with continental flood basalts (Jacksonwald, Orange Mountain, Hook Mountain, and Preakness Basalts) in the upper third of the section (Schlische, 1992). Differential weathering of these lithologies has given rise to a topography consisting of a broad lowland interrupted by long northeast-striking ridges (deepest water facies and basalts) and uplands (basalts). The strike-ridges express a series of longitudinal synclines and anticlines that formed due to differential subsidence of hanging wall blocks on a segmented border fault system in conjunction with syn-rift deposition (Schlische, 1992; 1993). Bedding generally strikes to the northeast, with local variations to the northwest and southeast in folded areas. Differential regional hangingwall subsidence also produced generally steeper dips in older units and those proximal to the border fault system (Schlische, 1992; 1993). In addition to being well-understood, the Newark basin provides the additional benefit of being located on a passive margin, where complications due to regional and local uplift are avoided.

The soil mantle in the Newark basin is generally thin, although it is generally thicker in areas affected by late Wisconsinan glaciation. Streams in the Newark basin generally flow over bedrock covered with a thin veneer of bedrock chips and slabs. The channels are floored with bedrock. The base of the banks is comprised of bedrock overlain by soils derived directly from the underlying bedrock, in turn overlain by floodplain deposits. Hence these channels fall somewhere in the middle of the bedrock-alluvial channel continuum (e.g. Howard, 1980).

METHODS

The basin was subdivided into structural domains based on the types of structures present and on the lithology (Figure 1.1) using 1:125,000 (Lyttle and Epstein, 1987) and 1:24,000 (Olsen et al., 1996) geologic maps. In addition, domains were subdivided based on the southern ice limit of late Wisconsinan glaciation (Figures 1.1 & 1.2). Table 1.1 summarizes the domain definitions. General structural data (strike of bedding, trends of fold axes) were acquired from the same geologic maps. Data on fracture sets were compiled from various local studies within the basin (Schlische, 1990; Jones; 1994, Herman, 1996; Muszala, 1996; Orabone, 1997), as well as from the Borehole Televiewer Logs (BHTV) acquired during the Newark Basin Drilling Project (Olsen et al., 1996). The arrows representing fracture orientations in Figures 1.3-1.9 represent the dominant fracture set, derived from rose diagrams of fracture data from the aforementioned sources. Additional subordinate fracture sets are presented in Figures 1.3-1.9 as shorter arrows. This chapter focuses on six of the eighteen domains shown in Figure 1.1c; the results for the analyses of all eighteen domains are summarized in Table 1.1. These six domains are the best examples from the basin, representing a range of structures, lithologies, positions within the basin, and degrees of correlation with the underlying bedrock structure. One of the domains is subdivided into regions affected and unaffected by late Wisconsinan galaciation.

Drainage networks were analyzed using a digital data set from the New Jersey Geologic Survey Geographic Information System. The streams were digitized and coded with their Strahler order by the New Jersey Geologic Survey from 1:24,000 7.5' United States Geological Survey topographic quadrangles. The geographic boundaries of the Newark basin were used to parse the state stream channel data set, and the file (Figure 1.2) was saved in a format compatible with desktop computer-based technical drawing software (Canvas 3.5.4). Stream channels were objectively divided into headwaters to confluence and confluence to confluence segments (Figure 1.3). Each segment was assigned a flow vector, where the downstream direction is the azimuth component of the vector and channel segment length (*L*) is the length component. The Strahler order coding was retained during the data analysis. The length component for each vector was normalized (L_n) by the sum of the segments of a given order in a given domain:

$$L_{\mathrm{n}} = \frac{L}{\Sigma L_{\zeta}}$$

where ζ is the Strahler order. This permits the orientation data to be presented on polar diagrams as shown in Figure 1.3, so that relatively short channel segments are not overshadowed by substantially longer segments. Anthropogenic features such as canals (e.g. the Raritan canal) and channelization for navigation (e.g. the Meadowlands) and drainage (e.g. the Watchungs) were omitted from the analysis.

After we present the results of our analyses, we will suggest a generalized correlation between stream order and the influence of geologic structure on channel form. Since these channels are primarily floored with bedrock, we will utilize a stream power-dependent erosion law for bedrock incision developed by Seidl et al. (1994) based on a drainage area (*A*) slope (*S*) product:

$$-\frac{\delta z}{\delta t} = kA^m S^n \approx \omega$$

where *z* is the elevation of the channel above some datum, *t* is time, *A* is drainage area, ω is stream power, and *k*, *m*, and *n* are empirical constants. This assumes that bedrock incision occurs primarily during low-frequency high-magnitude discharge events, and that such events scale positively with drainage area (*A*). As a general rule, higher order streams have larger drainage areas and thus generally higher values of stream power and erosive capacity. Howard et al. (1994) noted that erosion in bedrock channels depends on the capacity to scour or pluck bedrock, which in turn is often a function of drainage area and channel slope. Hence, we will use Strahler order as a proxy for stream power:

$$\zeta \propto A \propto \omega$$

This generalization facilitates this regional scale study, and assumes that there is little variation in channel slope. Streams with higher values of ζ will generally have lower values of S; our method assumes that an increase in A due to increasing ζ offsets this; this assumption is clearly not entirely valid, but is necessary during a first-pass regional analysis such as this. The generalization also assumes that all second order streams will have a greater value of ω than all first order streams. This is clearly not the case: two extremely small first order channels may confluence to form a small second order stream, which will have less ω than a larger first order stream with a larger drainage area (A). Finally, we will assume that streams take the route to base level that conserves the most energy.

RESULTS

A cursory examination of the map in Figure 1.2 reveals a range of drainage patterns, from dendritic to trellis to radial, and hybrids thereof (e.g. Horton, 1945; Howard, 1967; Zernitz, 1932). When this map is compared to the geologic map of the Newark basin in Figure 1.1, a first-order correlation between drainage networks and geologic structures is readily apparent. For example, the streams in Domain 16a follow the folds defined by basalt flows very closely. Similarly apparent relationships can be found in Domains 3, 7, 9, 10, and 16b.

A detailed analysis of Domain 3 is presented in Figure 1.4. This domain is underlain by uniformly striking (~060°) Lockatong formation (gray to black shales), and is bounded to the southwest by the Delaware River. Proximity to the river results in a fair number of channels with flow vectors to the southwest. The drainage pattern is best described as trellis. There is a strong correlation between the strike of bedding and first order channel flow vectors. The relationship between second order channels and bedding or the dominant (~045°) fracture set is ambiguous. Third order channels do not show good correlation with bedding or fractures, although the map pattern suggests that they may be exploiting the subordinate fracture set (150°).

Domain 7 is also underlain by the Lockatong Formation, but here the rocks are folded into a gently plunging open syncline with a west-trending fold axis (Figures 1.1 & 1.5). The Flemington fault forms the southeastern boundary of Domain 7, and serves as a drainage divide along its southern end (Figure 1.2). The hybrid dendritic-trellis drainage pattern in Domain 7 (Figures 1.3 & 1.5) mirrors the geometry of the fold (Figure 1.1), although first order streams show limited correlation with the strike of bedding (fold limbs) (Figure 1.5). Second order streams show some correlation with the limbs of the fold; they may also be exploiting the fractures. There are a limited number of third and fourth order channels, and they show weak correlation with the geologic structures.

The drainage pattern in Domain 12 is dendritic, underlain by Lockatong Formation uniformly striking ~060° (Figures 1.1 & 1.6). The Delaware River forms the southwestern boundary of this domain. First and second order streams show moderately good correlation with bedding and the fracture sets present, although it is difficult to determine if bedding or fractures are the dominant control, since they are subparallel. Many third order channels show close correlation with fractures, although there is a subset of channels orthogonal to the regional fracture sets. There are not any fourth order channels in this domain, and fifth order channels do not show any correlation with bedrock structure.

Domain 15 is the most structurally complex domain studied, and is located in the interior of the basin, bounded to the west by the Hopewell Fault, and is characterized by a dendritic drainage pattern. Even though a generalized bedding orientation is given in Figure 1.7, this region of the basin is characterized by highly variable bedding strikes. Fracture orientations are not readily available for this domain, although the regionally dominant northeast-striking set is most certainly present. Flow vectors for first order channels span the compass with no apparent uniform trend (Figure 1.7). Second, third, and fourth order channels show similar variability, whereas fifth order channels generally show a preferred flow vector subparallel to bedding, oriented slightly up-dip. Sixth order streams show a similar orientation, but are generally orthogonal to fifth order streams.

The southern limit of late Wisconsinan glaciation separates Domains 16a and 16b. Domain 16a lies to the south of the ice limit and Domain 16b lies to the north. Both are underlain by folded basalt flows and Jurassic strata, and contain intrabasinal faults. As is the case with Domain 15, fracture data are not readily available for these domains. The primary difference between Domains 16a and 16b is that sedimentary cover in Domain 16b is primarily glacially derived and thicker than that of Domain 16a. In both domains the basalt flows form major drainage divides due to differential weathering, and their influence can be seen in the drainage patterns. For example, there are streams caught between the Preakness and Hook Mountain Basalts (Figures 1.1 & 1.2), flowing northward on the Towaco Formation, following the strike of bedding closely and outlining the folds. In Domain 16a the two dominant bedding orientations (Figure 1.8) are defined by the limbs of a large syncline with a north-northwest-trending fold axis. These structures and the strong differential weathering make this a complex region; this is reflected in the combination of dendritic, annular, and trellis drainage patterns. Flow vectors of first order streams (Figure 1.8) show a large amount of scatter with no apparent preferred orientation. However, a rose diagram of flow azimuths (Figure 1.8) shows that there are more channels that flow in the direction of ~190°-200°; this is subparallel to the fold hinge. Second order channel flow vectors show similar scatter, and the rose diagram of azimuths also reveals a subtle preferred orientation, in this case to the south-southwest, subparallel to the fold axis.

Third, fourth, and fifth order channels also show substantial scatter, whereas sixth order channels show a strong preferred northeast flow direction. This is parallel to the strike of bedding on the southeastern limb, with drainages caught between basalt ridges flowing generally northward into Domain 16b.

The most marked difference between Domains 16a and 16b is that even though they are underlain by the same rocks and types of structures, and the drainages are affected by basalt ridges, (generally following the folds), the generally dendritic drainage pattern in Domain 16b is simpler than the drainage pattern in Domain 16a. First and second order channels do not show a preferred flow azimuth, whereas a slight majority of third order channels flow subparallel to the fold axes. Fourth order channels do not appear to have a preferred flow direction. Fifth order channels flow subparallel to bedding strike and fold axes, with sixth order channels often flowing orthogonal to this.

DISCUSSION

Table 1.1 summarizes the results for all of the domains analyzed. Structurally complex domains and those affected by glaciation generally have dendritic drainage patterns, whereas structurally simpler domains exhibit drainage patterns (trellis, annular, hybrids of dendritic) that reflect the underlying bedrock geology. Differential weathering is also apparent in the drainage patterns, with the streams broadly outlining the structures (folds), similar to the Nelson and St Lawrence Rivers (Wolman et al., 1990). These relationships are difficult to quantify on a regional scale, but are readily apparent when the stream map in Figure 1.2 is compared with the geologic map in Figure 1.1. In detail, the influence of structures on channel orientations is more difficult to extract. The data in Table 1.1 show a wide degree of variability and it is difficult to find consistent trends, indicating that there is not a simple correlation between drainage network form and geologic structures.

In general, first order channels show a wide amount of scatter, although Domains 3, 4, 10, and 13 show strong correlations with bedding strike. There is also substantial variability in 2nd order streams, with Domains 1, 3, 7, 8, and 16a showing strong correlations with fractures. Third order streams generally show modest correlations with structures, and are parallel or subparallel (within 15°) to fractures in Domains 1, 2, 3, 4, 12, and 14a. Third order streams parallel bedding in Domain 14a, and fold axes in Domain 16b. Fourth order streams also show modest correlations, and are parallel or subparallel to fractures in Domains 1, 7, 8, 11, and 14a. They are also parallel or subparallel to bedding in 9 and 14a. Fifth order streams show weak to no correlations with structures, with the exceptions of Domains 8 (bedding) and 14b (bedding, joints). Sixth order streams show weak to no correlations with structures.

The general trend that can be gleaned from these data is as follows: First order streams do not consistently correlate with geologic structure. Mid-order streams (2 - 4) usually show some correlation with geologic structure. High order (5 - 6) streams infrequently correlate with the underlying structure. These are broad generalities, exceptions to which are readily available in Table 1.1. Structurally complex domains show weak to no correlations, with the exception of 1st order streams in Domain 16b. The glaciated-unglaciated subdivisions of Domains 14 and 16 are structurally very similar, and show generally the same patterns of flow vectors. Correlations between channels and structures appear to be masked or not present in the formerly glaciated domains (14b & 16b).

We thus suggest the following "rule of thumb": Low order streams will not correlate with the underlying bedrock structure if they are caught in the sedimentary cover (they are free to meander). Larger low order streams and mid order streams will have enough power to cut through the relatively thin sedimentary cover in the Newark basin and flow primarily over bedrock. Hence, they will be influenced by the underlying structures. For example, less energy is expended by flowing parallel to joints than accross them: structures normal to flow are conducive to quarrying (e.g. Wohl, 1990; Miller, 1991), which in turn expends more energy. Higher order channels likely have enough power to override structural controls, cutting across structures in order to take the route to base level that conserves the most energy. The degree of influence will depend on thickness of the overburden (e.g. glaciated vs. unglaciated), and complexity of the underlying structures, both of which appear to moderate the influence of the underlying structures in the Newark basin. In areas affected by late Wisconsinan glaciation, streams have to incise deeper into the sedimentary cover before they can flow over bedrock. The bedrock in structurally complex areas may be substantially weaker than in simple areas due to additive effects, e.g. subsidence, folding, fracturing, contact metamorphism, and differential weathering vs. subsidence and fracturing. The drainage patterns in both glaciated and complex areas tend to be dendritic, perhaps implying that these materials respond to fluvial erosion as relatively homogenous media.

The data suggest that there is indeed a first-order correlation between drainage patterns and geologic structures, and that more detailed data are required to more clearly define what the relationships are. It may be as simple as integrating channel segment slopes or drainage areas or overburden thickness (or some combination thereof) into the flow vector analysis. In structurally complex areas, it may be necessary to undertake detailed studies of the structures underlying a few representative channels.

SUMMARY

The data collected in this regional study suggest that there is a first-order relationship between drainage network morphology and geologic structure within the Newark basin beyond that readily apparent from maps. Stream order appears to be related to the influence of the underlying structures on drainage patterns based on a stream power-dependent erosion law: Low order streams caught in overburden will not follow the structures, whereas mid-order streams flowing over bedrock will exhibit varying degrees of conformity to structures. High order streams appear to have enough stream power to override the influence of bedrock structure. These relationships break down in areas of thick overburden (glacial sediments) and complex geologic structure. It is not apparent if these relationships will hold in tectonically active regions or in areas with structural histories different or more complex than that of the Newark basin. It is clear from the data and the observations of other workers that more study both in the Newark basin and in other structural settings is needed to better understand the control that geologic structure exerts on fluvial form and process, as well as landscape evolution.

Table 1: Summary of the structural domains used in this study, including basis for delineation, drainage patterns, and correlations between stream orders and underlying bedrock structure.

Domain/ Complexity	Formation	Structure	Drainage Pattern	1st order	2nd order	3rd order	4th order	5th order	6th order
1 - Moderate	Passaic	Folded, bounded to NW by border fault	Dendritic-Trellis	Fractures (weak)	Bedding	Bedding, Fold axis	Bedding	N/A	N/A
2 - Simple	Passaic	Uniform strike	Insuff. Data	Bedding, Fractures	inconclusive	inconclusive	N/A	inconclusive	N/A
3 - Simple	Lockatong	Uniform Strike	Trellis	Bedding	inconclusive	inconclusive, fractures?	N/A	N/A	N/A
4 - Simple	Stockton	Uniform Strike	Trellis	Bedding	inconclusive	Fractures	N/A	N/A	N/A
5 - Complex	Stockton	Fault bounded horse	Insuff. Data	Insuff. Data	Insuff. Data	Insuff. Data	Insuff. Data	Insuff. Data	Insuff. Data
6 - Complex	Passaic	Complex, mostly adjacent to border fault, intrabasinal faults, bounded to NW by Flemington Fault, SW by central splay of the Flem. fault	Dendritic	None	None	Fractures (weak)	inconclusive	inconclusive	N/A
7 - Moderate	Lockatong	Folded, bounded to SE by Flemington Fault	Dendritic-Trellis	Bedding (limited)	Bedding, fractures (weak)	inconclusive	inconclusive	N/A	N/A
8 - Complex	Stockton	Folded, bounded to North by border fault	Dendritic	None	Fractures	None	Fractures	Bedding (weak)	N/A
9 - Simple	Passaic	Uniform strike, bounded to NW by central splay of the Flemington fault	Dendritic-Trellis	Fractures (weak), Bedding (weak)	inconclusive	inconclusive	Bedding (very weak)	inconclusive	inconclusive
10 - Simple	Mostly Lockatong	Uniform strike, bounded to NW by diabase, SE by Hopewell fault	Dendritic-Trellis	Bedding, Fractures	None	None	N/A	N/A	N/A

Domain/ Complexity	Forma-tion	Structure	Drainage Pattern	1st order	2nd order	3rd order	4th order	5th order	6th order
11 - Simple	Mostly Passaic	Uniform strike, bounded to NE by diabase, North by Hopewell fault	Dendritic-Trellis	Fractures	inconclusive	None	inconclu-sive	N/A	N/A
12 - Moderate	Mostly Lockatong	Uniform strike, intrabasinal faults, bounded to North by diabase	Dendritic	Bedding, fractures	Bedding, Fractures Fractures		N/A	None	N/A
13 - Simple	Mostly Stockton	Uniform strike	Dendritic	Bedding	Bedding (weak)	None	inconclu-sive	N/A	N/A
14a - Simple	Passaic	Uniform strike, partly bounded to NW by Hopewell fault, *unglaciated*	Dendritic-Trellis	Fractures	None	Bedding, Fractures (weak)	Fractures (?)	Bed-ding, Frac-tures (?)	None
14b - Simple	Passaic	Relatively uniform strike, very gentle syncline to the North, intrabasinal faults, *glaciated*	Dendritic	Bedding (weak)	inconclusive	Bedding (weak)	None	Frac-tures	Frac-tures (weak)
15 - Complex	Passaic	Structurally complex basin interior, variable strikes, bounded to West and North by Hopewell fault system	Dendritic	inconclusive, regional fractures?	inconclusive	inconclusive	inconclu-sive	bed-ding, slightly updip	bed-ding, slightly updip
16a - Complex	Basalt & Jurassic	Strong differential weathering of igneous and sedimentary rocks, large, tight syncline, intrabasinal faults, *unglaciated*	Dendritic-annular-trellis	Bedding (weak)	Bedding (weak)	inconclusive	inconclu-sive	incon-clusive	bedding (strike ridges)
16b - Complex	Basalt & Jurassic	Strong differential weathering of igneous and sedimentary rocks, tight anticline-syncline pair, intrabasinal faults, *glaciated*	Dendritic	None	None	Fold axis	Fold axis	Bed-ding, fold axes	None

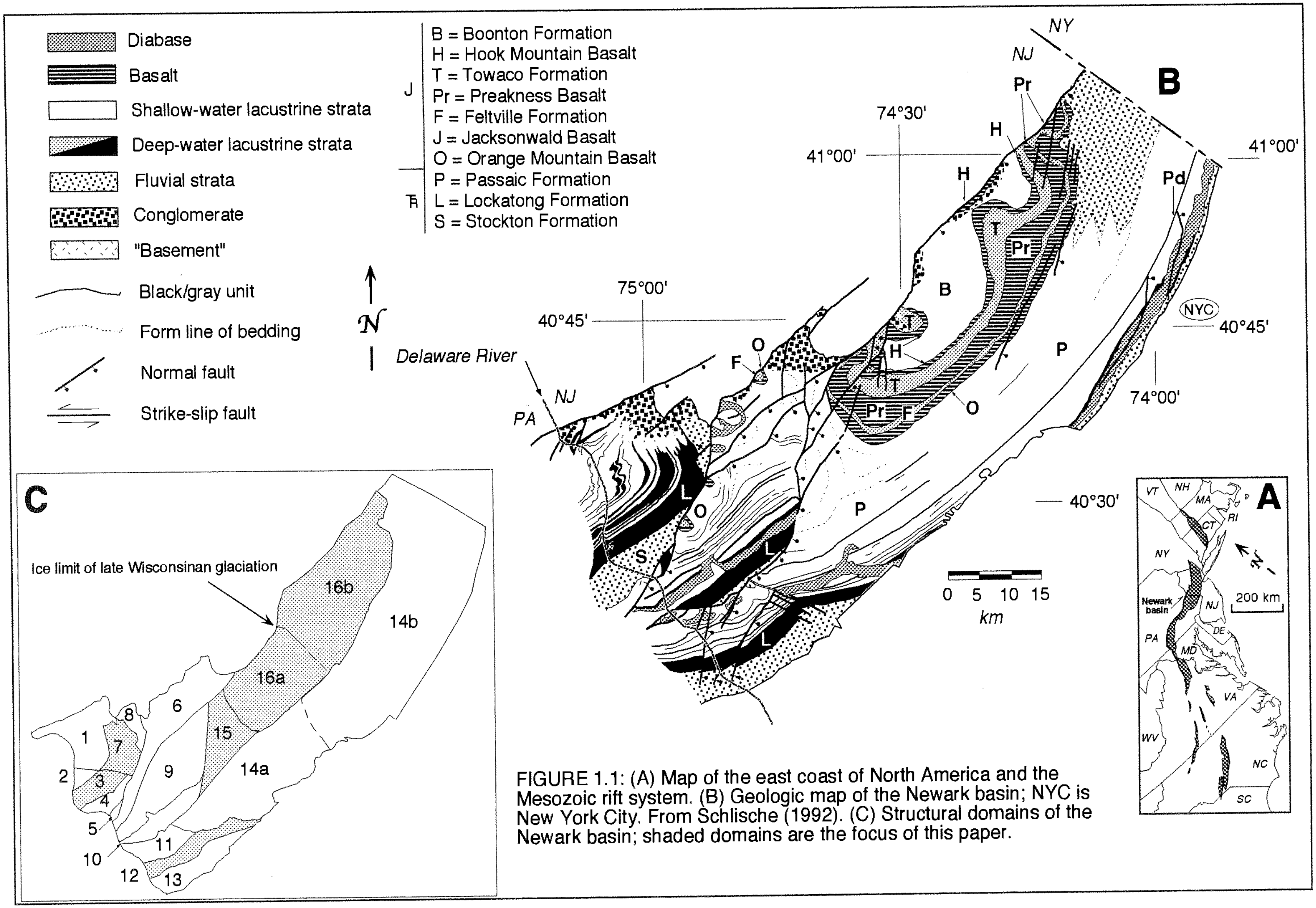

FIGURE 1.1: (A) Map of the east coast of North America and the Mesozoic rift system. (B) Geologic map of the Newark basin; NYC is New York City. From Schlische (1992). (C) Structural domains of the Newark basin; shaded domains are the focus of this paper.

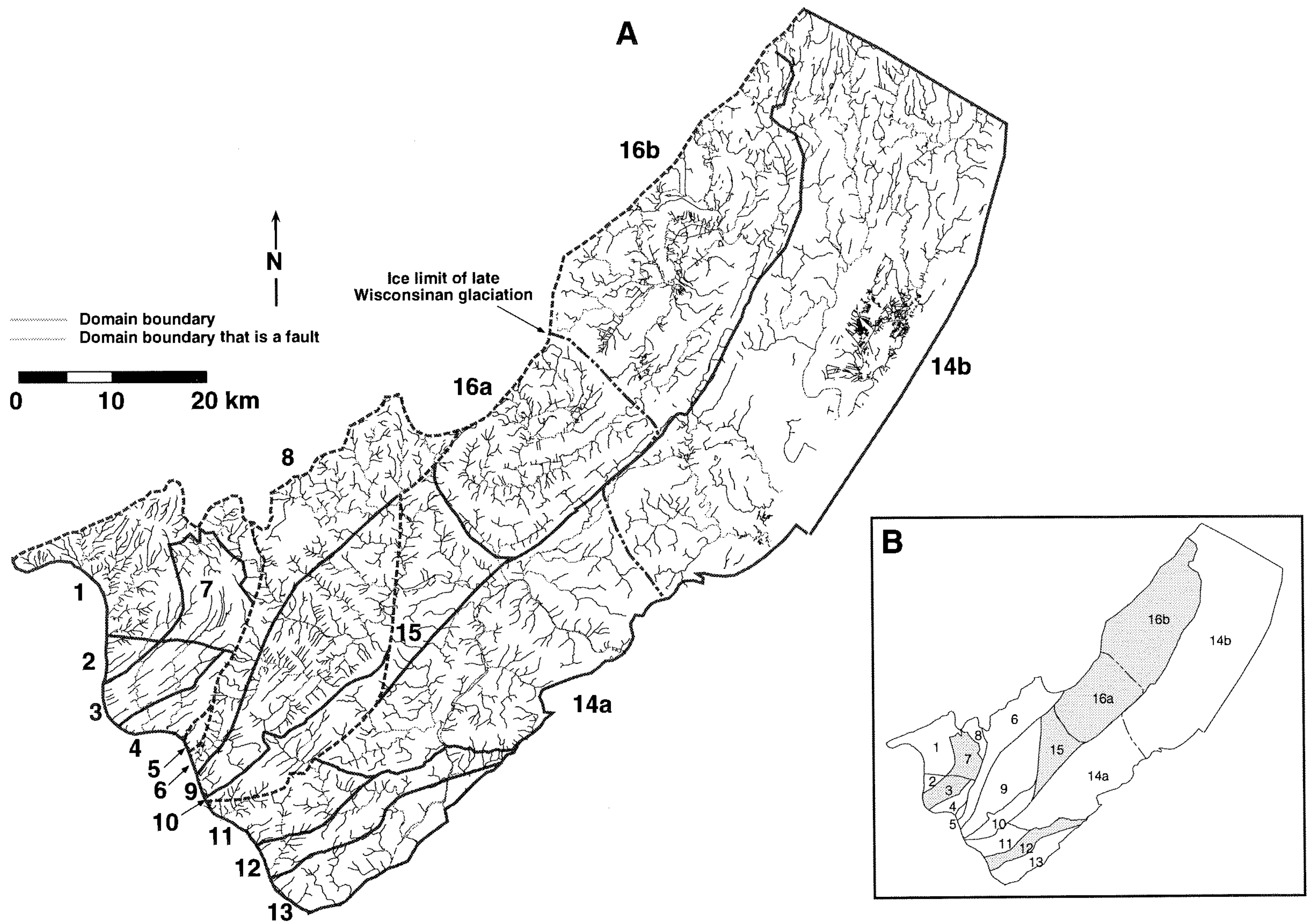

Figure 1.2: A. Streams of the Newark basin in New Jersey, with structural domains outlined. B. Domains discussed in detail in this paper.

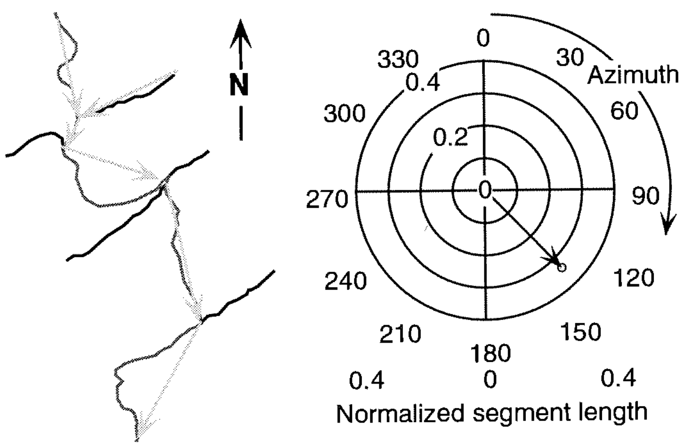

Figure 1.3: Method for determining channel segment flow vectors. Channels are broken down to confluence-confluence segments. Length components are normalized to the sum of the lengths for a given order by domain, and the normalized flow vectors are plotted on a polar diagram. The example point shown represents a channel segment with a normalized length of ~0.35 and a flow azimuth of ~135˚.

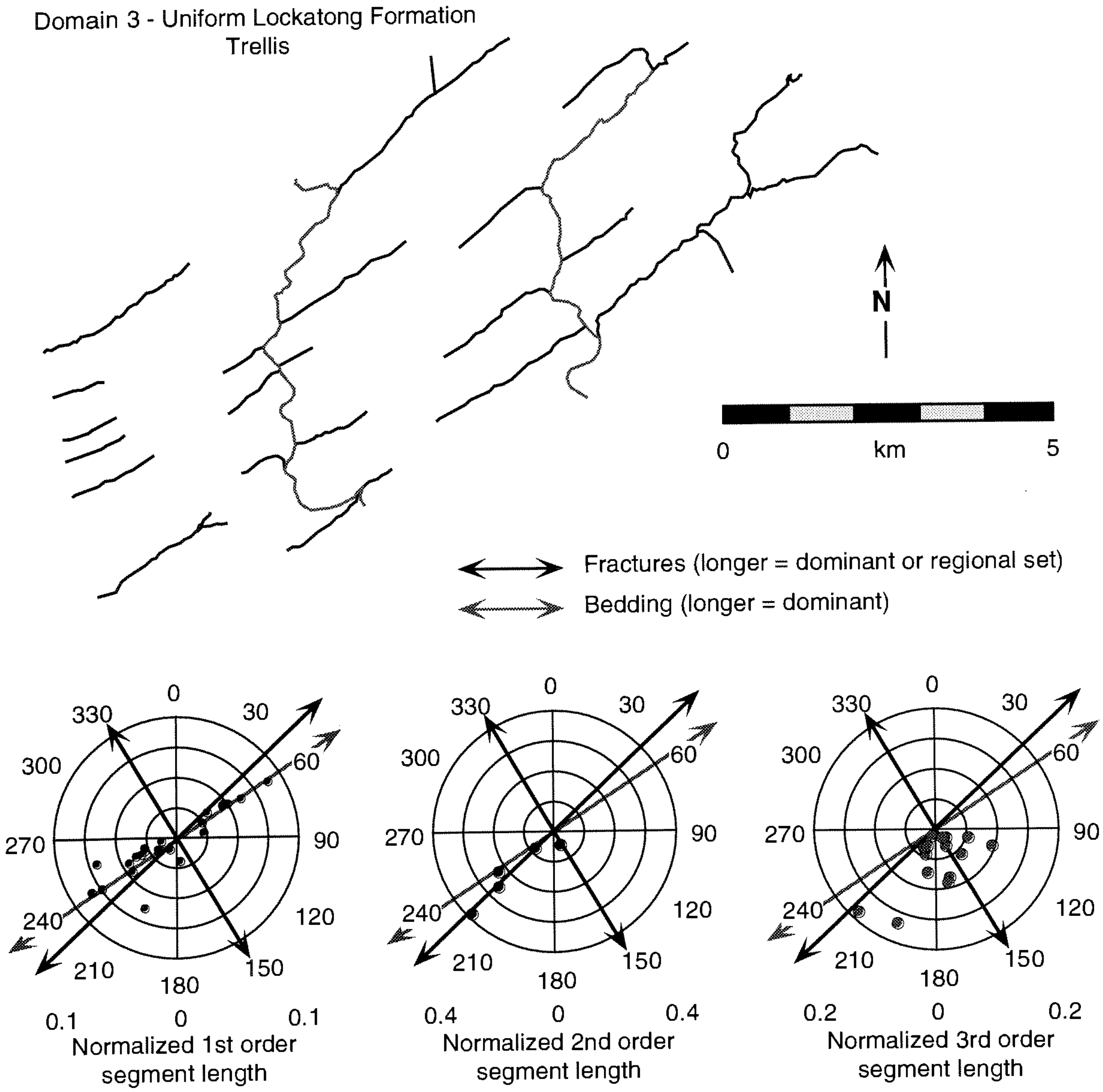

Figure 1.4: Streams, flow vector and structural data for Domain 3. See text for discussion.

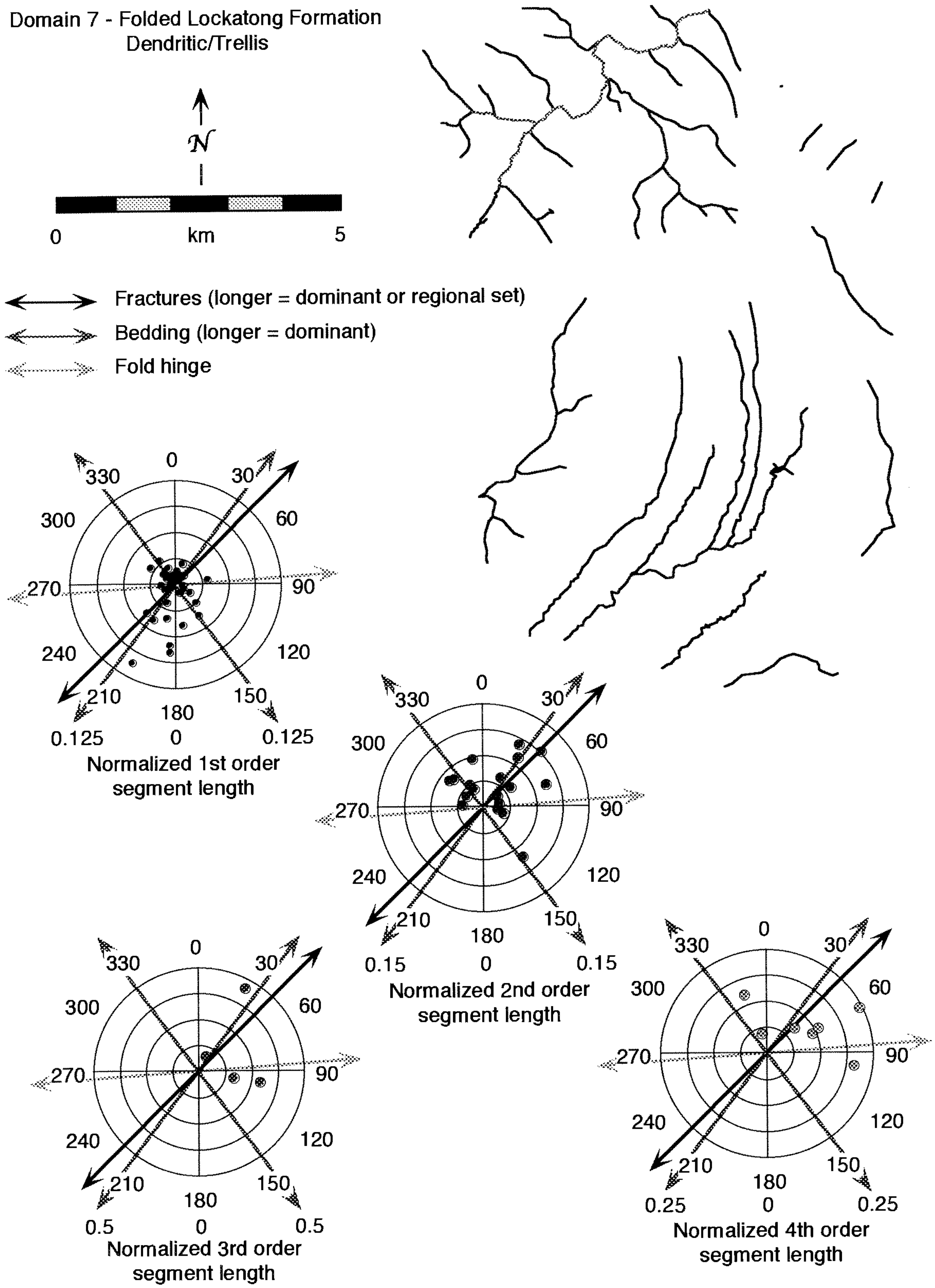

Figure 1.5: Streams, flow vector and structural data for Domain 7. See text for discussion.

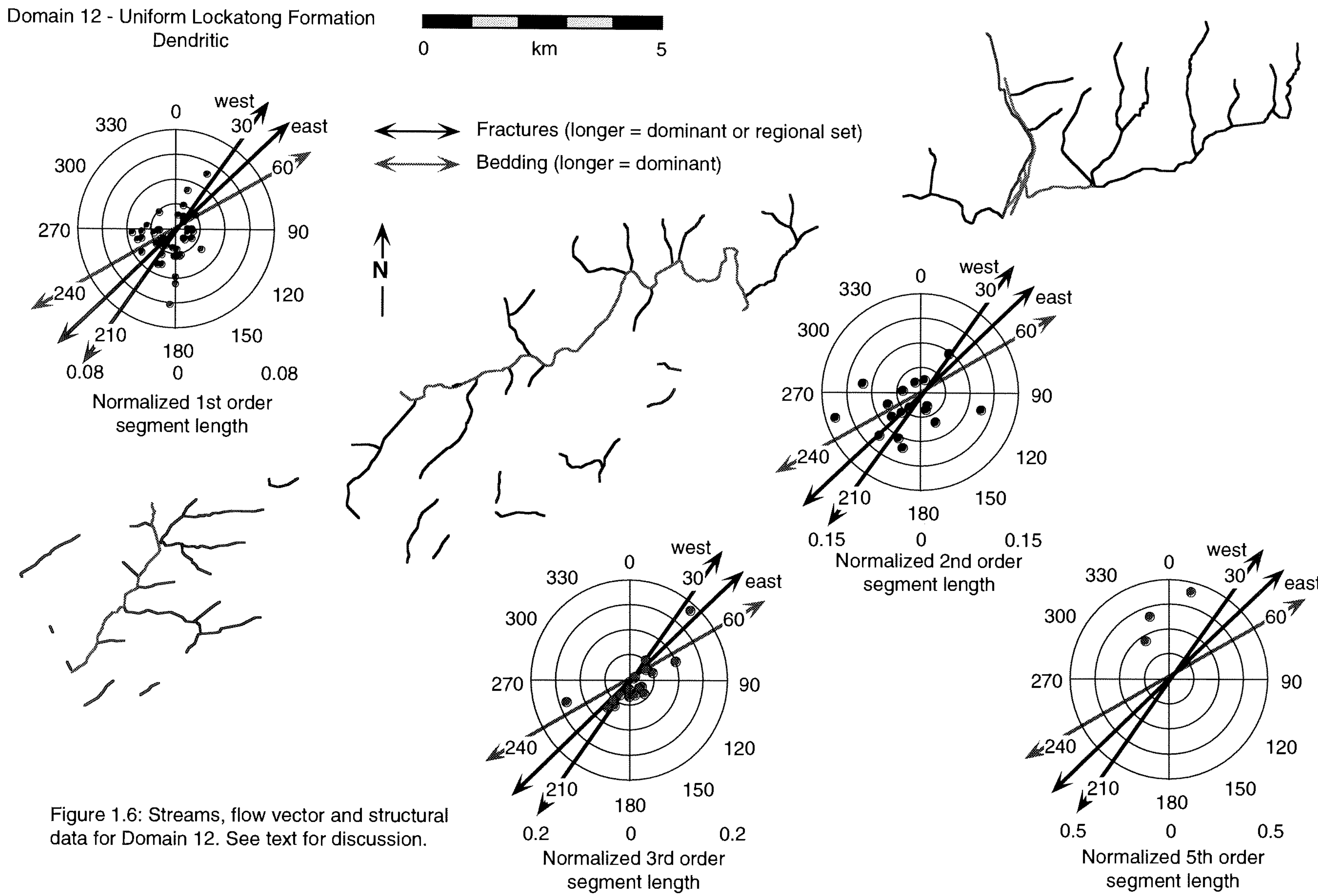

Figure 1.6: Streams, flow vector and structural data for Domain 12. See text for discussion.

Figure 1.7a: Streams and structural data for Domain 15. See text for discussion.

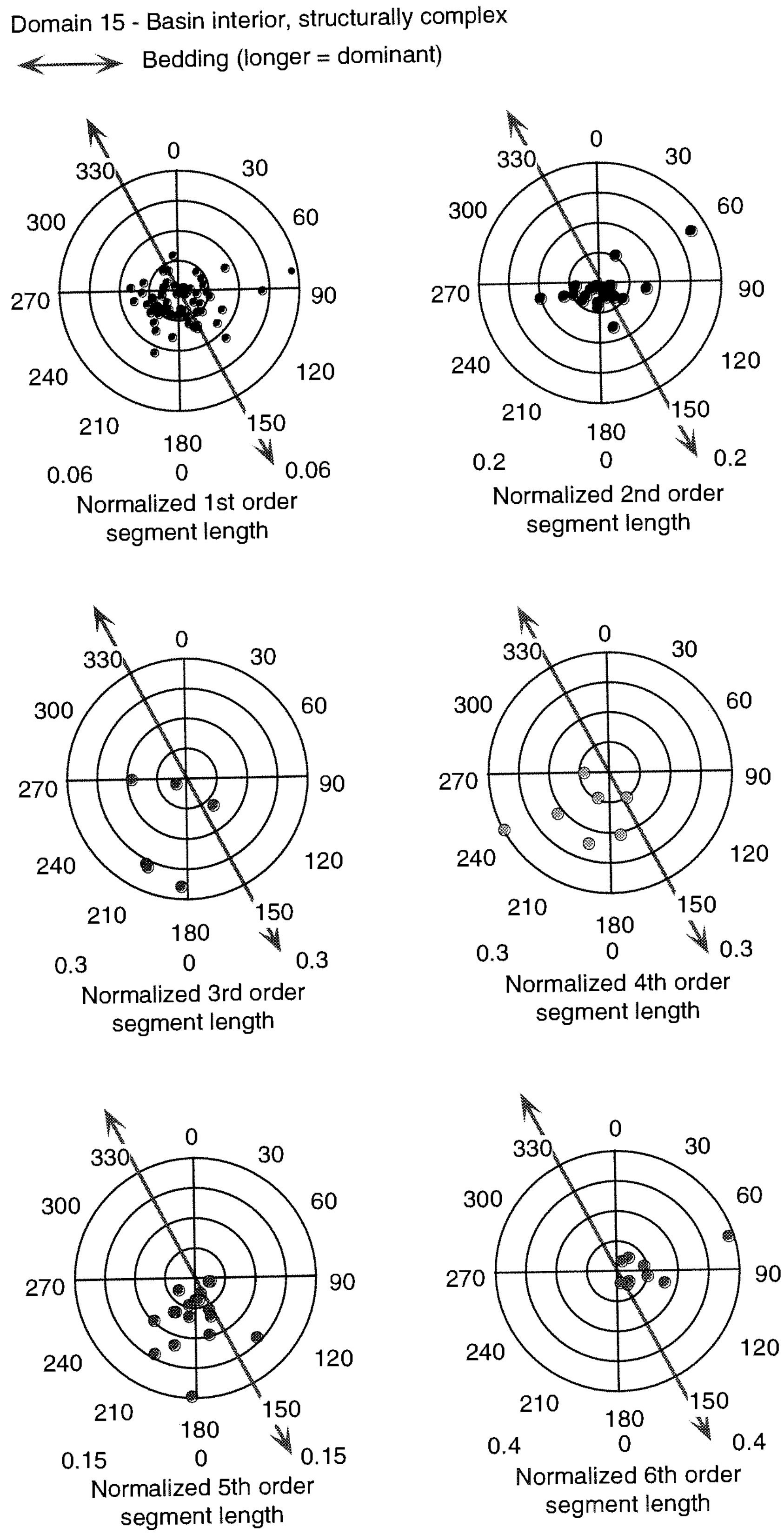

Figure 1.7b: Flow vector and structural data for Domain 15. See text for discussion.

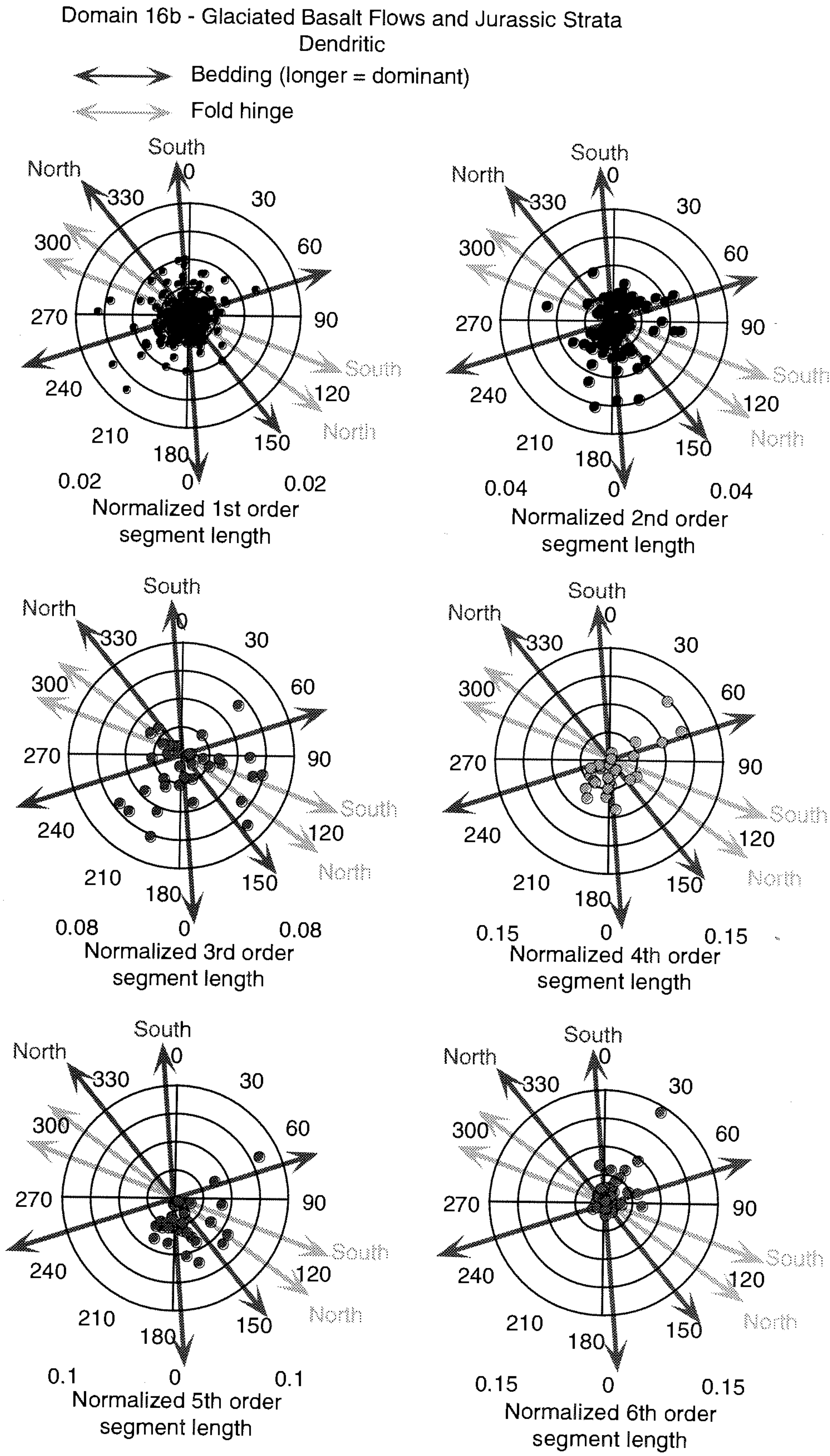

Figure 1.9b: Streams, flow vector and structural data for Domain 16b. See text for discussion.

16a - Unglaciated Basalt Flows and Jurassic Strata

Dendritic / Annular / Trellis

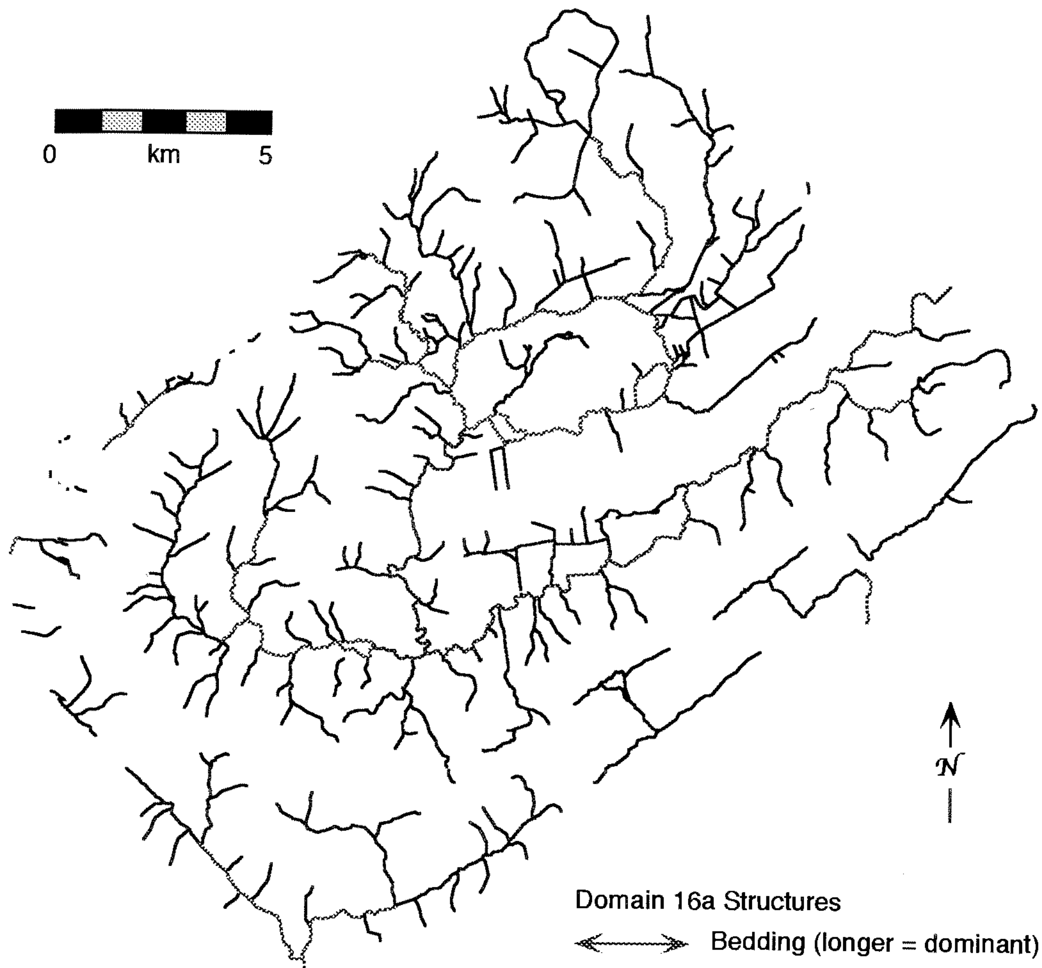

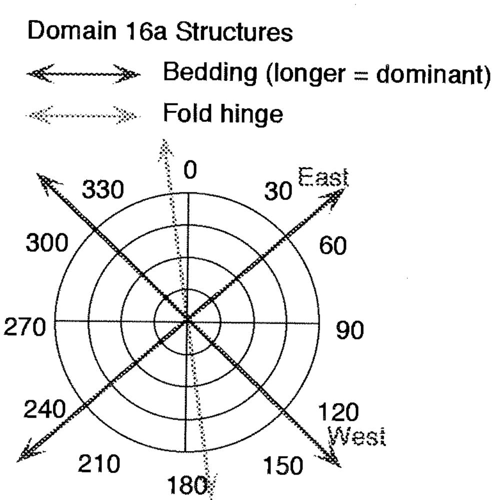

Figure 1.8a: Streams and structural data for Domain 16a. See text for discussion.

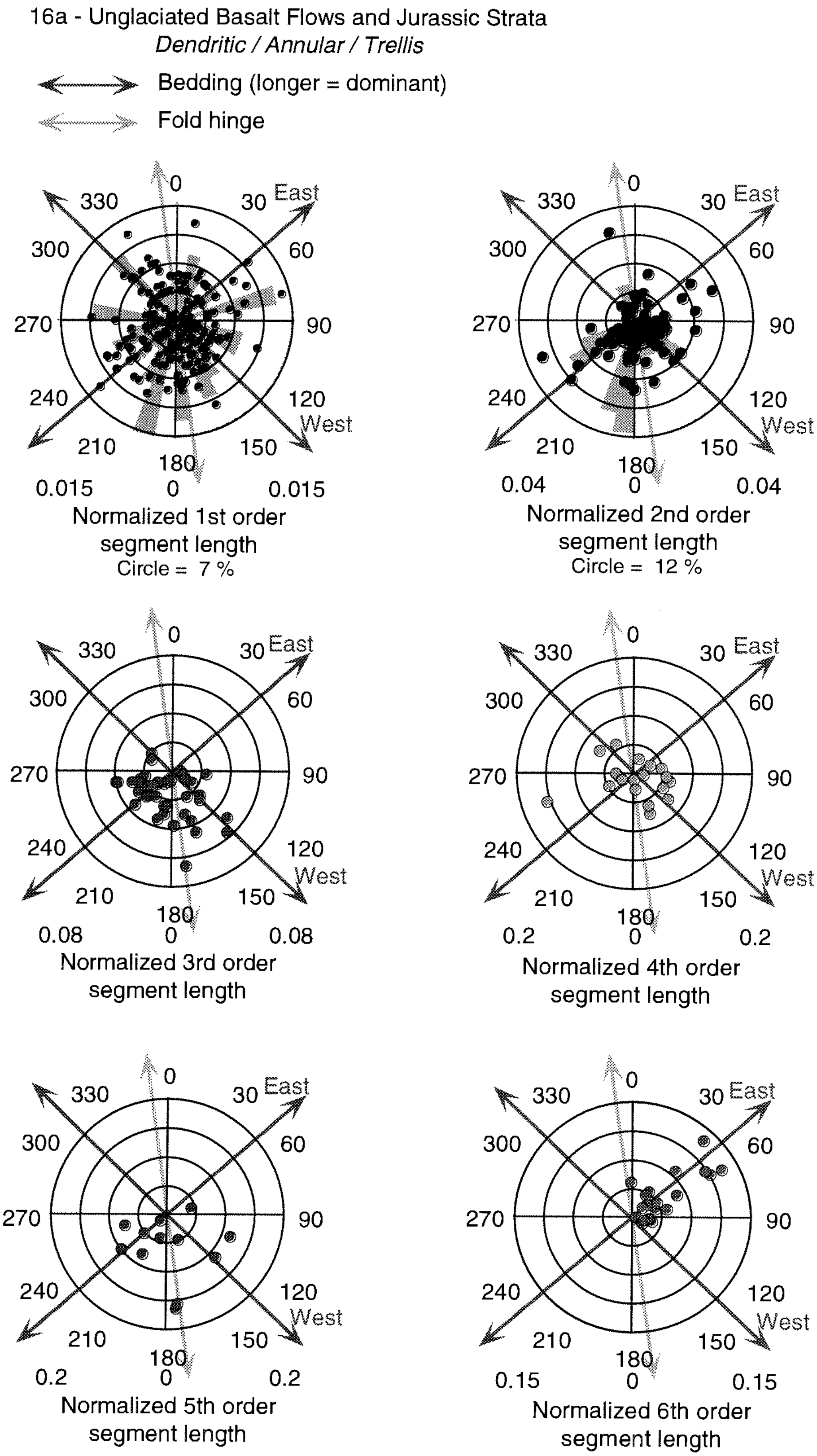

Figure 1.8b: Flow vector and structural data for Domain 16a. See text for discussion.

Domain 16b - Glaciated Basalt Flows and Jurassic Strata
Dendritic

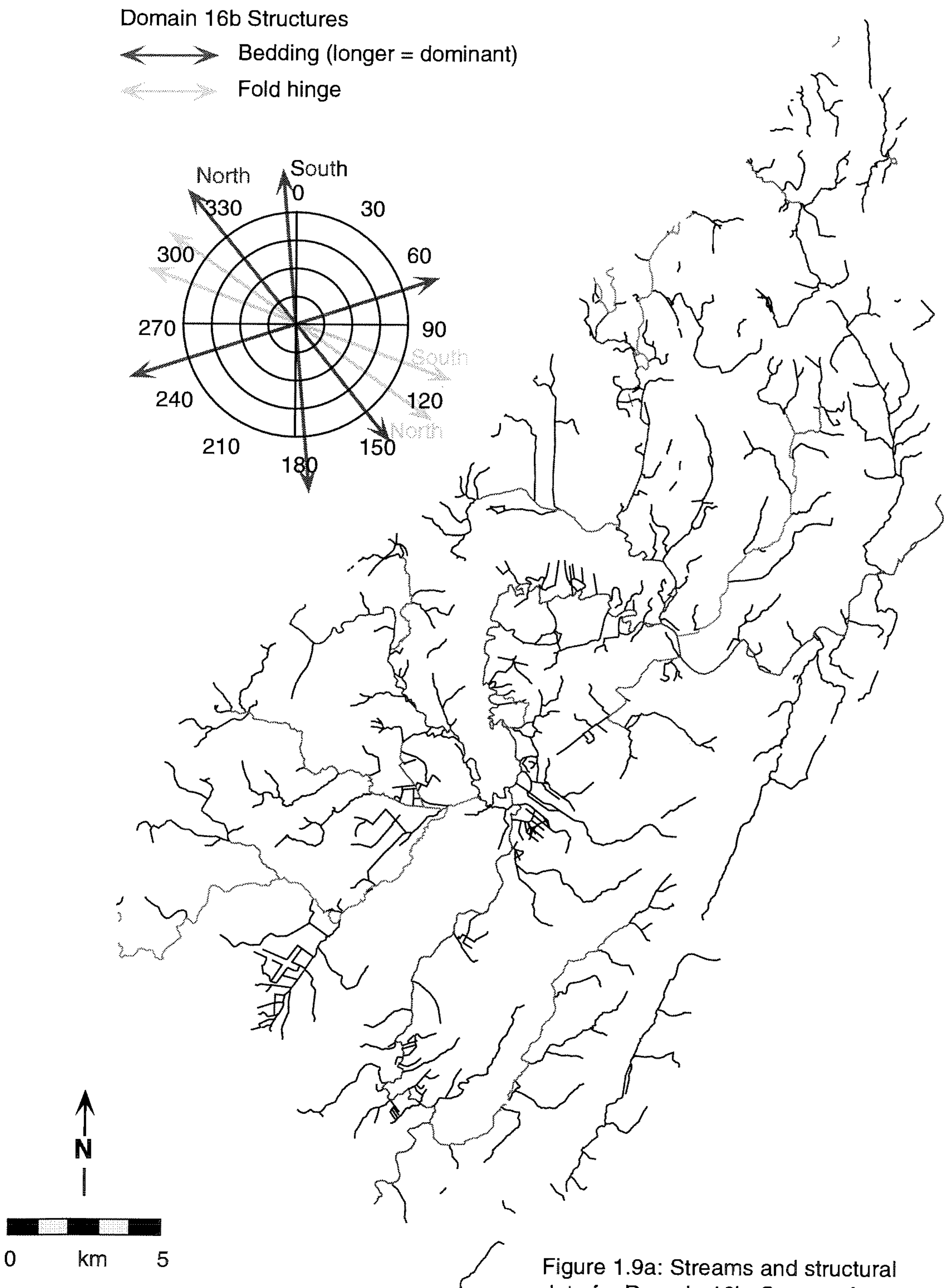

Figure 1.9a: Streams and structural data for Domain 16b. See text for discussion.

CHAPTER TWO: A LAGERSTÄTTE OF RIFT-RELATED TECTONIC STRUCTURES FROM THE SOLITE QUARRY, DAN RIVER/DANVILLE RIFT BASIN

SYNOPSIS

The Solite Quarry within the Dan River/Danville basin contains an extensive suite of neo-formed and reactivated rift-related structures. The cyclical Leekesville Formation has been deformed both ductilely and via all three brittle failure modes, exhibiting fracture partitioning such that failure mode is lithologically dependent. All structures are tectonic, extension estimates are roughly comparable for all failure modes, and there is a distinct absence of bedding-parallel detachment horizons with normal separation. All extensional structures formed in response to the same remote applied tectonic stress (Triassic rifting). These observations imply that different beds failed coevally or semi-coevally in extension. All contractional structures are consistent with earliest Jurassic inversion.

The normal faults present within the quarry are the smallest normal faults studied in detail to date. These very small faults (~ 0.1 cm $< L < \sim 200$ cm) dip at 70° to bedding, are synthetic to the border fault system of the basin, and are in most ways like larger faults. They occur both as isolated features and as segments of relay systems. The faults exhibit slickensided, mineralized fault surfaces; footwall uplift; hanging-wall subsidence; relay ramps; and elliptical fault surfaces. Maximum displacement occurs at fault centers and tapers to zero at the tips. These small faults extend the global length-displacement data set from 7 to 9 orders of magnitude of fault length, and demonstrate that maximum displacement scales linearly with length over that scale range, suggesting that fault growth is scale invariant.

INTRODUCTION

A field locality in the Dan River/Danville basin known as a major *Lagerstätte* for Triassic terrestrial arthropods and flora (e.g. Frasier et al., 1996) contains an exceptionally well-exposed suite of rift-related discontinuous (brittle) and continuous (ductile) deformation features. Detailed study of this exquisite suite of structures permits verification/nullification of a range of theoretical empirical relationships related to the processes and results of fault growth, specifically fault-scaling laws. In addition, careful studies of small-scale systems with simple strain histories provide information critical to a comprehensive understanding of large-scale systems, such as rift basins, studies of which are commonly hampered by poor exposure and complex basin architecture. Models of fractured bedrock systems such as the eastern North American rift system require detailed information on the size and spatial distribution of fractures in order to be effective for purposes such as groundwater prospecting and mining, petroleum exploration and exploitation, and the remediation of contaminated aquifer systems.

Fractures are ubiquitous within the Earth's crust, forming in response to a wide range of far and near-field stresses, from continental rifting to contracting lava as it cools. Fractures can be observed over a wide scale range, from micro-fractures in sandstones recovered in cores to continental lineaments. In effect, the border fault system of a rift basin is a very large shear fracture (see Schlische 1997). At this time, it is loosely accepted that continental normal fault systems are scale invariant with respect to their geometry and size distribution (e.g. Scholz and Cowie, 1990; Marrett and Allmendinger, 1992; Pickering et al., 1995; Schlische et al., 1996). Although this is an extremely active area of discussion in the literature and the focus of a great deal of research, it remains to be seen if all aspects of fractures are indeed scale invariant. A considerable amount of attention has been centered in recent years on understanding the processes of fault growth and coalescence, as well as how fault systems change through time (e.g. Cowie *et al.*, 1996). The population of structures at the Solite Quarry provides a unique opportunity to examine all of these issues in detail.

In this chapter, we systematically discuss the rift-related structures present within the Solite Quarry. The features are first described by category (brittle/discontinuous vs. ductile, tension vs. shear) and then by type of strain accommodated (extensional vs. contractional). We then examine how the different features are spatially distributed (stratigraphically and laterally) within the quarry, and the implications of these observations for fault-scaling relationships, lithologically dependent failure modes (mechanical stratigraphy), and Mohr-Coulomb behavior.

GEOLOGIC SETTING

The outcrops discussed in this chapter are located in the Main and New quarries of the Virginia Solite Corporation located in the Dan River/Danville basin, directly on the border between Virginia and North Carolina (Figure 2.1). The Dan River/Danville basin is part of the Mesozoic rift system on the eastern coast of North America, which formed in response to the Triassic initiation of break-up of the supercontinent of Pangea. At the time of rifting, σ_1 and σ_3 are inferred to have been vertical and NW-SE directed, respectively (Schlische, 1997). The basin itself is a highly elongate half-graben with a southeast-dipping border fault system (the Chatham fault zone) (Figure 2.1). The basin's high length to width ratio (11:1) (Kent and Olsen, 1997) is likely a result of inversion of the basin during earliest Jurassic time, due to re-orientation of the principal stresses at the onset of seafloor spreading in the Atlantic ocean (Withjack *et al.*, 1997).

The 4000 m of basin fill (Dan River Group) rest in depositional unconformity over basement, and dip toward the border fault system at angles from 20° to 50° (Kent and Olsen, 1997). The Solite Quarry lies within the upper Cow Branch Member of the Leekesville Formation, as defined by Kent and Olsen (1997). This member, as described by the previous authors, is a ~1950 m thick sequence of cyclic grey to black mudstones of deep-water lacustrine facies. Within the quarry, bedding-dip angles range from 30° to 40°. In subsequent sections, all structural orientations have been corrected for bedding dips.

STRUCTURES PRESENT WITHIN THE QUARRY

Brittle/Discontinuous Deformation - Extension

Mode I Fractures Mode I fractures are common within the Solite Quarry and exhibit the classic "penny-shaped crack" form described by Pollard and Aydin (1988) in both cross section and plan view (Figure 2.2a). Layers containing mode I fractures are typically medium- to fine-grained feldspathic sandstones. The vast majority of mode I fractures are calcite veins with cockscomb texture (e.g., Davis, 1984). They are restricted to discrete lithologies, are oriented subnormal to bedding, terminate at sharp lithologic boundaries, and have an average fracture spacing (at this scale range) that is roughly proportional to mechanical layer thickness (Figure 2.2a) (e.g. Gross *et al.*, 1995). The fractures can be divided into two sets based on orientation. The dominant set is subvertical, striking ~045° (Figure 2.3), suggesting that σ_1 and σ_3 were vertical and NW-SE directed, respectively, at the time of fracture formation. This is consistent with stress directions inferred from basin geometry and intrabasinal faults. The subordinate set is also subvertical, striking ~005°, subparallel to a regional (subordinate) dike set (~358°) (see Schlische, 1997, figure 4) that postdates the initiation of inversion of the basin in earliest Jurassic time (~200 Ma). The dominant regional dike set (~320°) (see Schlische, 1997, figure 4) is believed to be coeval with the initiation of inversion (Withjack *et al.*, 1997).

Extensional strain accommodated by mode I fractures was calculated using the sum of bed segments between veins along a scan-line and the length of the scan line. The average strain estimate is 5.4%. A histogram of vein spacings (Figure 2.4) for a bed in the main Solite quarry shows a skewed, log-normal distribution of spacings that is commonly observed where tension fractures are restricted to lithologically controlled mechanical layers (e.g. Ladeira and Price, 1981; Narr and Suppe, 1991; Gross, 1993a, b). There is significant under-sampling of the smallest size intervals, which is typical for outcrop studies where microscopic structures have not been included in the sample. As of yet, no quantitative thin-section work has been done on the Solite rocks. Hence, our average strain estimate for mode I fractures should be regarded as a minimum at this time.

Hybrid Fractures Hybrid fractures are shear fractures with a substantial tensile component (e.g. Dunne and Hancock, 1994). Within the Solite Quarry, hybrid fractures formed within medium- to coarse-grained feldspathic sandstones (Figure 2.2b), and are restricted to discrete lithologic intervals in the same manner as mode I fractures. Hybrid fractures are so rare within the quarry that there are not enough of them to generate reliable extension estimates, although they appear to be accommodating approximately the same amount of strain as mode I fractures. Hybrid fractures are the least common fracture type in the Solite Quarry.

Shear Fractures (Small Normal Faults) The third brittle failure mode (shear or mode II/III fractures) is represented by very small, neo-formed normal faults (Figure 2.2c). They are restricted to fine-grained massive siltstones that occasionally separate cleanly along bedding plane partings. These structures formed prior to basin-scale reverse drag associated with hanging wall subsidence, as well as normal drag associated with reverse faulting and inversion, and are thus best called early tectonic shear fractures. These are the smallest normal faults studied in detail to date, and are of particular interest because they are exceptionally well exposed and better constrain the scale range over which faulting takes place. They exhibit normal stratigraphic separation in both plan (Figure 2.2c) and cross-section views (Figures 2.2e-f), as well as footwall uplift and hanging-wall subsidence (Figures 2.2f, 2.5e). Isostasy is not a consideration at this scale range, hence the footwall uplift must be due to coseismic elastic deformation of the volume surrounding the fault. The bedding surfaces shown in Figure 2.2c can be traced continuously around the tips of the faults, and thus can be used as an offset marker. These very small faults (~0.5 cm <L< ~300 cm, where L is fault length) are planar and blind, dip at 70° to bedding (Figure 2.2d), and are synthetic to the border fault system of the basin (the conjugate set is not present). They are in many ways like their larger cousins, although they are unaffected by factors such as isostasy, erosion, and sedimentation. Some (~50%) of the structures exhibit a slight tensile component. The orientations of the small faults are consistent with Triassic rifting (Figure 2.3). Bedding thickness remains constant across the faults, indicating that they are not syndepositional. Their elliptical fault surfaces (Gupta and Scholz, 1996) contain either tool and groove (Figure 2.2d) or fibrous (calcite) slickensides (Figure 2.2c), ensuring their brittle origin. Slickenlines rake at high angles, indicating predominantly dip-slip motion. The faults occur both as isolated features and as segments of relay systems, with relay ramps between overlapping fault segments in map view (Figures 2.2c, 2.2d); relay structures are common to faults at a variety of scales (e.g. Larsen, 1988, Peacock and Sanderson, 1991, Dawers *et al.*, 1993). The faults also overlap in vertical section.

Extensional strain in beds containing small faults was calculated using the sum of heaves collected along scanlines oriented normal to the fault traces. The average extensional strain is ~4%. Along the length of the faults, displacement is at a maximum at the center of the fault and tapers to zero at the tips (Figures 2.2c, 2.5a), consistent with displacement profiles observed on larger structures (Figure 2.5b) (Dawers *et al.*, 1993). This is the geometry predicted by models of fault growth that incorporate a process zone, where inelastic and non-brittle processes such as plastic deformation, frictional wear, and mechanical breakdown occur at the fault tip (Cowie and Scholz, 1992b). Displacement also varies along the height of the faults, such that larger displacements occur towards the center of the structures, tapering to zero toward the upper and lower tips (Figures 2.2e-f), where the faults terminate into zero-displacement cracks. Far-field deformation affecting the volume surrounding the fault (required to maintain geometric coherence (e.g. Barnett *et al.*

(1987)) is expressed as bedding deflection (reverse drag) that decreases away from the faults (Figure 2.5c), generally consistent with elastic models of fault growth (Gupta and Scholz, 1996), and observations of faults at a variety of scales (e.g. Barnett *et al.*, 1987; Barientos *et al.*, 1986; King *et al.*, 1988; Schlische, 1995; 1997).

Unravelling the scaling relations of fault populations has been the focus of considerable attention and discussion over the last several years (e.g. Cowie and Scholz, 1992a,b; Gillespie *et al.*, 1992; Schlische *et al.*, 1996). One topic of discussion has been the relationship between the fault length and displacement, and whether the relationship is linear (scale-invariant) over many orders of magnitude. The general scaling relation is given as

$$D = cL^n$$

where D is displacement, L is length, c is related to rock properties (thus varying from population to population), and n is some exponent. The value of the exponent n has been vigorously discussed in the literature (e.g. Gillespie *et al.,* 1992; Cowie and Scholz, 1992a,b; Schlische *et al.*, 1996), with determinations ranging from $n \approx 2$ (Watterson, 1986; Walsh and Watterson, 1988), to $n \approx 1.5$ (consistent with linear elastic fracture mechanics) (Marrett and Allmendinger, 1992; Gillespie *et al.*, 1992), finally converging on $n \approx 1$ (Cowie and Scholz, 1992a; Dawers *et al.,* 1993; Schlische *et al.*, 1996). Schlische *et al.* (1996) added length-displacement scaling data from the small faults present in the Solite Quarry (Figure 2.6). As an individual data set, length scales linearly with displacement ($n \approx 1$) for the Solite faults (Figure 2.6). These data span over two orders of magnitude, and are the largest data set to date. They extend the global length-displacement data set from 7 to 9 orders of magnitude of fault length (Figure 2.6), and demonstrate that maximum displacement scales linearly with length over 9 orders of magnitude, suggesting that fault growth is scale invariant ($n = 1$, Schlische *et al.,* 1996). The determination of $n = 1$ supports Cowie and Scholz's (1992b) elastic-plastic model of fault growth. Other than differences in c related to rock properties (bigger faults sample deeper and stronger rocks, Cowie and Scholz, 1992b), there are no fundamental differences between small and large faults.

Ductile Deformation - Extension

The fourth style of extensional deformation present within the section is ductile/continuous (non-brittle). Black shales are interbedded with the three aforementioned lithologies, but do not exhibit brittle failure (Figure 2.2a). There are no bedding-parallel extensional detachments within the section: all beds are welded together. Thus, in order to maintain strain compatibility, the black shale layers deformed ductilely. Deformation of this type is manifested as deformed mudcracks and stretching lineations aligned with the extension direction inferred from mode I fractures and small faults.

Brittle/Ductile Deformation - Compression/Inversion

Multiple contractional structures present in the Solite Quarry are related to inversion of the basin during earliest Jurassic time (Figure 2.3). The orientations of these features are consistent with the high aspect ratio of the basin in both map and cross section views, as well as steep bedding dips within the quarry. Some of the contractional structures in the quarry are thought to be neo-formed, whereas others are believed to be reactivated extensional features. One such structure is a reverse fault ($L \approx 15$ m) that appears to be a reactivated normal fault (Figure 2.7a); the structure is parallel to all other small, intermediate, and large normal faults within the quarry. Small faults (~2 cm $<L<$ ~10 cm) located in the hanging wall of the inverted fault may have been reactivated as normal faults, such that they are "torqued" (Figure 2.7b): as the larger fault moved, synthetic small faults located in its hanging wall anticline appear to have slipped, although they did not lengthen according to the same scaling relation they followed during their initial formation. Nonetheless, the relationship between L and D was probably still linear. We attribute this to changes in the rock properties and thus c between the time of formation the extensional features (see next section) and the time of initiation of inversion, which corresponds to the burial and thermal maximums for these rocks (Withjack *et al.*, 1997).

Several individual shale layers were shortened during inversion of the Dan River/Danville basin. Black shales occasionally serve as contractional decollemént surfaces with multiple imbricate thrust sheets (Figure 2.7c). Microlaminated organic-rich shale layers known for their terrestrial fossils have also been shortened, forming very small folds in advance of propagating reverse faults (Figure 2.7d). The fossils themselves have been deformed (Olsen *et al.*, 1989, Frasier *et al.*, 1996).

Neotectonic Structures

Quarry buckles present within the Solite Quarry (Figure 2.7e) suggest a NE - SW directed maximum principal horizontal stress (Figure 2.3). The buckles formed due to unloading as material was removed during the quarrying process. The resultant folds (buckles) formed such that their fold axes are orthogonal to the maximum horizontal principal stress direction (Stewart and Hancock, 1994). Neo-formed fractures associated with the buckles parallel the axes of the buckles.

VERTICAL DISTRIBUTION OF STRUCTURES

Within the Solite Quarry, deformation style and failure mode correlate closely with lithology, such that mode I fractures, hybrid fractures and small normal faults are all restricted to discrete lithologic layers; there is no vertical connection between most of the fractures. In order to quantify this relation, samples of each lithology were analyzed to constrain their composition using a combination of methods (geochemical and x-ray diffraction). Three samples of rock exhibiting each extensional deformation style (tension, hybrid, shear, ductile) were run. Fresh samples of host rock were fluxed using lithium metaborate following Feigenson and Carr (1985), and were analyzed for weight-percentages of major oxides using a direct current plasma atomic emission spectrometer. X-ray diffraction was used in order to determine the relative abundances of minerals in the samples. The analyses were conducted on fresh samples, and performed on a Siemens D500 diffractometer using Ni-filtered CuK_{α} radiation, a divergent slit of 1° and a receiving slit of 0.05°, an operating voltage of 40KV, and a current of 30 mA. The data were collected by a DACO microprocessor using a stepwidth of 0.05° 2θ and a measuring time of 3 seconds. Phases were identified by matching with standard XRD patterns of the JCPDS file. Quantitative x-ray diffraction was not possible within the financial and time constraints of the study. Thus the oxide and phase data were combined to generate the bulk mineral compositions of the samples. This was done using a modified least squares-based magma mixing model; such models combine the same types of data to determine the bulk compositions of igneous rocks.

Figure 2.8 is the x-ray diffraction pattern for 8 of the 12 samples run. The patterns are all quite similar, varying only in the intensity of certain peaks. Note that all samples have a strong peak at 28° 2θ (albite); all samples are at least 50% albite. Albite is likely the cement for these rocks, consistent with their saline lacustrine origin (P.E. Olsen, personal communication). Other minerals present in the samples are phyllosilicates (biotite), tectosilicates (Na- and K-feldspars, quartz, analcime), carbonates (dolomite, calcite), and inosilicates (riebekite).

Figure 2.9a presents the results of the oxide analysis in terms of general carbonate vs. sandstone compositions, following Brownlow (1979). The data are sorted by failure mode, and show a correlation between increasing shear failure component and decreasing carbonate component (carbonates are generally considered to be "strong" (Suppe, 1985)). There does not appear to be a correlation between failure mode and sandstone component within the samples. In Figure 2.9b, the oxide data are shown in terms of $CaO:Al_2O_3$ ratios, with decreasing CaO and increasing Al_2O_3 trends following phyllosilicate ("weak" platy minerals) composition trends. The Solite data show a correlation between increasing shear component to the deformation and increasing phyllosilicate composition trends. Notice that the outlying point in Figures 2.9a-b is sample S2395BT. Some vein material (calcite) may have been erroneously incorporated into the sample during crushing of this mode I sample, leading to an anomalously high CaO content.

Figure 2.9c summarizes the results of the least-squares regression analysis, where the major oxide and relative mineral abundance data were combined. The data are presented in terms of percentages of "weak" and "strong" minerals. "Weak" minerals are defined as phyllosilicates; all other minerals present in the samples are "strong" minerals. There is a very good correlation between increasing proportions of "weak" minerals and increasing shear failure components (Figure 2.9c). Interestingly, the hybrid samples contain hydrous inosilicates (riebekite), which may have made them more prone to shear failure.

Given the correlation between failure mode and bulk mineralogy, the roughly comparable strain estimates in all layers, and the distinct absence of extensional bedding-parallel detachments within the section, models of the earliest stages (macroscopic failure) of this system must have specific constraints placed on them. This is very similar to the observations and model discussed by Gross (1995): coeval failure of interbedded sedimentary units of the Monterey Formation was suggested by different failure modes that accommodated the same amount of strain in the absence of bedding-parallel detachments. Gross' (1995) model invokes a specific set of boundary conditions, and could potentially be used to construct a predictive mechanical stratigraphy based on rock characteristics. Such a predictive tool would be useful for studies of groundwater and hydrocarbon accumulation and migration. There are several primary differences between the Solite mechanical section and the Monterey mechanical section discussed by Gross (1995). At Solite, mode I and shear fractures appear to have accommodated slightly different amounts of strain (~5% and ~4%, respectively). The mechanical layers at the Solite Quarry are interbedded at a smaller scale (≥ 1 m in the Monterey section, vs. ≤ 1 m in this study). There are hybrid fractures present in the Solite section, and there are layers present in the Solite Quarry that have deformed ductilely. The Solite section therefore provides another opportunity to construct a Mohr-Coulomb failure model consistent with field observations. This model requires a somewhat different set of boundary conditions than Gross' (1995) in that not all failure modes have accommodated the same amount of strain.

Our failure model is a two-component (tensile and shear) Mohr-Coulomb model for macroscopic failure, based on mechanical analogs from the literature, following the general principals set forth in Gross (1995). It uses a simple one-dimensional Hooke's law,

$$\sigma_D = E_0 \varepsilon$$

where σ_D is the differential stress, E_0 is Young's Modulus, and ε is the elastic strain prior to failure (Gross, 1995). The maximum principal stress (σ_1) is defined as

$$\sigma_1 = \rho g h$$

where ρ is the density of the rocks, g is acceleration due to gravity, and h is the thickness of the overburden (burial depth). The least principal stress (σ_3) is given by the difference between the maximum principal stress and the differential stress.

Beds that failed in tension may have failed first, since they appear to have accommodated more strain. Thus beds that failed in tension must have higher values for C_0 (cohesive shear strength), T_0 (tensile strength), and σ_D (thus higher E_0), as well as a high value for ϕ (angle of internal friction). In order to maintain strain compatibility, we followed Gross' (1995) assumption that ε is the same for both beds prior to failure. We used a value of 0.2% for ε (C.H. Scholz, personal communication). Based on an iterative modelling approach, we used a burial depth of 4 km, which yields a σ_1 of ~100 MPa. This is not inconsistent with a thermal maximum at 201 Ma of 225° C, determined from thermal maturation studies of the Solite rocks and samples from the Taylorsville basin (Malinconico, 1996; personal communication). The maximum burial depth of these rocks may have been as deep as 7 km (P.E. Olsen, personal communication). When actual triaxial loading experiments on samples are not practical, mechanical analogs from the literature must be used instead. Thus our other parameters are based on average values published for rocks descriptively similar (feldspathic sandstones and massive siltstones; Lama and Vutukuri, 1978) to those at Solite.

The model is presented in Figure 2.10a-c. In the initial condition (Figure 2.10a), both Mohr circles reside in their respective stable regions of the Mohr diagram, anchored at a σ_1 of ~100 MPa. Figure 2.10b represents the condition in which the Mohr circles have been driven to the left due to an increase in pore-fluid pressure (P_f) by 16 MPa, until the one representing the beds that fail in tension intersects the failure envelope at T_0^t, producing pure tension fractures.

At this point our model invokes semi-coeval failure while maintaining strain compatibility in a manner that is not inconsistent with Gross (1995). The condition shown in Figure 2.10c is based on Hobbs' (1967) assumption that the brittle failure of one mechanical layer will cause the stress to increase in adjacent unfailed layers as a direct result of differences in elastic displacement (as discussed in Gross *et al.*, 1995). A shear traction is imposed on the unfailed bed, causing its Mohr circle of stress to grow until it intersects the shear failure envelope at $2\theta = 140^\circ$, consistent with the 70° fault-bedding angle observed at Solite. This point of intersection also indicates a slight component of dilation, consistent with field observations of some the small faults at Solite.

These models for macroscopic failure (both ours and Gross' 1995) have limitations that must be noted. A fundamental problem is that the mechanical properties used in the models are from analogs of the rocks in question. Published data listing mechanical properties, bulk mineralogy, sedimentary geochemistry, and good lithologic descriptions are lacking, thus making these models more conceptual than case-specific. This in turn points to another weakness: it is not clear if the samples we have now are mineralogically, geochemically, and mechanically similar to when they failed at depth, making load tests questionable even if they are feasible. In the Solite example, the rocks have been metamorphosed to zeolite facies, and are thermally mature. The thermal maximum for the basin occurred after the initial formation of the fractures, just prior to inversion of the basin in earliest Jurassic time (Malinconico, 1996; Withjack *et al.*, 1997). In addition, the stress orientation analysis for the Solite rocks suggests that failure occurred prior to significant tilting of the basin fill, some of which is due to hanging-wall subsidence and reverse drag associated with rifting, but most of which is due to inversion (Withjack *et al.*, 1997). Whether or not the details of the Mohr-Coulomb failure model are correct, it is nonetheless clear that the different types of fractures are controlled by lithology and formed semi-coevally.

LATERAL DISTRIBUTION OF STRUCTURES

Mode I

A bedding plane exposure of mode I fractures from the Solite Quarry is shown in Figure 2.11. There is a uniform distribution of features across the surface. The average extension accommodated across the slab (measured using apertures from a series of scanlines) is 3.06%, with a standard deviation of 0.5 percentage points; this estimate is lower than those determined using bed lengths along a cross section scanline. The reason for this is that the bed shown in Figure 2.11 has broken at a mechanical layer boundary - the view is thus of the "top" of the mechanical layer, where mode I fractures terminate. Thus the apertures measured were not maximum apertures, which would have required sampling at the level in the bed where the fractures nucleated, if there is a single level. Nonetheless, the strain appears to be evenly distributed across the surface sampled.

Figure 2.12 is a cumulative frequency plot (number of features greater than a given size plotted vs. size) in log-log space for the lengths of the mode I fractures shown in Figure 2.11. The entire distribution is best fit using an exponential function rather than a power-law function (which only applies to a very limited scale range; dark circles in Figure 2.12). The definition of a mean value or characteristic size is a diagnostic feature of exponential distributions (Cowie *et al.*, 1994). The spacing of mode I fractures is controlled by mechanical layer thickness and rock properties, such that a characteristic spacing roughly proportional to mechanical layer thickness arises (Gross *et al.*, 1995). The exponential distribution is probably a result of a lack of spatial correlation in the system due to the effect of mechanical layer thickness on lateral positioning of fractures, which in turn suppresses the short- and long-range interaction of structures that gives rise to power-law (fractal) distributions (e.g. Cowie *et al.*, 1994).

The population of mode I fractures shown in Figure 2.11 exhibits a characteristic length of ~2.60 cm based on the slope of the best-fit exponential curve in Figure 2.12. The slope (0.384) is the reciprocal of $\langle L \rangle$, the mean value of L (e.g. Cowie *et al.*, 1994). This estimate of 2.60 cm contrasts with an average length of ~4.25 cm based on field observations. The difference likely stems from the structural level where fractures were sampled: lengths were sampled at the mechanical layer boundary (a limiting level for fracture height), not the nucleation level (if there is a common one). As a result, small fractures were under-sampled either because they do not intersect the sampled level, or because they fall below the resolution of the sampling level (naked eye). The estimate of 4.25 cm is derived from a sample where small fractures were under-represented, thus overestimating the average or characteristic length. The 2.60 cm estimate of characteristic length is likely more accurate because it relies on the distribution of fracture sizes. The distribution of sizes (the slope of the line in Figure 2.12) will not vary appreciably with structural level, provided most fractures have achieved a height equal to mechanical layer thickness. Some lengths sampled at the layer boundary will be less than the maximum lengths. In other words, depending on the structural level sampled, the intercepts of the cumulative frequency plot will change, but the slope will not, and it is the slope that provides the characteristic length.

Small Normal Faults

Over large areas, the small normal faults appear to be fairly uniformly distributed within the units that fail in shear at the Solite Quarry. There are a range of sizes (0.1 cm < L

< 200 cm) of these structures, although the vast majority of them are < 10 cm long. A division based on fault size (length) can be made (Figure 2.13): there are small faults ($L \leq 20$ cm) and larger faults ($L \geq 20$ cm, usually $L \geq 100$ cm). The larger faults are fairly infrequent, and appear to be uniformly distributed within the rock volume. Around these larger faults (master faults), there appear to be zones devoid of smaller brittle structures (Figure 2.13), which are otherwise ubiquitous in the surrounding volume. We call these regions lacking smaller faults fault shields. Master faults are defined by the presence of a fault shield around them, regardless of their size. The amount of strain accommodated within a rectilinear 2-D area around a master normal fault, including smaller faults outside the fault shield, varies along the length of the larger fault, mirroring a length-displacement profile (Figure 2.14a). When the master faults present are not included in the strain calculation, strain on the smaller structures does not vary appreciably across the study area, and the amount of strain accommodated is substantially less. The master faults are clearly dominating the strain. If one considers an area without a master fault present (Figure 2.14b), the small faults do not exhibit stepping patterns, and the amount of strain accommodated is fairly uniform and substantially less than areas with master faults.

Chapter Three of this dissertation focuses on master faults, fault shields, the lateral distribution of master and small faults in the quarry, and how these shed light on the temporal evolution of this system.

SUMMARY AND CONCLUSIONS

• The Solite Quarry contains an exquisite suite of rift-related deformation structures that provides a unique opportunity to study fracture geometries, kinematics, size and spatial distributions, and population systematics in great detail.

• Neo-formed mode I fractures, hybrid fractures, and shear fractures (small normal faults) are the dominant brittle structures related to Triassic rifting. The faults and mode I fractures are clearly geometrically and kinematically distinct, and it is therefore unlikely the

faults originated as macroscopic mode I fractures. Also present are reactivated normal faults, reverse faults, imbricate thrust faults, and microfolds, all of which are late-stage features related to inversion of the Dan River/Danville basin in earliest Jurassic time.

• All these features are restricted to certain interbedded lithologies, such that beds with greater percentages of weak minerals failed with increasing shear components. There is a distinct absence of extensional detachment horizons between mechanical layers. Mode I fractures have accommodated slightly more 1-D extensional strain than the small faults, suggesting they failed slightly earlier. This is consistent with a two component Mohr-Coulomb model of semi-coeval macroscopic failure based on mechanical analogs of the rocks studied.

• The Solite faults extend the global D-L data set by 2 orders of magnitude to a total of 9 orders of magnitude of fault length and indicate that there is no significant change in the linear D-L scaling relation.

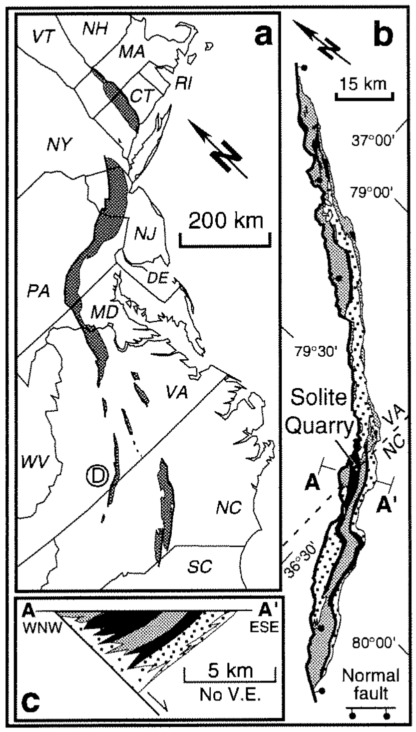

Figure 2.1: (a) Exposed Mesozoic rift basins of the eastern United States. D is the Danville basin. (b) Simplified geologic map of Danville basin, showing location of Solite Quarry. Black represents Cow Branch members of the Leekesville Formation. (c) Simplified geologic cross section of the Danville basin (see b for location), illustrating half-graben geometry modified by inversion. Modified from Olsen and Kent (1997), Schlische et al. (1996), and Schlische (1997).

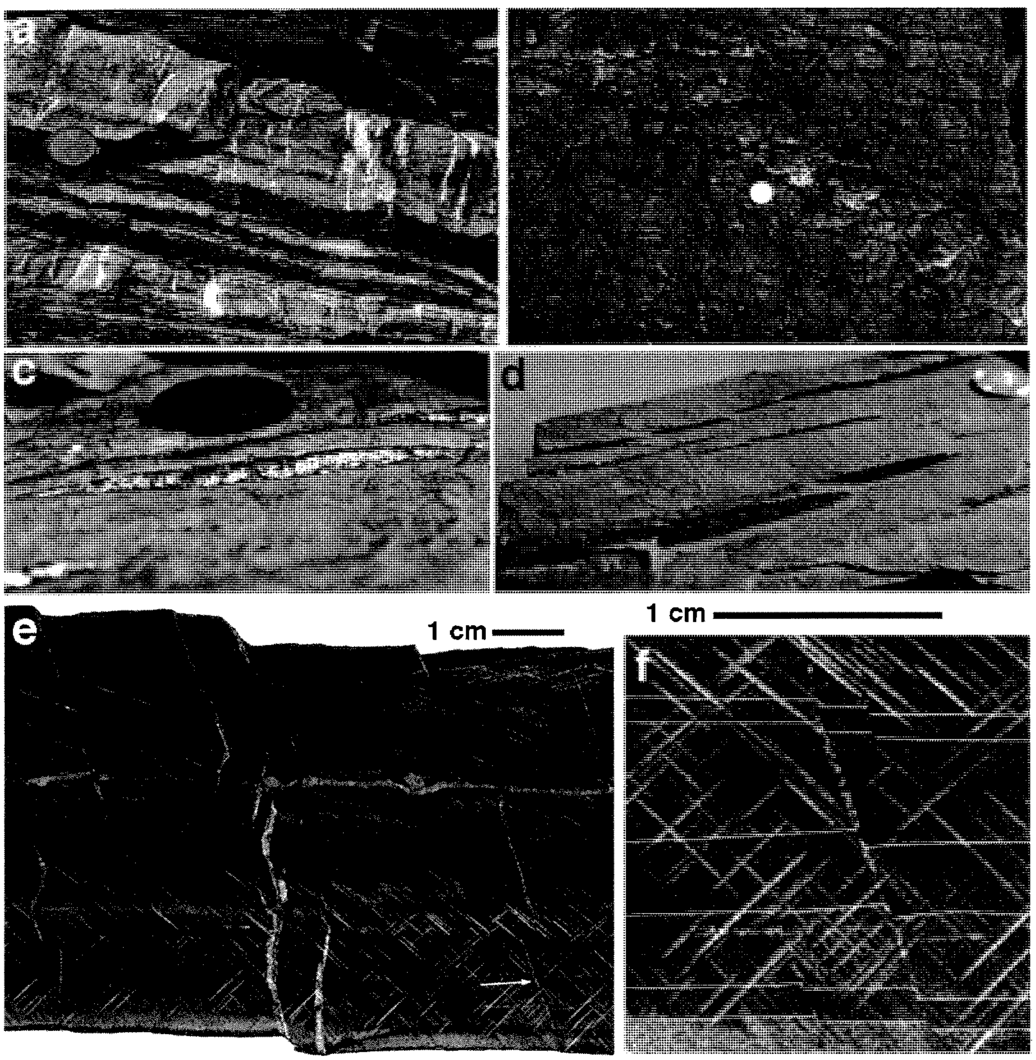

Figure 2.2

Figure 2.2: Brittle extensional features of the Solite Quarry. (a) Medium-fine grained sandstones containing calcite veins, interbedded with black shales that failed continuously; lens cap for scale. (b) Hybrid fractures that formed in medium-coarse grained feldspathic sandstones. Feature trending from top-left to bottom-right of photo is a shear zone. Coin is 2.3 cm in diameter. (c) Single small normal fault, formed in fine-grained massive siltstones; fault surface contains fibrous slickenlines that indicate predominantly dip-slip motion. Lens cap for scale. (d) Small normal faults separated by a relay structure. Fault surfaces contain tool and groove slickenlines; coin is ~1 cm in diameter. (e) Sawed section of a slab containing small faults; arrow points to a prime example of footwall uplift and hanging wall subsidence (reverse drag) along a bedding plane parting cut by a normal fault. (f) is an interpreted close-up of fault with arrow in (e). Notice that displacement along the fault is at a maximum towards the center of the fault, tapering to zero at the tips, where the structure terminates in zero-displacement cracks.

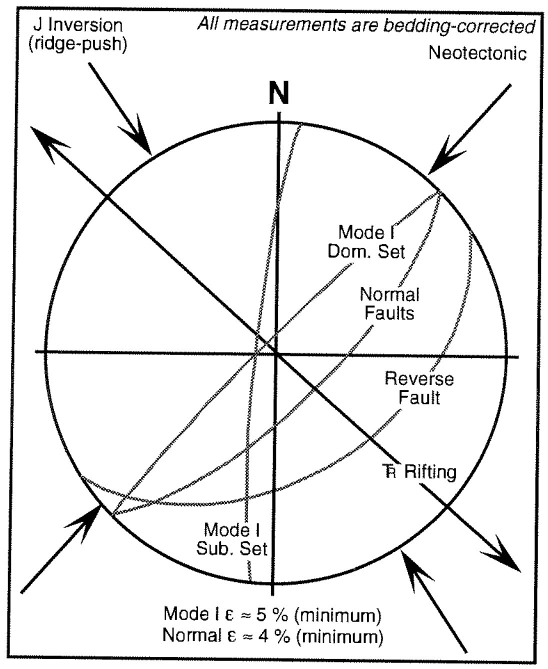

Figure 2.3: Stress orientation analysis for brittle features present at the Solite Quarry. Extensional structures are consistent with Triassic rifting; contractional structures are consistent with earliest Jurassic rifting. Great circles are means based on multiple structures: 100+ normal faults; 50+ veins; 1 reverse fault; 1 imbricate thrust stack; 5 quarry buckles.

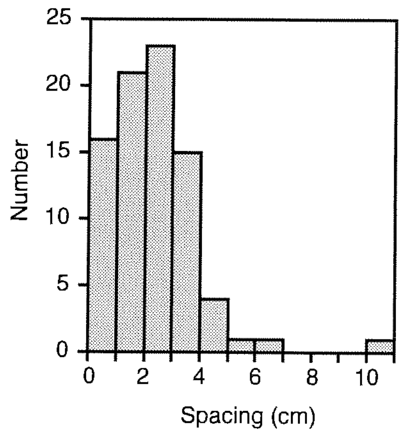

Figure 2.4: Histogram of spacings of macroscopic veins; notice undersampling at smaller spacing typical of outcrop-scale fracture studies.

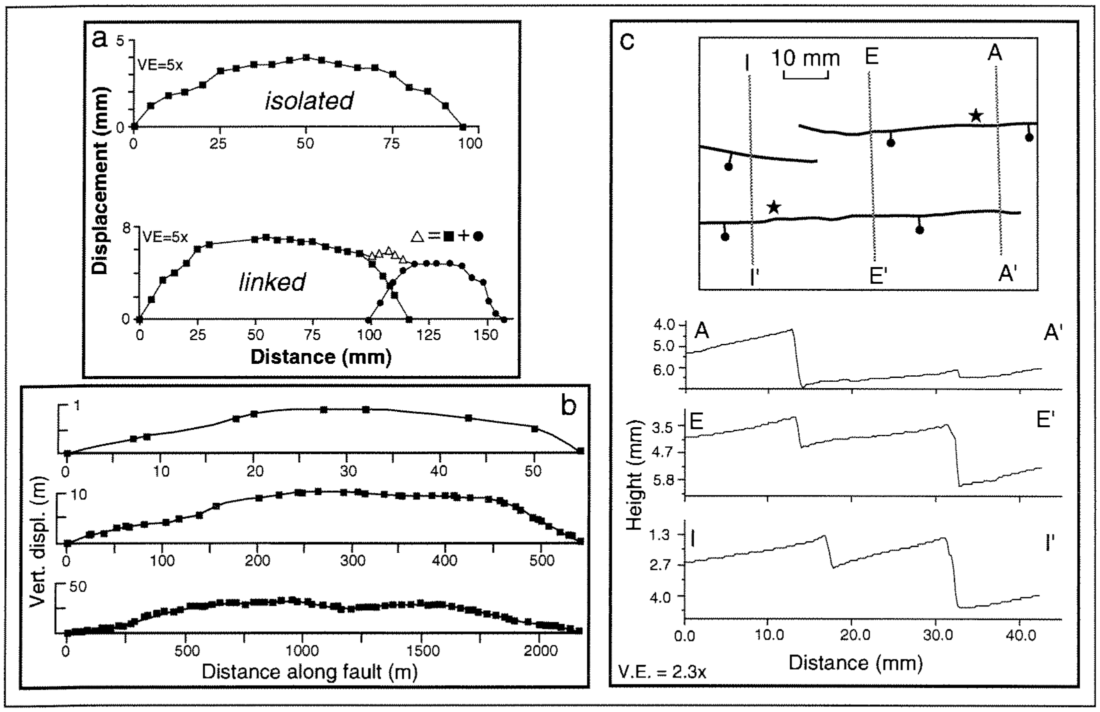

Figure 2.5: (a) Displacement versus distance plots for an isolated normal fault and a linked fault system from the Solite Qaurry. Note that displacement gradients are higher at the tips of the linked faults, and that the summed displacement profile for the linked faults resembles that of an isolated structure, indicating that they are kinematically (soft) linked, although they are not breached (hard linked) in map view. Modified from Schlische et al. (1996). (b) Variations in scarp height for large normal faults from the Volcanic Tablelands, California. Note different horizontal and vertical scales; modified from Dawers et al. (1993). (c) Top: map of a bedding surface cut by three small normal faults from the Solite Quarry. Stars indicate locations of maximum displacement, shaded lines show locations of profiles across the offset bedding surface (bottom). Notice reverse drag immediately adjacent to the faults, as well as displacement transfer between the structures, maintaining strain continuity across the map area as one fault dies out.

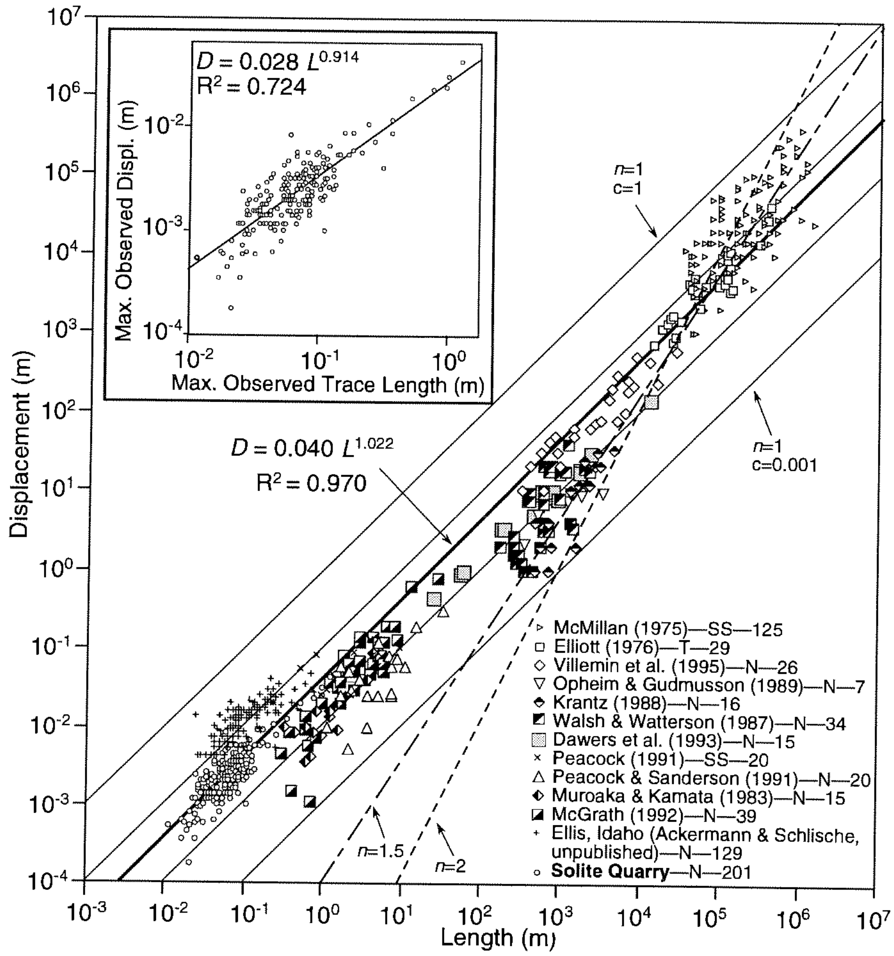

Figure 2.6: Log-log plot of displacement versus length for various published fault populations. Abbreviations are: N, normal faults; T, thrust faults; and SS, strike-slip faults. A family of linear curves (n=1) with various c-values bound the data; the best-fit curve for all the data is shown as the heavy solid line. Also shown for reference are curves for n=1.5 and n=2. Inset: Log-log plot of displacement versus length for only the small faults from the Solite Quarry, n ≈ 1.

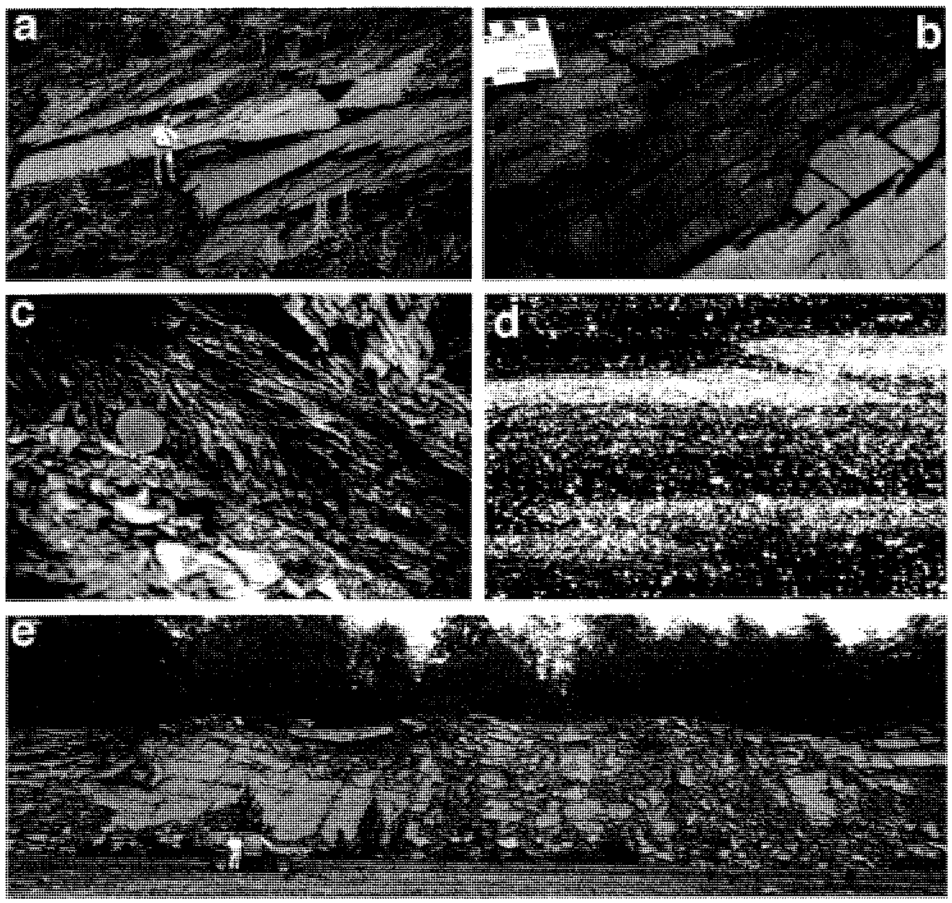

Figure 2.7

Figure 2.7: Contractional structures present at the Solite Quarry. a-d are related to inversion in earliest Jurassic time. (a) Large normal fault reactivated as a reverse fault; person's hand is on the hanging wall, feet are on the footwall. (b) Small faults present in the hanging wall of the fault in (a), where they were reactivated as normal faults. (c) Black shale layer serving as a decollemént surface, forming a series of imbricate thrust slices; lens cap for scale. (d) Thin section of one of the arthropod beds, showing small reverse faults with less than 1 mm of separation. Photo courtesy of Nick Frasier. (e) Neotectonic quarry buckles. Arrows indicate the buckle axes, which are orthogonal to neotectonic $\sigma 1$.

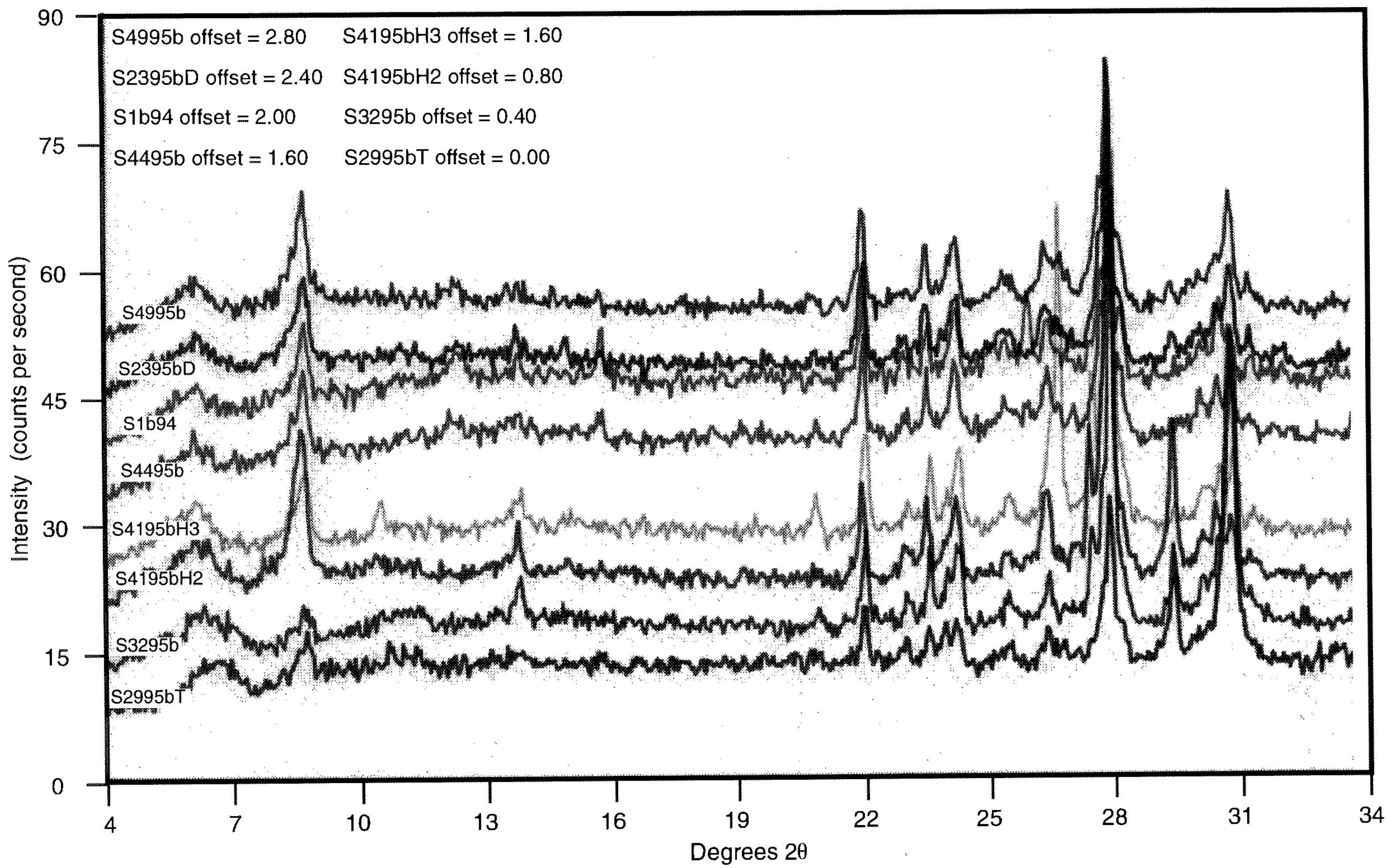

Figure 2.8: X-ray diffraction patterns for 8 of the 12 samples run from the Solite Quarry, offset along the intensity axis so they do not blot each other out. Notice how the patterns are all quite similar, generally differing only in the intensities of certain peaks. All have a strong peak at 28° 2θ, the peak for albite.

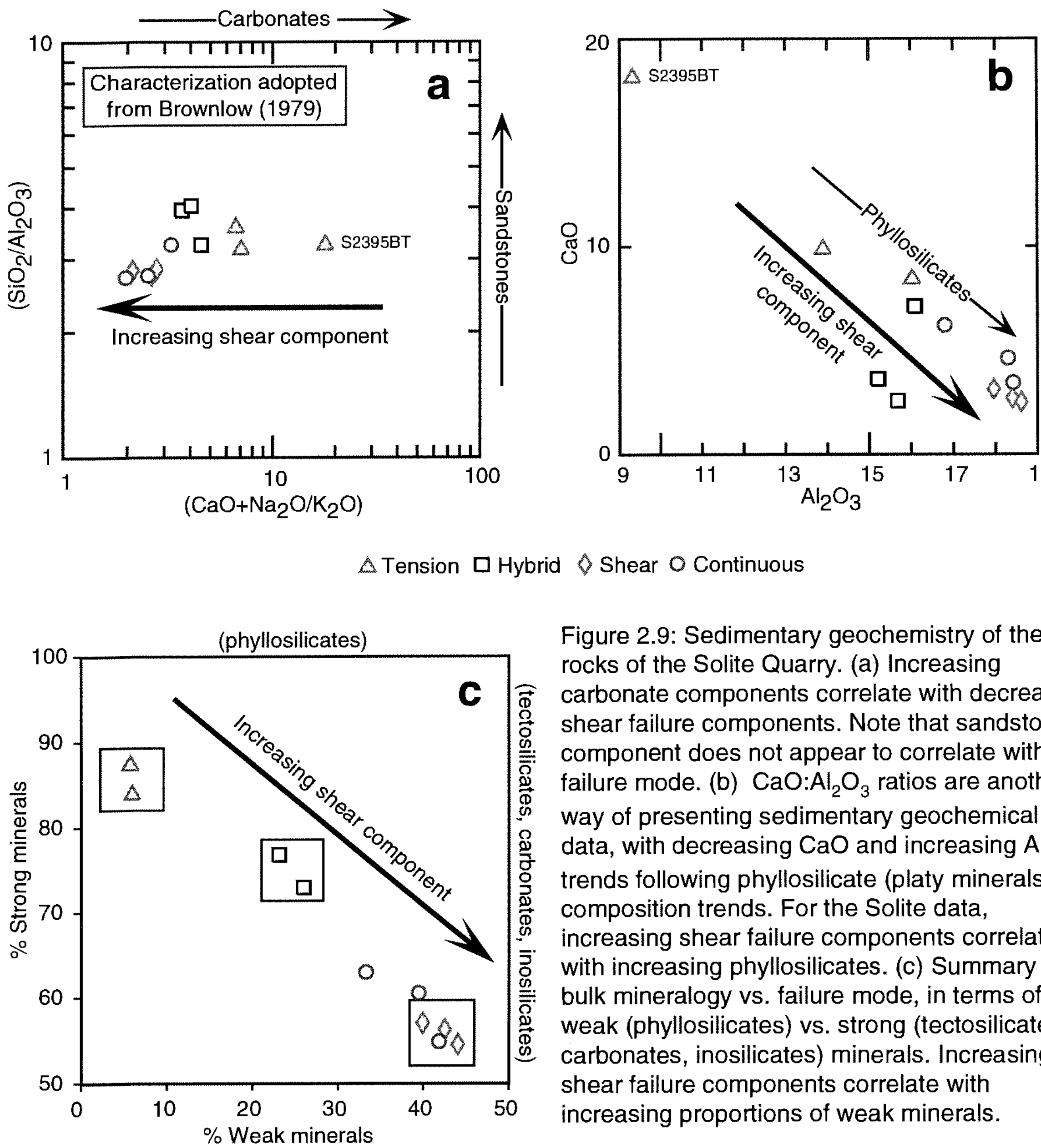

Figure 2.9: Sedimentary geochemistry of the rocks of the Solite Quarry. (a) Increasing carbonate components correlate with decreasing shear failure components. Note that sandstone component does not appear to correlate with failure mode. (b) $CaO:Al_2O_3$ ratios are another way of presenting sedimentary geochemical data, with decreasing CaO and increasing Al_2O_3 trends following phyllosilicate (platy minerals) composition trends. For the Solite data, increasing shear failure components correlate with increasing phyllosilicates. (c) Summary of bulk mineralogy vs. failure mode, in terms of weak (phyllosilicates) vs. strong (tectosilicates, carbonates, inosilicates) minerals. Increasing shear failure components correlate with increasing proportions of weak minerals.

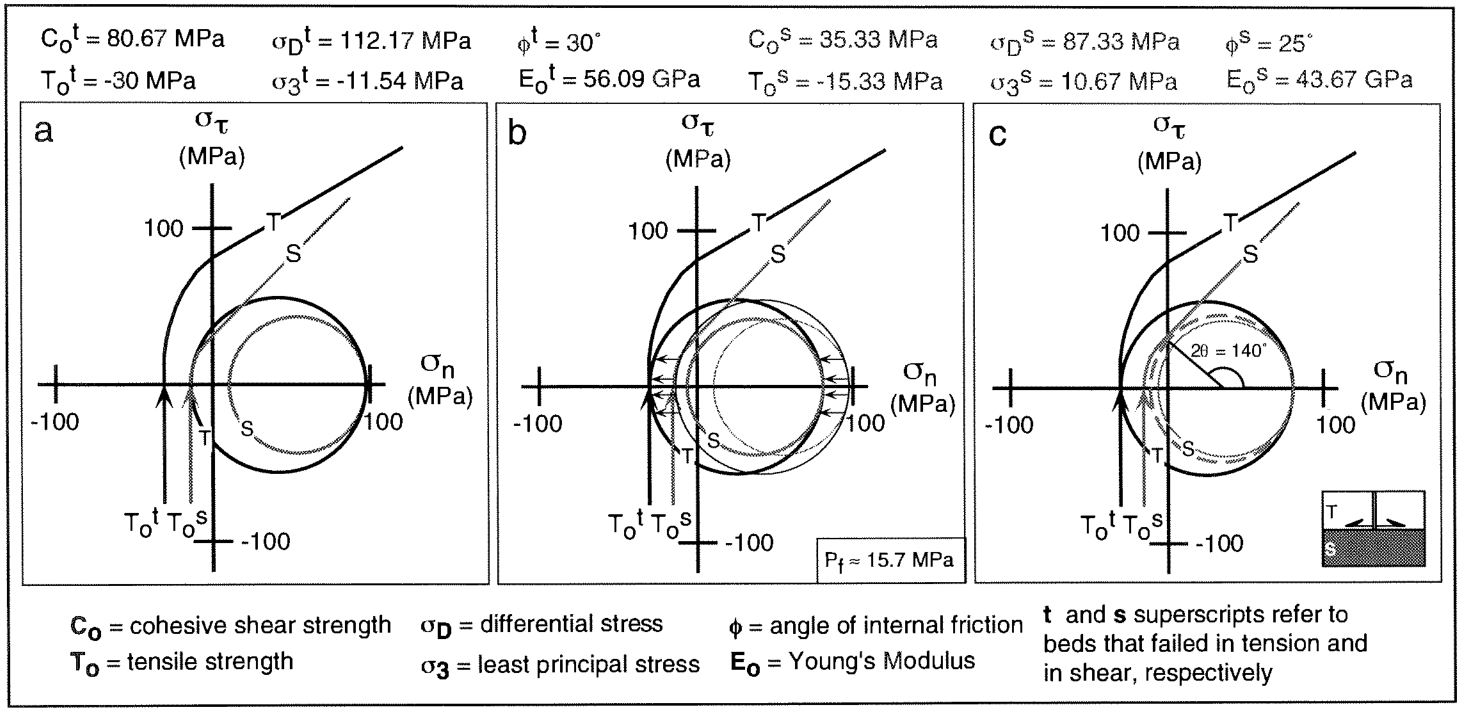

Figure 2.10: Two-component (tensile and shear) Mohr-Coulomb model for macroscopic failure of rocks from the Solite Quarry, based on mechanical analogs from the literature. The model follows the principles set forth in Gross (1995), Gross et al. (1995), and Hobbs (1967). Failure envelopes and circles are labeled with T and S, for beds that failed in tension (feldspathic sandstones) and those that failed in shear (massive siltstones), respectively. (a) Initial condition of the model, with circles for both modes residing in their respective stable fields of the Mohr diagram. (b) Condition of tensile failure after an increase in pore-fluid pressure, which drives the circles to the left. (c) Condition of shear failure after differences in elastic strains after (b) lead to an increase in the stress in the unfailed bed, due to an imposed shear traction, causing the circle to grow and intersect its failure envelope.

Figure 2.11

Figure 2.11: Spatial distribution of mode I fractures across a bedding surface. View is of the top of the bed, which is a mechanical layer boundary. Lines are scanlines along which one-dimensional strain data were collected.

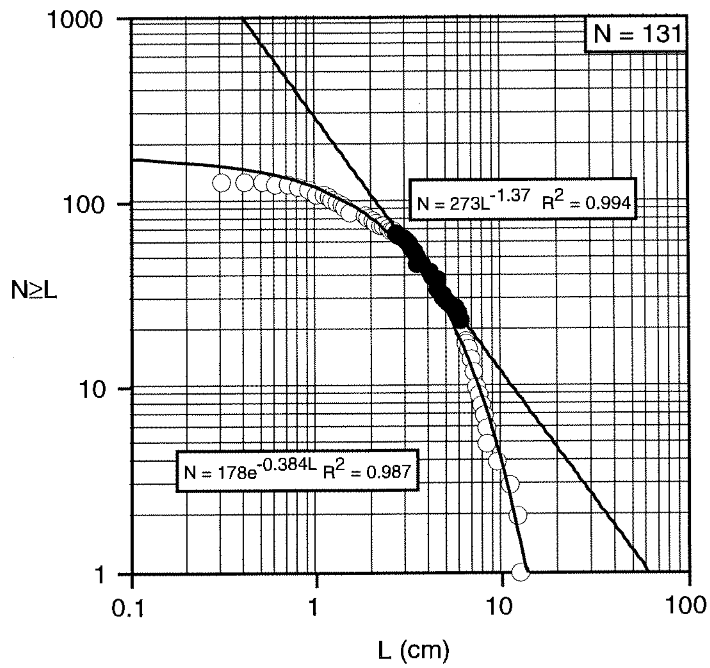

Figure 2.12: Cumulative frequency diagram of mode I fracture lengths for the bedding surface shown in Figure 11. It is not clear if there is a "flat" central segment suggestive of a power-law distribution of sizes. The data as a whole are better fit using an exponential function. If the data do indeed follow a power-law distribution, then truncation and censoring effects are severe for this sample (see discussion of Figure 2.15).

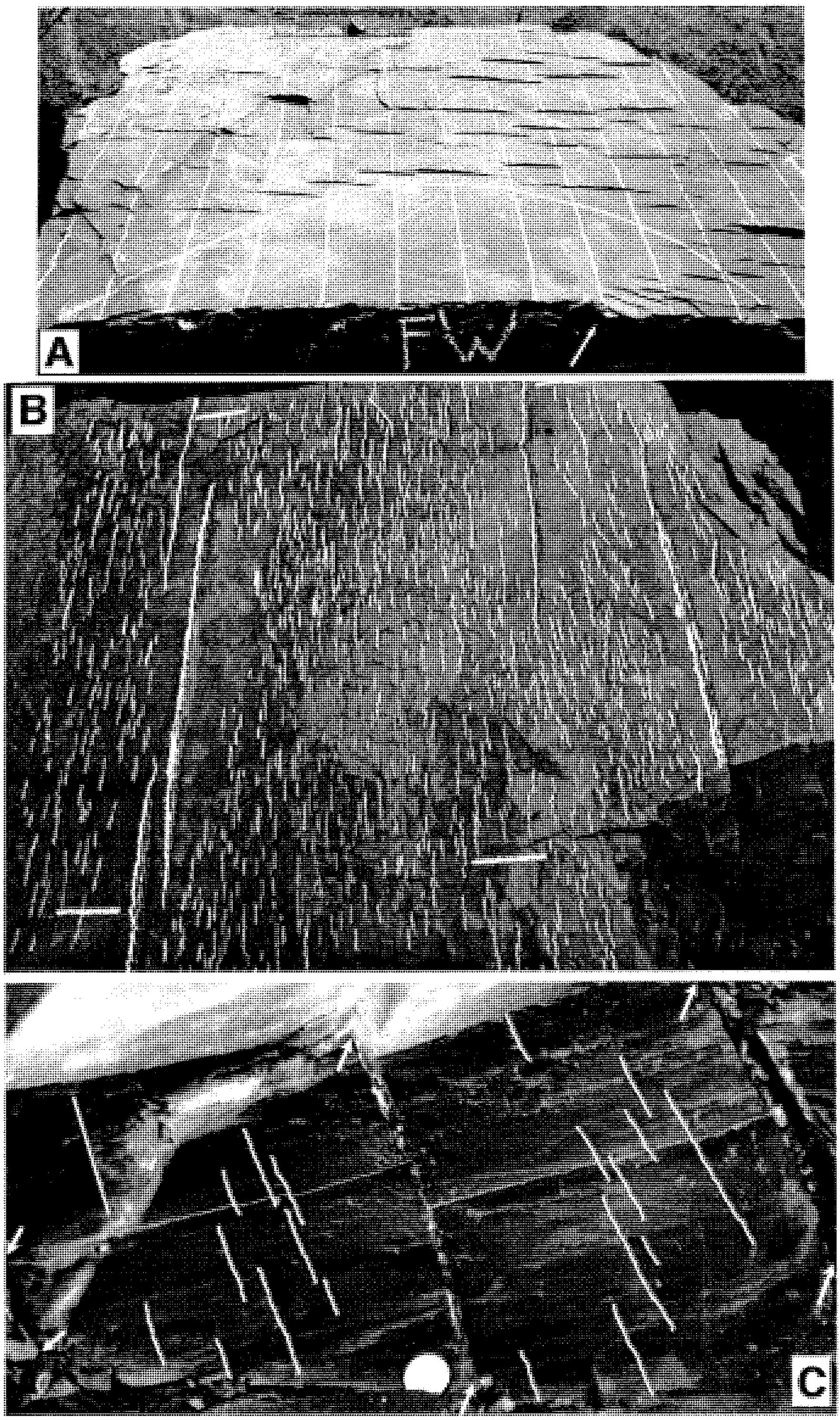

Figure 2.13

Figure 2.13: (a) Small faults anti-clustered around a larger normal fault (footwall surface shown in foreground); ruler at top of image is 15 cm wide. Notice the absence of faults within an elliptical region around the larger structure, except for where there is a breached ramp structure in the lower right (arrow). (b) Distribution of faults exposed on bedding surface of a quarried boulder. Faults are highlighted with chalk. Scale bars normal to fault traces are 10 cm long. (c) Fault shields in cross section, faults are highlighted. Arrows point to tips of master faults. Master faults and small faults offset bedding. Coin for scale.

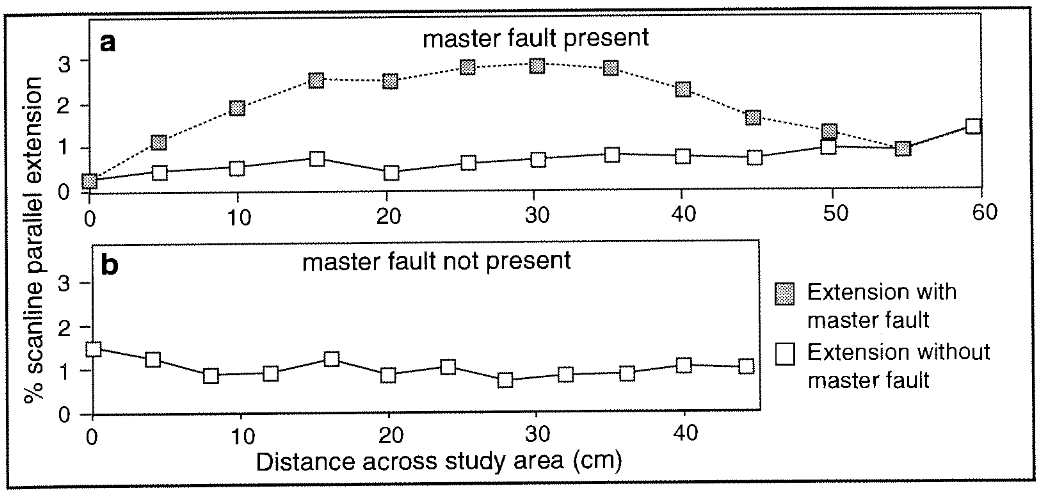

Figure 2.14: Distance-strain profiles for two study areas. Diagrams show distance across the study area (parallel to fault traces) on the ordinate, and percent scan-line parallel (fault-orthogonal) extension on the abscissa. (a) Profile for an area with a master fault present. Curves show total brittle strain. Estimates including the master fault are shown with shaded boxes, estimates not including the master fault contribution are shown with unfilled boxes. (b) Profile of an area where there is no master fault present.

CHAPTER THREE: ANTICLUSTERING OF SMALL NORMAL FAULTS AROUND LARGER FAULTS

SYNOPSIS

The Solite Quarry in the Danville rift basin contains a population of normal faults that can be subdivided into two sets based on their spatial and size distribution within the rock volume. Larger master normal faults (20 cm < L < 200 cm) are "2-D" structures, accommodate the majority of the strain, are not numerous, and have spanned the mechanical layer. The other set (~0.1 cm < L < 20 cm) consists of "3-D" structures which are ubiquitous within the rock volume, and exhibit anti-clustering with respect to the larger structures, forming "fault shields" around the master faults. The shields are ellipsoidal in shape and are geometrically similar to (although about one-quarter the predicted size of) the elastic deformation fields of the master faults, and correspond to a critical stress-reduction shadow that prevented the nucleation of smaller faults in the vicinity of the master faults. The master faults likely formed earlier than the smaller faults, which nucleated en masse when some critical strain threshold was exceeded outside the master fault deformation field.

INTRODUCTION

Thorough analysis of the spatial distribution of faults is critical to understanding the mechanics and systematics of faulting, fault growth, and fault population evolution. The ability to predict where various structures occur within the volume surrounding a large structure is integral to the construction of fractured aquifer and hydrocarbon reservoir models. Unfortunately, our understanding of the spatial distribution of faults is limited, especially compared to opening-mode fractures (e.g., Gillespie et al., 1993). Some studies have noted that smaller faults commonly cluster around larger faults (e.g., Gillespie et al., 1993; Little, 1996; Watterson et al., 1996). Jackson and White (1989) suggested that very large normal faults in the Basin and Range have a characteristic spacing, but no information is provided on the distribution of smaller-scale faults. Although the spacing of opening-mode fractures may change with increasing strain (e.g., Rives et al., 1992), most studies (see summary in Narr and Suppe, 1991) confirm that the fractures have a characteristic spacing that is proportional to mechanical layer thickness and is governed by a stress-reduction shadow, which forms because stress within the rock volume cannot be transmitted across the free surface of the fracture (Gross et al., 1995). Until now, stress shielding between faults has only been casually suggested (e.g., Cowie et al., 1996).

In this paper, we report on the spatial distribution of exceptionally well-exposed neo-formed faults from a quarry in the Danville basin in North Carolina. Here smaller normal faults are clearly anti-clustered around larger structures. We argue that this distribution is related to a stress-reduction shadow around the larger faults, and explore the effect of this spatial distribution on the size distribution of faults in the population, the implications for the temporal evolution of this fault system, and the applicability of these concepts to larger-scale structures.

POPULATION SYSTEMATICS

The population of small faults lies within the Mesozoic Danville rift basin, a half graben with an east-dipping border fault system. A detailed discussion of the geometry and length-displacement scaling relations of these faults is given in Schlische et al. (1996). These (originally) blind normal faults are readily observed on quarried, clean bedding plane partings, permitting detailed spatial analysis. They can also be observed in quarried cross-section exposures, as well as in rock slabs that have been sawed open in the lab. All of the faults have a consistent orientation (045°, 70° SE, bedding corrected) and dip synthetic to the border fault system. The strain they accommodate is related to Triassic rifting during the break-up of Pangea (Ackermann et al., 1996).

This population can be divided into two broad groups of faults based on size and distribution. Large faults (20 cm < L < 200 cm) are infrequent and essentially evenly distributed. Small faults (~0.1 cm < L < 20 cm) are generally ubiquitous within the rock volume, but are absent within ellipsoidal regions around the large faults (Figure 3.1). These regions are devoid of brittle structures. We refer to these regions as *fault shields*, and the faults they surround as *master faults*. Master faults are defined by the presence of a fault shield around them, regardless of their size. Shield geometries vary depending on linkage of larger structures. The smaller faults appear abruptly outside of the fault shields, and there is no increase in the size of the small faults away from the larger structures; rather they occur in a range of sizes with no apparent systematic variation. The small faults generally follow stepping patterns around master faults: the small faults closest to the master fault change step at the center of the length of the larger structure, as well as at the tips (Figure 3.1a). These geometric relationships provide important information about the spatial and temporal evolution of the system, specifically that the larger faults formed and grew first, and then the smaller faults nucleated.

Strain within the volume is dominated by the master faults, which have accommodated approximately 2.5% extension (Ackermann and Schlische, 1995). The small faults have accommodated only 1% extension, for a total of 3.5% extension. Analysis of multiple scanlines across fields of faults reveals that extension varies areally only when the master faults are included (Figure 2.14), mimicking the displacement profiles of the large faults (e.g., maximum displacement at the center of the fault) (Ackermann and Schlische, 1995). This differential strain accommodation thus provides a second basis for sub-division of the population.

Faults are generally believed to follow a power-law distribution of sizes such that

$$N = aL^{-C}$$

where N is number of faults with a length (L) greater than a given size, a is related to the number of faults, and C is the power-law exponent (Scholz and Cowie, 1990; Pickering et al., 1995). The power-law exponent gives the ratio of the smallest faults to the largest faults. Thus in populations with larger power-law exponents (steeper slopes), smaller faults are relatively more important in accommodating strain. The power-law exponent is determined by plotting N vs. L on cumulative frequency plots. Typically, such plots are convex upward, consisting of a single central segment (with a slope of $-C$), a shallow upper segment resulting from truncation due to sampling resolution and a steep lower segment generally ascribed to a censoring effect due to large structures extending out of the sampling area (e.g., Pickering et al., 1995).

In recent years, some workers have noted that this simple power-law distribution may not always hold. In particular, Wojtal (1994, 1996) drew attention to fault populations that have faceted central segments, i.e., central portions composed of at least two straight segments with different power-law exponents. Wojtal attributed such faceted diagrams to the effects of fault linkage during the evolution of the population. Despite the faceted appearance, the cumulative frequency plots are still convex upward. In contrast, a cumulative frequency plot (Figure 3.2) for faults from the Solite Quarry is concave upward and appears to have two central segments, both of which follow a power-law distribution. Figure 3.2 is based on the distribution of 850 fault lengths measured on a single bedding surface, which were corrected for linkage in the field following Wojtal (1996) and Dawers and Anders (1996); the data suffer from truncation and censoring effects.

The two well-defined central segments shown in Figure 3.2 suggest that there are two subpopulations, which in turn reflect the strain history of these rocks. (Removing the master faults from the analysis results in a single central segment nearly identical to the segment covering smaller fault sizes in Figure 3.2.) Interestingly, $C_m = 0.66$ for the segment covering the larger fault sizes (master faults), which is ~1 less then that of the other segment ($C_s = 1.64$). Marrett and Allmendinger (1991) observed that the value of C is critically dependant on f-s, where f is the geometric dimension of the region occupied by the faults, and s is the sampling dimension. In this example, $s = 2$ (two-dimensional sampling of observed trace lengths) for both subpopulations. The lower value of C_m thus implies that the occupation dimension (f) is lower for the master faults. We suggest that this is because all the faults in the quarry are restricted to discrete mechanical layers (see Ackermann et al., 1996), with the master faults spanning entire layers but not exceeding them. Therefore they occupy only two dimensions ($f = 2$, as opposed to the small faults where $f = 3$); this is analogous to faults that span the brittle crust, which can only grow along strike, having lost one degree of freedom (e.g., eq. 2 in Marrett and Allmendinger, 1991). This results in more complete sampling of that subpopulation using a two-dimensional sampling method (f-s = 0): all structures will be observed at all structural levels.

Using eqs. 3 - 6 in Marrett and Allmendinger (1991) (which account for faults that do and do not span a brittle layer), and a value of $n = 1$ (where n is the length-displacement scaling exponent: see Schlische et al., 1996), we calculate B_m (master faults) and B_s (small faults) based on geometric moment (M_g). B is the power-law exponent for the distribution of M_g, similar to C. $B_m = 0.83$ and $B_s = 0.88$, suggesting that the two subpopulations are intricately related, although smaller faults are slightly less important in strain accommodation for the master fault subpopulation. $B_m \approx B_s$ demonstrates that the master faults and the small faults are simply two interrelated components of a single coherent fault population. $C_s - C_m \approx 1$ in turn indicates that one subset of faults has a lower occupation dimension (f) and thus spans the mechanical layer, which is consistent with field observations.

Cumulative frequency plots are commonly used to extrapolate fault size data (following a power-law distribution) measured over a relatively narrow scale range (<3 orders of magnitude) in order to estimate the amount of strain accommodated by structures below the sampling resolution (e.g., Marrett and Allmendinger, 1992). The presence of faceted cumulative frequency plots (e.g., Wojtal, 1996) and concave-upward plots (Figure 3.2) suggests that such extrapolations should be undertaken with caution.

approximate the deformation field by the roll-over radius (R'), defined as the distance perpendicular to the normal fault affected by significant footwall uplift or hanging wall subsidence, and expressed as:

$$R' = R'_{max}\left(\frac{d}{D}\right)^{1/2}$$

where d is the displacement on the fault, and D is the maximum displacement. R'_{max} is the maximum roll-over radius, taken to be equal to the mean of the major and minor radii of the fault surface ellipse; axial ratios of normal faults generally range from 1.25 to 3 (Gibson et al., 1989).

Geometrically, the fault shield and the deformation field for a 1 m long fault are similar, although the shield is about one-quarter the predicted size of the deformation field (Figure 3.4). Because the deformation field represents a volume of rock in which the material has been relaxed (strained), it should be a proxy for a stress-reduction shadow around a fault. The fault shield therefore occupies a part of the stress-reduction shadow, specifically that portion where the stress did not exceed the shear strength of the rock. Thus, it would be possible to have brittle failure within the deformation field of a fault but not in the volume in the immediate vicinity of the fault, the size of which is governed by the size of the fault and material properties; strain rate is likely to be important as well.

The interpretation that the fault shields correspond to a critical stress-reduction shadow is bolstered by the following: (1) As noted above, there is an almost complete absence of brittle structures within the fault shields, yet small faults are ubiquitous elsewhere. (2) The geometry of the fault shield is very similar to the stress-reduction shadow for an opening-mode crack calculated using finite-element modeling (Gross et al., 1995). The distance over which stress is recovered away from an opening-mode crack is a function of the applied load, Young's modulus, shear modulus, bed thickness, and the elastic strain at which the first joint forms (dependent on size of the initial flaw) (see Gross et al., 1995, eqs. 1-3). The relationships are in detail not appropriate for faults because they are based on the inability of stress to be transmitted across the free surface of an opening-mode crack. Nonetheless, the geometric similarities suggest that similar phenomena (stress-reduction shadows) are associated with both faults and opening-mode fractures. (3) The idealized fault shield shown in Figure 3.4 lies within the region of highest stress-reduction associated with seismic slip on a fault as calculated by Das and Scholz (1982); see also Scholz (1990, his fig. 3.27). Although the Das and Scholz (1982) model was specifically constructed for a strike-slip fault, this should also be applicable to normal faults. In addition to calculating areas that have experienced stress-reduction, the Das and Scholz (1982) model predicts regions that experience an increase in stress. The highest stresses are found near the tips of the faults. This may lead to the preferential development of smaller faults in these areas, some of which may be incorporated into the process zone as the fault tips propagate during growth. The higher density of faults in these areas may also explain why some authors have reported clustering of smaller faults near larger faults (e.g., Gillespie et al., 1993; Little, 1996; Watterson et al., 1996). We note that our fault shield geometries break down in areas where master faults have linked together; prior to linkage, these areas may have had higher numbers of smaller faults surrounding the fault tips.

DISCUSSION

The two distinct subsets of the fault population in the Solite Quarry provide specific information about the spatial and temporal evolution of this population. We interpret the deformation history here as follows: (1) A set of faults formed from random flaws within the rock volume in response to a remote applied stress (Triassic rifting). These grew and linked through time, elastically interacting at both short and long ranges (see also Cowie et al., 1993, 1995). Given the variable sizes of the master faults, it is unlikely that all nucleated at the same time. Rather, new faults continued to nucleate while older faults grew, some of which linked together. The younger faults probably continued to nucleate at random flaws, the only constraint being that younger faults would not nucleate in the fault shields of the older faults. (2) At some point, an elastic threshold was exceeded within the rock volume, perhaps related to the amount of elastic shear strain that can be accommodated prior to brittle failure, or corresponding to the stage when the tips of the master faults reached mechanical layer boundaries. At that point, the original set of faults was no longer sufficient to accommodate the strain, which necessitated the mass nucleation of a second set of faults. However, the deformation fields/stress-reduction shadows of the original set of faults governed the spatial distribution of the new faults so that they did not form within regions surrounding the larger structures where either (a) the stress was not great enough to exceed the shear strength of the rock or (b) elastic strain accommodation was sufficient enough such that an elastic threshold was not exceeded. Thus the smaller faults are relatively late stage features, although they formed over multiple slip events (Schlische et al., 1996).

The system discussed here is much simpler than the vast majority of systems studied, which are of much larger scale. However, because the mechanics and processes of fault growth are scale invariant (e.g., Cowie and Scholz, 1992; Schlische et al., 1996), the analysis of these fault shields provides important insights into faulting at all scales. It may be that stress-reduction shadows and fault shields can only be observed at small scales, at low strains, in simple settings. At larger scales and strains, it may not be possible to accommodate all of the strain in the deformation field elastically, with loading, erosion, and isostasy providing additional complications. Nonetheless, if our current understanding of faulting is correct, then it may be that even large fault zones are surrounded by some region that is less deformed, or that shows a radial increase in fault size which formed as the stress-reduction shadow of the larger structure slowly engulfed and de-activated smaller structures as it grew through time.

Eventually, the largest faults will grow to such a size that they completely cut through a mechanical layer (whether it is a single sedimentary layer or the brittle crust). At such a time, these large faults will no longer propagate up-dip and down-dip, but will continue to propagate along strike. The effect of this is that the ellipticity of the fault surface will increase, and the displacement profile will change from bell-shaped to flat-topped (see Dawers et al., 1993); increased rates of along-strike propagation may lead to an increase in lateral fault linkage. Because the fault shield/stress-reduction shadow scales with displacement, and because the maximum displacement no longer increases significantly once the fault has broken through a mechanical layer, the end result of this evolutionary scenario is a series of large faults with a quasi-regular spacing, which itself is a function of mechanical layer thickness, maximum displacements, and stress-reduction shadows. As noted in the introduction, the large basin-bounding faults in the Basin and Range have a characteristic spacing that Jackson and White (1989) speculated was a function of the thickness of the seismogenic layer.

In summary, the exceptionally well-exposed population of small faults in the Solite Quarry provides an opportunity for detailed spatial, temporal and kinematic analyses. The results of these analyses suggest that there are two discrete yet closely related subsets to this particular population, and more importantly suggest the existence of stress-reduction shadows around neo-formed normal faults, similar in concept to stress-reduction shadows around opening mode cracks. In this example, remnants of the shadows have been preserved as fault shields around larger structures that are devoid of meso- and microscopic faults. We suggest that the spatial distribution of neo-formed normal faults is governed by stress-reduction shadows approximated by the deformation fields of these structures, the rate of stress recovery away from the fault (governed by rock properties), and the short- and long-range elastic interaction between faults (e.g., Cowie et al., 1993, 1995).

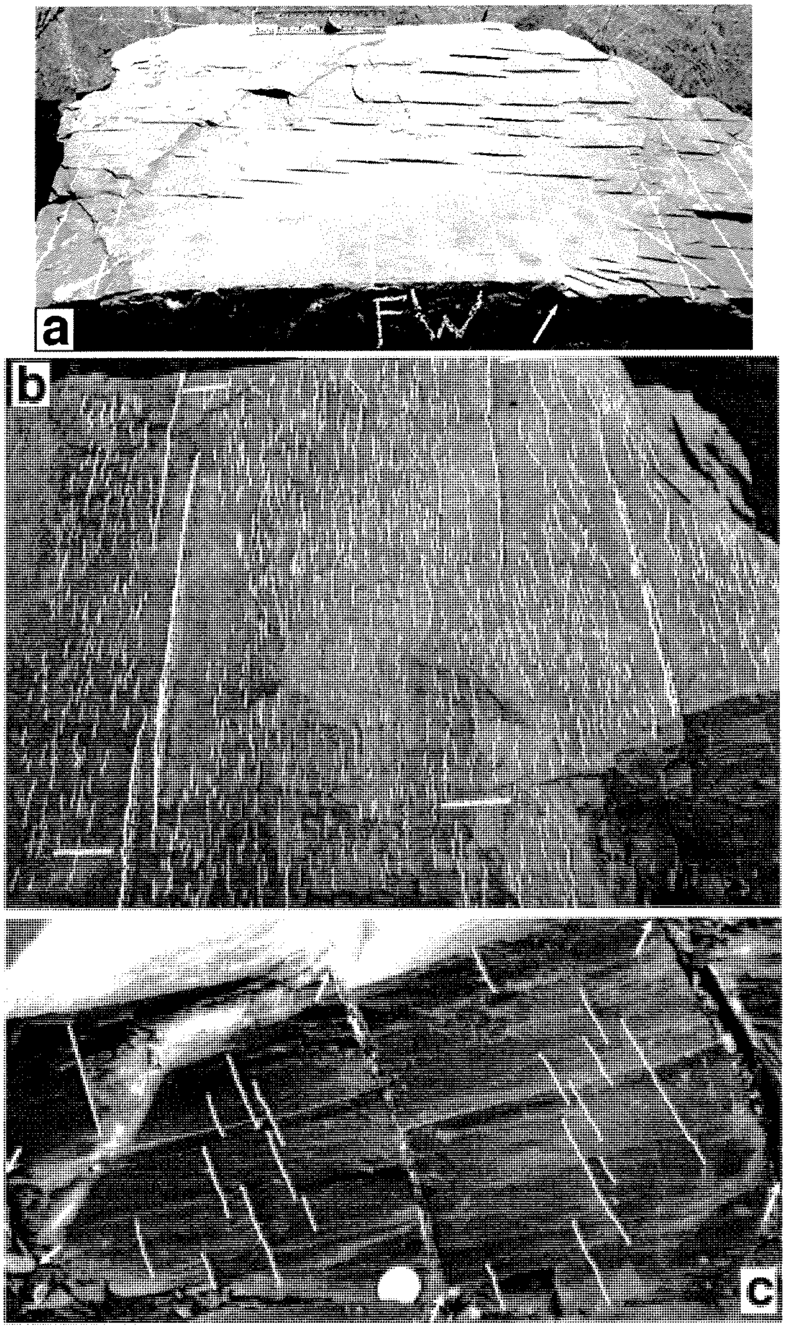

Figure 3.1

Figure 3.1: (a) Small faults anti-clustered around a larger normal fault (footwall surface shown in foreground); ruler at top of image is 15 cm wide. Notice the breached ramp structure in the lower right (arrow). (b) Distribution of faults (highlighted) exposed on bedding surface of a quarried boulder. Scale bars normal to fault traces are 10 cm long. (b) Fault shields in cross section, faults are highlighted. Arrows point to tips of master faults. Coin for scale.

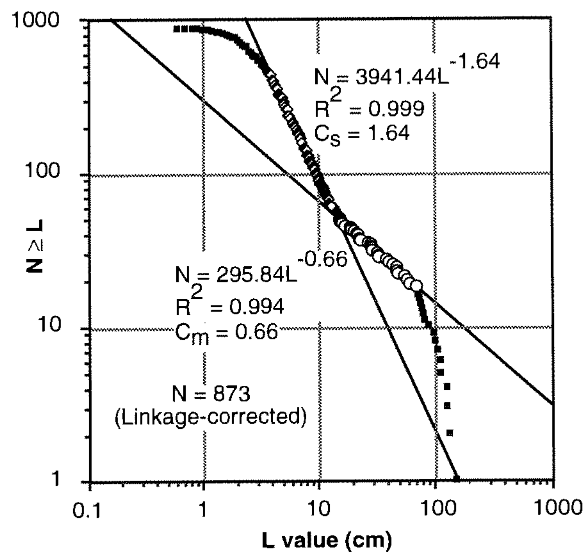

Figure 3.2. Cumulative frequency plot of fault lengths for all structures within a ~34 m^2 area. Note the two distinct central segments, suggesting two subsets of faults, with slopes that differ by ~ 1.0. Subscripts of *m* and *s* are for master faults and small faults, respectively.

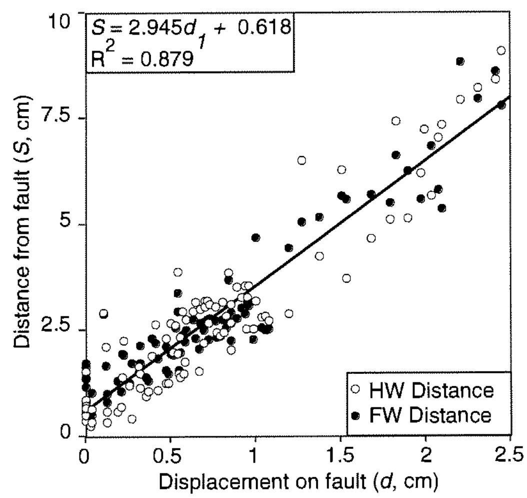

Figure 3.3. Linear relationship between local displacement and fault shield projection distance for master faults from this population.

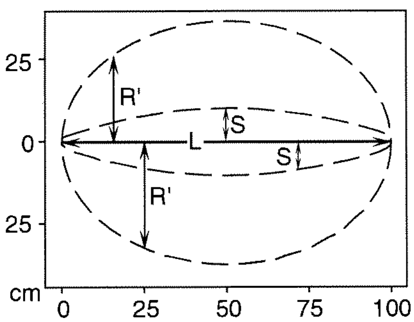

Figure 3.4. Map view of a simple model for the relationship between the deformation field and fault shield at the center of an isolated, blind, neo-formed normal fault. The extent of the fault shield will vary with rock properties and strain rate, and terminates where the stress locally exceeds the shear strength of the rock. L = 100 cm, d_{max} = 3 cm, axial ratio = 2 (Gupta and Scholz, 1996).

CHAPTER FOUR: SYSTEMATICS OF AN EVOLVING POPULATION OF NORMAL FAULTS IN SCALED PHYSICAL MODELS

SYNOPSIS

An understanding of the spatial and temporal evolution of fault systems in terms of population systematics can aid in the structural evaluation of an area. Unfortunately, existing fault populations represent only the end result of a multistage evolutionary development. Scaled physical models provide a means to learn more about the temporal and spatial evolution of fault systems (within certain boundary conditions). The model discussed here is of simple brittle extension of a homogeneous medium (wet clay) over a discontinuity (latex sheet).

Examination of the population systematics of this model reveals that there is a major shift from a power-law distribution of fault sizes to an exponential distribution. This shift is coincident with a linkage event and a leveling-off of the rate of increase of average fault length. The shift becomes evident in the map pattern of the model after a lag time: faults become more regularly spaced and change from a self-similar spatial clustering distribution to a uniform (not random) spatial distribution. A scanline-based analysis technique appears to be more sensitive to this shift than an area-based method.

These changes are hypothesized to have occurred when the majority of faults exceeded their mechanical layer, changing from unbounded (3-D) to bounded (2-D) structures. This retards long-range elastic interaction between faults, which in turn suppresses spatial correlations and power-law scaling. It would appear that thickness of the faulted mechanical layer is the controlling factor in how fault sizes are distributed and spatially correlated. Systems in thinner mechanical layers will reach the transition from power-law to exponential distribution and the transition from spatial clustering to a uniform distribution at lower strains than those in thicker layers.

INTRODUCTION

Fault population systematics integrates data on strain accommodation, fault geometries, scaling relationships, and the size and spatial distributions of faults. The systematics of a structural system reflect its framework and history, both of which are crucial to petroleum and groundwater investigations. Studies of fault populations have recently received considerable attention, marked by a special issue of the *Journal of Structural Geology* in 1996 (see Cowie et al., 1996). Numerous studies in the past five years have focused on different facets of fault population studies, and how they are affected by factors such as fault type (e.g. Wojtal 1994), geologic setting (e.g. Cowie et al., 1995; Gross et al., 1997a), fault linkage (e.g. Trudgill and Cartwright, 1994; Cartwright et al., 1995; Dawers and Anders, 1995; Wojtal, 1996), and mechanical stratigraphy (e.g. Gross, 1995; Ackermann et al, 1997; Ackermann and Schlische, 1997; Gross et al., 1997b), among others. However, existing fault populations represent only the end result of a multistage evolutionary development, and an understanding of the spatial and temporal evolution of fault systems in terms of population systematics can aid in the structural evaluation of an area. In order to study the temporal evolution of fault systems, we could examine different populations representing different amounts of strain, and assume that 1. increasing strain correlates with increasing time, and 2. different populations in different geologic and tectonic settings behave the same. Other options include the use of numerical models (e.g. Cowie et al., 1993; 1995), geometric models (e.g. Cladouhos and Marrett, 1996), or scaled physical models, the latter of which is the topic of this paper.

The utility of scaled physical models (both sand and clay) for the study of tectonic processes has been well established by workers such as H. Cloos (1929), E. Cloos (1955, 1968), Hubbert (1937), Eisenstadt et al. (1995), and McClay (1996). However, until now time-series analysis of model runs using fault population statistics has not been performed. The goal of this study is to determine if this is a feasible practice. Ultimately, studies of the how the temporal evolution of fault systems varies with varying boundary conditions could be invaluable to our understanding of how fault systems evolve both spatially and temporally. The model analyzed here is of simple brittle extension of a homogeneous medium (wet clay) in order to best evaluate the applicability of scaled physical modeling to studies of fault population systematics.

EXPERIMENTAL AND ANALYTICAL METHOD

The experimental apparatus is located at the Mobil Exploration and Production Technology Center in Dallas, Texas, and consists of four vertical plexiglass walls and a horizontal base (Figure 4.1). One of the walls is moveable to produce either extension or contraction; movement is achieved with an electric cylinder controlled by a computer. A portion of the horizontal base is moveable along a 45° incline, although this motion was not used in this experiment. Two overlapping metal plates are attached to the moving wall and its opposite (Figure 4.1). A latex (Hygienic Corp., medium gage) discontinuity covers the region of overlap, attached with 3M #131NA duct-tape. The area of stretchable latex corresponds to the area of the model where faulting occurs (fault generation zone). The analog media used was 50% weight H_2O clay, consisting of powdered kaolin, nepheline-syenite, and flint ≤ 0.1 mm in diameter. The clay is mixed to a predetermined density (~1.67 g/cm^3, following Sims, 1993), applied over the latex discontinuity (Figure 4.1), homogenized, and then smoothed.

In order to ensure that scaled physical models maintain geometric and kinematic similarity to actual rock deformation, the strength of the modeling media and the dimensions of the model must be scaled down correctly (Hubbert, 1937). The geometric scaling factor of the model is ~1:10^5; hence this 1.3 cm thick model corresponds to ~1.3 km of average crust. The cohesive strength of the clay is ~10^{-4} MPa (Sims, 1993); the clay is therefore ~10^5 times weaker than rock. Even though the physical model is scaled down, it is critical to note it is not an *exact* scale model, and that there are many differences with natural systems, most notably constant strain rate (1 cm/hour) and (relatively) homogeneous media.

The width of the discontinuity prior to deformation was 12 cm; 3.95 cm of extension was imposed to achieve a total ~33% extension. The model was illuminated from the side opposite the moving wall (Figure 4.1) using a high-power light source directed through the plexiglass wall, and photographed using Kodak Ektachrome 160T tungsten-balanced 35 mm slide film in a semi-automatic Minolta SLR camera at 0.15 cm increments (9 minute intervals). The camera was fixed above the model so as to provide a map view of the evolving fault system with a fixed frame of reference (fixed walls). Images representing times 8 - 14 (9.167% - 20.433% extension) are discussed here. These images correspond to the first image with enough faults to analyze and the last image structurally simple enough for this preliminary investigation.

The 35 mm slides from the model run were scanned as grayscale at 4000 dpi using a ScanMaker 35t*plus* slide scanner and Adobe PhotoShop (image manipulation) software. PhotoShop was then used to crop the images down to only the faulted region and to reduce the file size. Files were then imported into Canvas (technical drawing) software as *.*tiff* files at 2540 dpi (the highest resolution readable by Canvas). The final image of the model run was used to select the study area, omitting the edge effect (Figures 4.2 & 4.11). Edge effects are the inadvertent results of the boundary conditions of the model, in this case the effects of friction along the rigid side walls of the modeling apparatus (Eisenstadt et al., 1995). The box in Figures 4.2 - 4.11 always covers the same area of the model. The fault scarps show up either as bright (top- or fixed-wall dipping) or dark (bottom- or moving-wall dipping) regions, and were traced in Canvas, color coded by dip polarity to produce the fault maps in Figures 4.2 - 4.11. These fault maps and the derivative centroid maps are the basis of all the analyses presented here.

Fault trace lengths were corrected for linkage following Dawers and Anders (1997), such that synthetic faults with an overlap to separation ratio > 3 were considered soft linked (acting kinematically as one fault, although there is no visible through-going fault surface). Many of the faults in the model are parallel and never linked. Hence only faults whose tips were "approaching" each other and/or still had a chance of hard linking were considered for linkage correction. The number of faults that appeared, linked, and grew in length were counted for each image. Number that linked and number that grew were normalized to the total number of faults from the previous image; this assumes that newly appeared faults have had little effect on these processes.

The distribution of fault sizes (in this study, lengths) in a population is regularly analyzed using cumulative frequency analysis where the number of faults greater than or equal to some trace length ($N \geq L$) is compared to L. Fault populations follow one of two distributions of fault sizes. Continental fault populations appear to generally obey a power-law distribution of sizes such that

$$N(L) \approx aL^{-C}$$

where N is the total number of faults with dimensions greater than or equal to some length (L), a is a constant related to the size of the population, and C is the power-law exponent (e.g. Kakimi, 1980; Marrett and Allmendinger, 1992; Scholz et al., 1993; Wojtal, 1994; Pickering et al., 1995). The power-law (or fractal) distribution is thought to be the result of short- and long-range elastic interaction between structures (Cowie et al., 1993; 1995). For example, Cladouhos and Marrett (1996) have developed a geometric model for the growth of a system where fault linkage is a key mechanism; they maintained a power-law distribution of fault sizes based on faults being able to "feel" each other elastically. The result is a fault pattern containing strong spatial correlations, which is therefore fractal (Cowie et al., 1993, 1995). The size data are presented as plots of $N \geq L$ vs. L in log-log space. There are usually three distinct segments to the curve (e.g. time 6 & 7 in Figure 4.17). The upper segment is due to data truncation (Pickering et al. 1995), representing under-sampling of structures below the observation limit of the sampling method used. The lower segment is a censoring effect, representing under-sampling of larger structures because they extend beyond the study area, but may also be due to truncation - extremely large structures are undersampled because they do not intersect the study area (Pickering et al., 1995). Cladouhos and Marrett (1996) suggested that this segment may be due to long faults not being able to grow at a rate sufficient to maintain a power-law distribution. The central segment bounded by inflection points is of primary interest. The slope of this segment (C) describes the distribution of fault sizes in the population; it gives the ratio of small to large structures. C is sometimes referred to as the fractal dimension or power-law exponent (Main, 1996). Steeper slopes (thus greater values of C) indicate that smaller structures are relatively more important than larger structures in strain accommodation (Scholz and Cowie, 1990).

Cowie et al. (1994) have found that the size distribution of normal faults in oceanic crust is best described by an exponential function, although in the zone of active faulting immediately adjacent to the ridge (±10 km), a power-law distribution is more appropriate (Cowie et al., 1994). The function is given as

$$N(L) \approx N_T e^{-\lambda L}$$

where N_T is the total number of measurements, and λ is inverse of $\langle L \rangle$, the mean value of L. λ is also the slope of the best-fit line to the data. The definition of a mean value or characteristic size is a diagnostic feature of exponential distributions (Cowie et al., 1994). The overall exponential distribution in oceanic populations is probably a result of a lack of spatial correlation in the system due to the relatively narrow fault generation zone at midocean ridges, and the rafting and deactivation of fault packages (which may individually exhibit power-law distributions) as new crust is formed. This in turn suppresses the short- and long-range interaction of structures that gives rise to power-law (fractal) distributions (e.g. Cowie et al., 1994).

Spatial clustering of fault centroids (taken as the center of the trace length) was assessed following the method outlined in Dawers and Malinverno (1997), where the distance r from a scanline (positioned in the center of the study area, parallel to the extension direction, see Figure 4.2) to each centroid is measured. The number of centroids within a distance r from the scanline is given as:

$$N(R) \propto r^{\psi}$$

where ψ is the clustering dimension (ψ=1 indicates a random distribution according to Dawers and Malinverno 1997; 0<ψ<1 indicates self-similar spatial clustering) in the strike direction (normal to the scanline). This study will also explore this principle using a scanline normal to the extension direction (also in the center of the study area), yielding ψ', the clustering dimension in the extension (dip) direction. Potential shortcomings of this method include biases due to placement of scanlines as well centroids not being weighted by their lengths.

Uniformity and randomness of the spatial distribution of points (centroids) were analyzed using grid-based χ^2 methods outlined in Swan and Sandilands (1995). Although it would be possible to weight structures by their length using these methods, it was not done for this study in order to keep the investigation relatively simple. The following summary of the methods is based on Swan and Sandilands (1995). Uniformity in a point distribution implies a lack of independence of points (in this case, fault centroids) from each other, hence the establishment of a point (fault) changes the probability of another fault developing in its vicinity. Uniformity also implies homogeneity in the geologic medium. Uniformity of the point distribution is assessed as:

$$\chi_u^2 = \frac{1}{E}\sum_{j=1}^{k}(O_j - E)^2$$

where k is the number of subareas (grid cells), and E is the total number of points divided by k. E thus represents the condition in which each cell contains the same number of centroids. χ_u^2 is a comparison of the observed point distribution (O_j) with E. This is compared to χ_{uc}^2, the critical χ_u^2 required to nullify a hypothesis of a uniform distribution. χ_{uc}^2 is based on the number of degrees of freedom (grid cells) and a 5% level of significance. If $\chi_u^2 > \chi_{uc}^2$ the point distribution is not uniform.

Randomness in a point distribution also implies homogeneity of the geologic medium, but more importantly implies independence of points (fault centroids) from each other. Thus the geologic process determining the positions of points is blind to the positions of other faults. Randomness is assessed by comparing the observed point distribution (O_j) to an expected Poisson distribution (E_j) as:

$$\chi_r^2 = \sum_{j=1}^{k} \frac{(O_j - E_j)^2}{E_j}$$

where

$$E_j = Te^{-n/T} \frac{(n/T)^j}{j!}$$

and O_j is the number of subareas (grid cells) that contain j points. The Poisson distribution is based on the total number of points (n) and the number of grid cells (T). As in the uniformity test, χ_r^2 is compared to χ_{rc}^2, which is calculated in the same manner as in the uniformity test. If $\chi_r^2 > \chi_{rc}^2$ the distribution of points is not random. Non-random point distributions trend in either the direction of clustering or uniformity (Swan and Sandilands, 1995). Thus, by applying both spatial uniformity and randomness tests, we can check for spatial clustering independently of the ψ method outlined above in two sampling directions (sampling over an area), whereas the ψ method utilizes only one sampling direction (sampling along a scanline).

RESULTS

Table 4.1 presents the model image sequence in terms of time, imposed heave, and imposed extension. Brittle deformation in the model does not become apparent until about ~6.6% extension due to two factors. First, early in the model run strain is likely accommodated continuously until the stress in the media exceeds the critical stress required to achieve brittle failure. Second, the faults propagate upward from the base of the model, nucleating at the interface between the latex sheet and the clay (Withjack and Jamison, 1986). They eventually break the free surface of the model, which is the structural level studied here. They grow both in length and displacement, interacting and linking with each other. The faults are consistently oriented at ~90° to the extension direction with pure dip-slip motion. Fault dips average around 60°, with mixed dip polarity. Because we are interested in how the population of faults evolves through time, we will concentrate on how the map pattern and fault statistics change with time, focusing on those times where significant changes take place.

Figures 4.2 - 4.11 show the ten time slices (8 - 14) of the model discussed here, from ~9% to ~21% extension. The map pattern of the model evolves fairly gradually with increasing strain, and is best examined in light of the fault statistics that will be discussed later in this section. At time 5 (Figure 4.2) enough faults had broken the surface to collect sufficient data for population analysis. Time 7 (Figure 4.4) marks the beginnings of a through-going fault system in the central region of the study area that will eventually form a well-developed graben at time 9 (Figure 4.6). A weakly right-stepping fault pattern begins to become apparent at time 10 (Figure 4.7), and persists through time 12 (Figure 4.9). Time 10 also marks the beginnings of a second through-going full graben system toward the top of the model, which is fully developed by time 13 (Figure 4.10). At time 11 (Figure 4.8), approximately half the area of the model is cut by faults, although there is a "blank" area near the bottom left of the model. At this point in the model run, it is apparent that most of the brittle deformation is concentrated in the central (measured in the extension direction) two-thirds of the model. Approximately two-thirds of the model surface is cut by faults at time 13, with the "blank" area persisting. By time 14, the "blank" area fills in, about three-quarters of the model surface is cut by faults, and most of the brittle deformation is still concentrated in the central two-thirds of the model.

Figure 4.12 shows the total number of faults, the average length ($\overline{L}$) of all faults, and the summed length ($\sum L$) of all faults through time (increasing strain). The total number of faults and $\sum L$ increase steadily through time, but $\overline{L}$ first increases rapidly until time 8 when it levels off, not increasing again until time 13. The absolute number of newly appeared faults follows the trend of the total number of faults (Figure 4.13), except for time

13. The absolute number of faults that linked and the absolute number that grew also generally increase with increasing strain, although there is a noticeable spike in the number that linked at time 8. Figure 4.14 presents the same data as Figure 4.13, but the number of faults that linked and the number that grew have been normalized to the total number of faults present in the previous time step; the number of newly appeared faults has been normalized to the total number of faults in the current time step. Normalization changes the trends significantly: now the normalized number of newly appeared faults generally decreases through time, although there is a small bump at time 10. The normalized number that linked increases rapidly until time 8, after which it drops and then levels off. The normalized number of faults that grew through time appears to generally increase and then decrease, with the exception of time 7. Figure 4.15 compares the normalized linkage, growth, and newly appeared fault data with average fault length through time. The spike in the linkage trend corresponds with the levelling off of $\overline{L}$ at time 8.

Figure 4.16 presents data on the spacing of faults along four scanlines parallel to the extension direction, positioned at a regular intervals (9.2 cm) across the study area. The average fault spacing (equivalent to fault block width) decreases steadily with increasing strain, although there is a slight increase at time 10. This slight increase reflects faults appearing at long range, and corresponds with a slight increase in the normalized number of newly appeared faults. There is clearly an inverse relationship between the total number of faults and the average spacing through time. The average standard deviation of the spacings increases rapidly to a peak at time 10, then decreases at a rate comparable to that of the average spacing.

Results of the cumulative frequency analysis of fault lengths are presented in Figure 4.17. With increasing strain, the curves fall higher and increasingly to the right of the diagram, consistent with increasing numbers of faults and increasing fault trace lengths. There is a change in the character of the curves between times 7 and 8, when the general shape of the curves changes from weakly concave-up to strongly convex-up. Times 5 - 7 have a form consistent with a power-law distribution of fault sizes, and are best fit using a power-law function. Times 7 - 14 are better fit using an exponential function. The exponents (power-law and exponential) are shown graphically through time in Figure 4.18. The power-law exponent (C) of early time steps decreases with increasing strain, signifying a change in the relative importance of small vs. large faults in strain accommodation, with small faults becoming relatively less important. This has also been noted in the numerical models of Cowie et al. (1995) and in the geometric models of Cladouhos and Marrett (1996). After the shift from a power-law to exponential distribution of fault sizes at time 8, the exponential exponent (λ) remains constant until time 10, after which it steadily decreases. The change in the type of size distribution is coincident with leveling off of $\overline{L}$ at time 8 (Figure 4.18), as well as the spike at time 8 in the normalized number of faults that linked (Figure 4.19). The characteristic or mean fault length ($\langle L \rangle$) derived from λ is also shown on Figure 4.18, and is consistently less than $\overline{L}$. Interestingly, $\langle L \rangle$ follows the trend of $\overline{L}$ quite closely; the two may even be convergent after time 10.

The scanline-based clustering analysis was performed both parallel and normal to the extension direction, yielding a clustering dimension (ψ) for the along-strike direction, and a clustering dimension (ψ') for the dip direction. $N \leq r$ and $N \leq r'$ curves for the model run are shown in Figure 4.20, and values of ψ and ψ' through time are shown in Figure 4.21. For times 5 - 9, $\psi << 1$, implying self-similar spatial clustering of fault centroids in the along-strike direction. For times 10 - 14 $\psi \approx 1$, suggesting that, according to this method, there is a random distribution of centroids in the along-strike direction. Throughout the model run $\psi' \approx 1$, suggesting that there is a random distribution of fault centroids in the dip direction. In Figure 4.20, there is a noticeable inflection in the curve at $r' \approx 4$ cm that is persistent through the model run. The area covered by $r' \approx 4$ cm is shaded in Figures 4.2 - 4.12, and corresponds to the region of the model where the majority of the visible faulting occurs. This area is narrower than the fault generation zone (discontinuity), but may nonetheless be an artifact of the model set-up.

The χ^2 test for uniformity of the spatial distribution of centroids consistently resulted in confirmation of the uniformity hypothesis for the entire model run ($\chi^2_u < \chi^2_{uc}$). The χ^2 test for randomness in the spatial distribution of centroids (Poisson distribution) consistently resulted in nullification of the hypothesis of randomness for the entire model run ($\chi^2_r > \chi^2_{rc}$). The failure of the randomness test contradicts the results of the ψ and ψ' analyses (both of which were for only one direction/dimension). Recall that if the spatial distribution of points is non-random, it can trend either in the direction of uniformity or clustering. Because uniformity was confirmed for all time steps, these tests suggest that there is no clustering in the model (over an area). This conflicts with the ψ analysis of time steps 5 - 9.

DISCUSSION

The shift from power-law to exponential distribution and mechanical layer thickness

It is readily apparent from the preceding summary of the data acquired from this model run that time 8 is significant. There are major changes in the trends of average fault length ($\overline{L}$) (levelling off) and the number of faults that linked (reversal) (Figure 4.15). There is also a shift from a power-law to an exponential distribution of fault lengths (Figures 4.17 - 4.18) at time 8. Populations of bounded faults (3-D structures, e.g. continental populations) typically follow a power-law distribution, whereas populations of unbounded faults (2-D structures, e.g. oceanic populations) generally follow exponential distributions (see Introduction). Cowie et al. (1995) suggested that the different distributions are a function of the width of the fault generation zone relative to the longest faults: where the generation zone is relatively narrow (midocean ridges) and only a small percentage of population are active for short periods of time, the generation of spatial correlations (due to long and short-range elastic interaction) that give rise to power-law distributions is strongly suppressed (Cowie *et al.*, 1995).

We suggest that the different types of size distributions found in the this model hinge on mechanical layer thickness, following an evolutionary model of fault systems based on field data presented by Ackermann and Schlische (1997). In their model, when the largest faults exceed the mechanical layer they continue to grow in length but not significantly in displacement, and displacement profiles change from bell-shaped to flat-topped (see Dawers et al., 1993). The dimensions of stress-reduction shadows around the faults (which reflect the long-range elastic interaction of structures) will be restricted because they scale linearly with displacement (Ackermann and Schlische, 1997). Increased rates of along-strike propagation may lead to an increase in lateral fault linkage, such that the end result of that model is a series of large faults with a quasi-regular spacing - similar to mode I fractures and oceanic faults, both of which follow exponential size distributions. The spacing would be a function of mechanical layer thickness (similar to mode I fractures). Cladouhos and Marrett (1996) noted that long faults may not be able to grow at a rate fast enough to maintain power-law scaling; this may be because they can no longer grow in the dip direction, thus retarding lengthening. Nicol et al. (1996) noted that non-power law scaling may indicate that different processes or controls are effective at different scales.

Time 8 marks the point in the strain history of the model when some critical proportion of the faults in the model exceeds the mechanical layer:

$$(h)\cos(90\text{-}\delta) > t_m$$

(where h is fault ellipse height, δ is fault dip, and t_m is thickness of the mechanical layer, in this case the clay layer), and begin to have high ellipticities, such that they shift from having an occupation dimension (f) of 3 to $f = 2$ (see Marrett and Allmendinger (1991) and Ackermann and Schlische (1997) for a complete treatment of this concept). Because faults grow in length with increasing displacement, and less displacement can accumulate when the mechanical layer is exceeded, the average fault length becomes fairly constant after time 8. The change in the trend of the number of faults that grew (normalized) through time (Figure 4.15) occurs at time 9. This likely signifies that there are relatively fewer and fewer active faults as strain increases, which has one of two implications. Either there is preferential partitioning of slip onto larger structures, or the structures that are active are growing faster and faster; the deviance of the cumulative frequency distribution at large fault sizes ("oversized" faults) late in the model run (Figure 4.17) is consistent with the former. The standard deviation of the average fault spacing (Figure 4.16) increases at first as faults form at long range from the central fault zone, but then decreases steadily after time 10 as the faults come closer to having a quasi-regular spacing. Note that time 10 is two time steps after time 8, when the type of size distribution changes, and when the map pattern begins to fill in with faults (Figure 4.7). Time 10 also marks the onset of a decrease in the exponential exponent (λ) as the surface of the model is more heavily effected by the event at time 8. That is, faults that were hidden inside the model at time 8 began to appear at the surface at time 10.

The major change in the fault system is taking place inside the model at time 8 (the change is borne out in the fault statistics at time 8), and there is a time lag until time 10 when it becomes evident in the map pattern and λ. The fault system itself responds to the major change around time 9 by reducing the number of active faults.

Fault generation zone width vs. mechanical layer thickness

At this point in the discussion we have not yet ruled out the width of the fault generation zone as a factor in the shift from a power-law to an exponential distribution: it may be that at $\overline{L} \approx 1.65$ cm (time 8), the width of the fault generation zone was narrow enough relative to the largest faults to produce an exponential size distribution. If this is the case, then a model with a narrower generation zone should exhibit the power-law-exponential shift at *lower* values of $\overline{L}$ and/or *sooner* (in terms of strain) after the first appearance of faults at the model surface. Model 02.02.96 was similar in the setup to the model discussed here (12.15.96), with the exception of a 25% *narrower* discontinuity (9 cm) and a 200% *thicker* clay layer (3.9 cm).

Figure 4.22 presents length and exponent data through time for 02.02.96. Difficulties with image acquisition during the model run have introduced scatter to most of the data collected for the model. The average length curve for 02.02.96 (Figure 4.22) has the same general form as the curve for 12.15.96 (Figure 4.18), with the levelling off occurring at time 12. A similar power-law exponential shift occurs at time 12, which is later than in 12.15.96 (~22.4% vs. ~13% extension), as well as later after the first appearance of faults (~14% vs. ~6.6%, with delays of 8.4 and 7.6 percentage points, respectively). Furthermore, the shift occurs at a greater value of $\overline{L}$ (2.27 cm) in 02.02.96 than in 12.15.96 (1.65 cm). These observations not only eliminate the width of the fault generation zone as the factor governing the shift from power-law to exponential distribution, but point to mechanical layer thickness as the determining factor.

This hypothesis is consistent with a progressive increase in width of the generation zone from oceanic crust to continental crust with high heat flow to continental crust with low heat flow. Thickness of the uppermost brittle crustal layer also increases along this progression, and size distributions appear to shift from exponential to power-law along the same trend. Hence, there appears to be a broad correlation between mechanical layer thickness and width of the fault generation zone: thinner layers are exceeded sooner and thus long-range interactions do not take place, leading to exponential distributions due to the suppression of spatial correlations.

$\overline{L}$ vs. $\langle L \rangle$

$\overline{L}$ (average fault length) is consistently lower than $\langle L \rangle$ (characteristic length). This is because the structural level of observation is the model surface, and faults are propagating upward from the interface between the latex sheet and the clay. Thus, at any given time step, there are small faults that have not yet cut the surface and have not been sampled, which in turn leads to $\overline{L}$ overestimating the average length. $\overline{L}$ appears to be converging with $\langle L \rangle$ after time 10 (recall that at time 10, the major change in the system becomes apparent at the model surface), suggesting that, with increasing strain, $\overline{L}$ becomes a better measure of average fault length until the end stage of the Ackermann and Schlische (1997) model, when $\overline{L} \approx \langle L \rangle$. The same general trends can also be seen in model 02.02.96.

Spatial distribution of fault centroids

It was noted above that the results of the different spatial analysis techniques conflict. The χ^2 based analyses indicated a uniform, non-random, non-clustered spatial distribution of points through time. Recall that uniformity in a point distribution implies a *lack* of independence of points with each other. The scanline-based cluster analyses yielded a random distribution of points in the dip direction through time (ψ'). The distribution of points in the strike direction (ψ) was found to exhibit self-similar spatial clustering until time 10, when it changed to a random distribution (coincident with a major change in the map pattern, spacings, and λ). Cowie et al. (1995) suggested that short- and short and long range elastic interactions between faults results in populations with strong spatial correlations that follow power-law size distributions. Recall that a random distribution of points implies *independence* of points from each other. If this is the case, then it would be impossible to have a population of faults that are randomly distributed but follow a power-law distribution of sizes as discussed in Dawers and Malinverno (1997). We suggest that the condition of $\psi \approx 1$ is one of a uniform point distribution, not random.

If fault systems evolve as outlined in Ackermann and Schlische (1997), they start off able to interact with each other at long range, and thus follow a power-law distribution of fault sizes, and produce a condition of $0 < \psi < 1$ (self-similar spatial clustering). When the shift from power-law to exponential distribution occurs, the large-scale distribution of structures is already determined, such that the distribution of structures shifts from self-similar spatial clustering to uniform, because now faults cannot interact at long range. The distribution is not random because the faults were not independent of each other when the overall fault pattern formed. In addition, faults can still interact over short ranges such that new faults are not independent of old ones. This may lead to the condition of power-law scaling over small areas (individual large fault blocks that are relatively elastically independent from each other, similar in concept to the individual rafted packages of faults in midocean ridge settings described by Cowie *et al.*, 1995). The sequence of events is consistent with the change in ψ through time in the model: at first there is self-similar spatial clustering, then at time 10 the spatial distribution becomes uniform (erroneously termed "random" in Dawers and Malinverno, 1997). Recall that at time 10 (e.g. Figure 4.16), the map pattern catches up to the major change in the model that occurred at time 8, namely the shift from power-law to exponential distribution. It appears that the scanline based cluster analysis (when performed in two sampling directions) is more sensitive to self-similar spatial clustering than the grid-based χ^2 tests for uniformity and randomness.

Modeling artifacts

As with any scaled physical model, the results and interpretations must be critically examined in light of the limitations of the experimental setup. Modeling media, dimensions, and strain rate were selected so as to maintain geometric, kinematic, and dynamic scaling relations based on the experience of the experimental physical modeling group at Mobil. One potential artifact may be produced by the modeling apparatus itself. The modeling area is only 60 cm in the strike direction - thus faults cannot grow any longer. We feel that this is not a factor in this study, specifically because at the shift from power-law to exponential distribution (time 8) there were no faults (even soft-linked) nearly this long. The width of the discontinuity (12 cm prior to deformation) may be producing an artifact in the form of the ~4 cm inflection in the r' curves, although it is not clear if this is actually the case.

The origins of the long graben systems at the top and bottom of the model are not clear. The grabens at the top of the model formed early in model run (times 6 -7), whereas the graben near the bottom of the model formed late (time 14). Their locations coincide with the edges of the latex discontinuity and with the position of the retracting overlapping metal plate (top grabens only), and they are most likely edge effects. There are three possible explanations for their formation: 1. The retracting overlapping metal plate left a void behind it, causing the overlying material to collapse into it. 2. The latex discontinuity was sticking to the base of the modelling apparatus. 3. There was a heterogeneity in the model due to the latex-duct tape interface. In order to determine if the edge effect grabens had significant influence on the population systematics of the model, specifically if they were the cause of the change from a power-law to an exponential size distribution (Figures 4.17, 4.23a) , they were removed from the cumulative frequency analysis of fault lengths (Figure 4.23b). The quality of the curves is degraded by the parsing, although the degree of degradation decreases with time. The change from a power-law to exponential distribution of fault sizes is still present, although at time 8 the distribution of faults sizes could be either power-law or exponential. The results of the analysis suggests that even though the graben systems were the results of edge effects, they should not be removed from the analysis because they are part of a coherent fault system with elastically interacting faults. Future work will be directed towards producing models without these edge effects, most likely by using *silbion* putty rather than latex as the basal discontinuity.

Another issue to consider is the influence of the edge-effect from the model walls on the fault statistics. We specifically selected the study area outlined in Figures 4.2 - 4.11 in order to minimize edge-effects. Faults near the outer edges of the study area appeared first within the study area, and propagated laterally, parts of them extending out of the study area and becoming part of the edge-effect. Finally, our modeling material was homogeneous throughout the model, with no preexisting fabrics, weaknesses, or random flaws. Real rocks usually have at least two of these characteristics. It is not clear if extremely small scale heterogeneities in the wet clay scale up to the random flaws in rocks.

SUMMARY AND CONCLUSIONS

1. The map pattern of the model evolves gradually through time, passing through a period of a weakly right-stepping fault fabric. Three through-going full graben systems form, with the regions between them filled in with smaller structures. Most of the brittle deformation is concentrated in the central 8 cm of the model (measured in the dip direction).

2. Examination of the population systematics of this model reveals that there is a major change in the scaling relations of the fault population at time 8, most notably a shift from a power-law distribution of fault sizes to exponential distribution. This shift is coincident with a major linkage event, and a leveling-off in the trend of average fault length ($\overline{L}$).

3. The shift becomes evident in the map pattern of the model after a lag of two time steps (time 10), with a reversal in the trend of the standard deviation of the average fault spacing indicating that the faults are becoming more regularly spaced.

4. The characteristic fault length (<*L*>) derived from the exponential distribution of fault sizes is consistently less than $\overline{L}$ (average observed fault length) due to the sampling level. The values of <*L*> and $\overline{L}$ appear to converge with increasing strain, suggesting that with increasing strain, $\overline{L}$ becomes a more accurate measure of the true average fault length.

5. Analysis of the spatial distribution of structures using two different techniques yielded what appear to be conflicting results. The bi-directional grid-based χ^2 tests for uniformity and randomness suggest a uniform, non-random, non-clustered distribution through time. The one-directional scanline based ψ & ψ' analyses indicated a "random" distribution (more properly termed uniform) in the dip direction through time, and a shift from self-similar spatial clustering to a "random" distribution at time 10.

6. These observations are consistent with the field observations and an evolutionary model presented in Ackermann and Schlische (1997). Early in the strain history of a system, faults are able to interact elastically at short and long ranges, which gives rise to a population of faults with strong spatial correlations and a power-law distribution of fault sizes. Eventually faults begin to exceed the mechanical layer, and begin to have higher aspect ratios as they continue to grow along strike but not in the dip direction. This in turn restricts the size of the stress-reduction shadows and deformation around the faults, which are generally the means by which faults elastically interact at long range. Spatial correlations begin to be suppressed, a quasi-regular fault spacing arises, and the distribution of fault sizes becomes exponential, similar to mode I cracks and oceanic faults where the mechanical layer has been exceeded. The spatial distribution becomes uniform, not random, reflecting the original spatially correlated fault pattern.

7. Thickness of the faulted mechanical layer is the controlling factor in how fault sizes are distributed and spatially correlated. Hence oceanic populations follow exponential scaling and lack spatial correlation because they are bounded, whereas continental systems are usually unbounded and follow power-law scaling with strong spatial correlations. Systems in thinner mechanical layers will reach the transition from power-law to exponential distribution and the transition from spatial clustering to a uniform distribution earlier (at lower strains) than those in thicker layers. Given enough strain, all fault systems might eventually experience these transitions. We suggest that the natural fault system in Ackermann and Schlische (1997) represents a transitional phase (mid-shift).

8. Time-series analysis of the population systematics of scaled physical models is a viable means by which to learn more about how fault systems evolve.

9. Future work will include using *silbion* putty for the basal discontinuity, as well as examining the role of mechanical layer thickness and fault generation zone width by varying these two components of the model design.

Image number	Time (H:MM)	Heave (cm)	% Extension	$\overline{L}$	C	λ	$<L>$	ψ	ψ'
5	1:06	1.10	9.167	0.50	1.412	-	-	0.638	1.157
6	1:15	1.25	10.417	0.83	0.947	-	-	0.795	1.069
7	1:24	1.40	11.667	1.21	0.694	-	-	0.727	0.922
8	1:33	1.55	12.917	1.65	-	1.054	0.948	0.754	1.026
9	1:42	1.70	14.167	1.76	-	1.043	0.959	0.717	0.995
10	1:51	1.86	15.508	1.74	-	1.078	0.928	0.911	1.037
11	2:00	2.00	16.667	1.68	-	0.946	1.057	1.001	1.12
12	2:09	2.15	17.917	1.70	-	0.888	1.127	1.06	1.079
13	2:18	2.30	19.300	1.97	-	0.723	1.384	0.937	1.002
14	2:27	2.45	20.433	1.97	-	0.653	1.532	0.884	0.949

Table 4.1: Summary of time slices discussed in this paper.

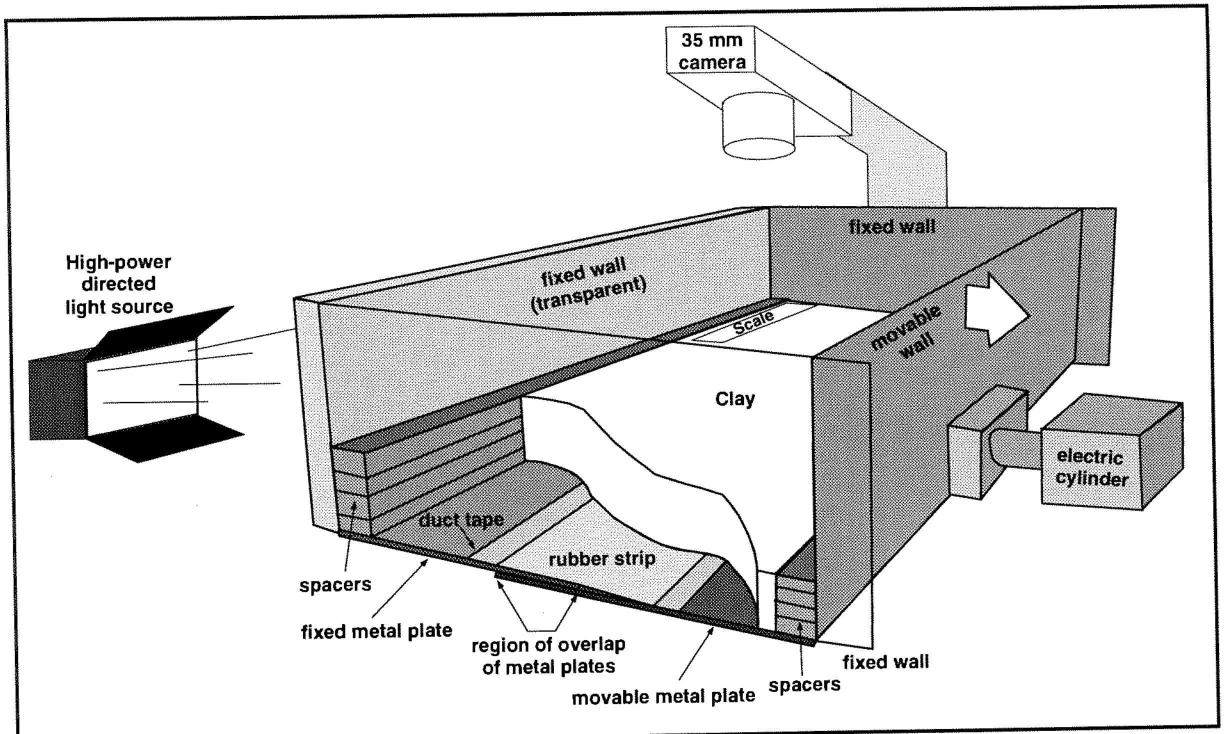

Figure 4.1: Modeling Apparatus at the MEPTEC DRL structure lab. Modified from Eisenstadt et al. (1995)

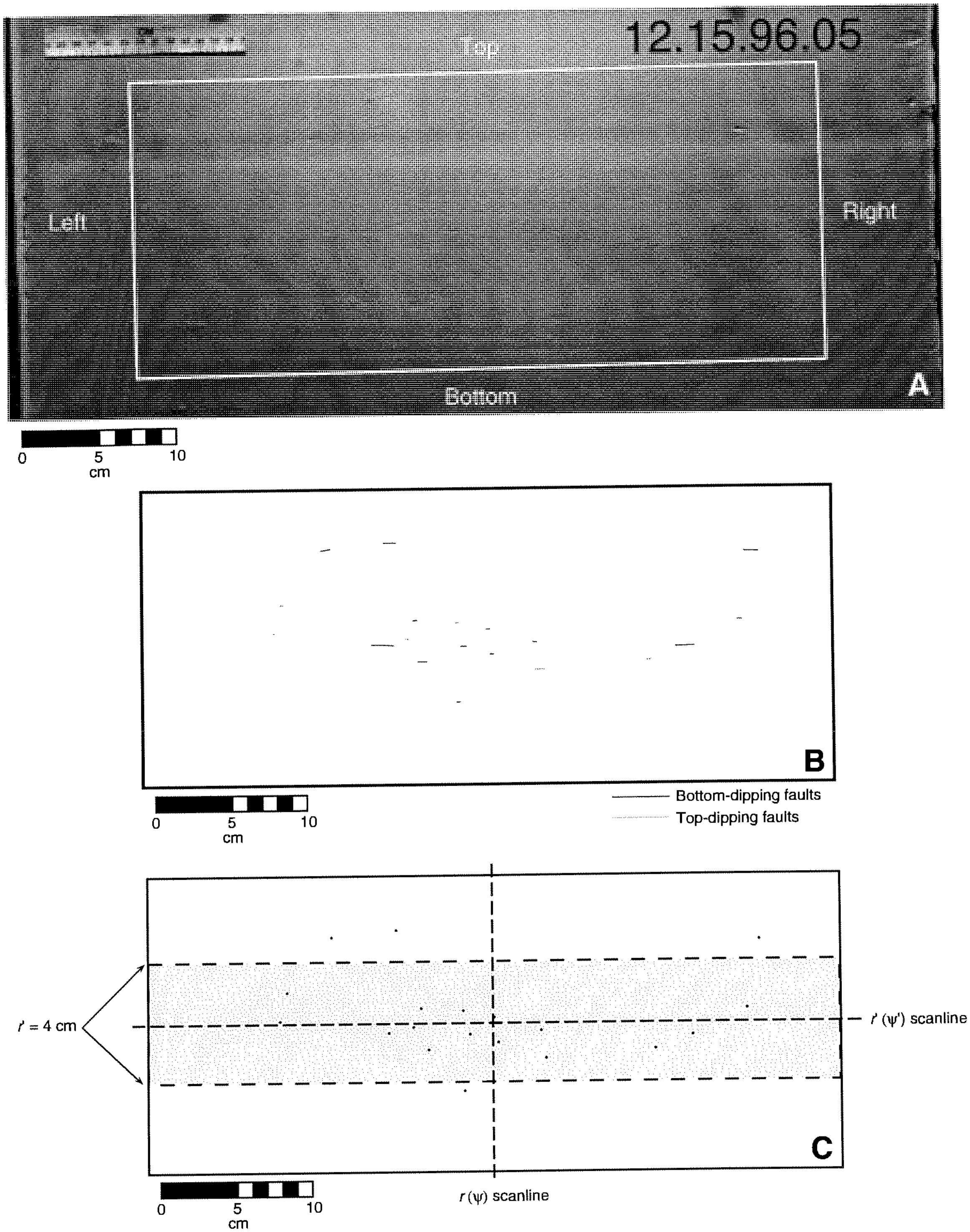

Figure 4.2: Time 5. A is the image of the model surface; the study area is outlined with the white box. B is the fault map derived from the image in A, C is the centroid map derived from B.

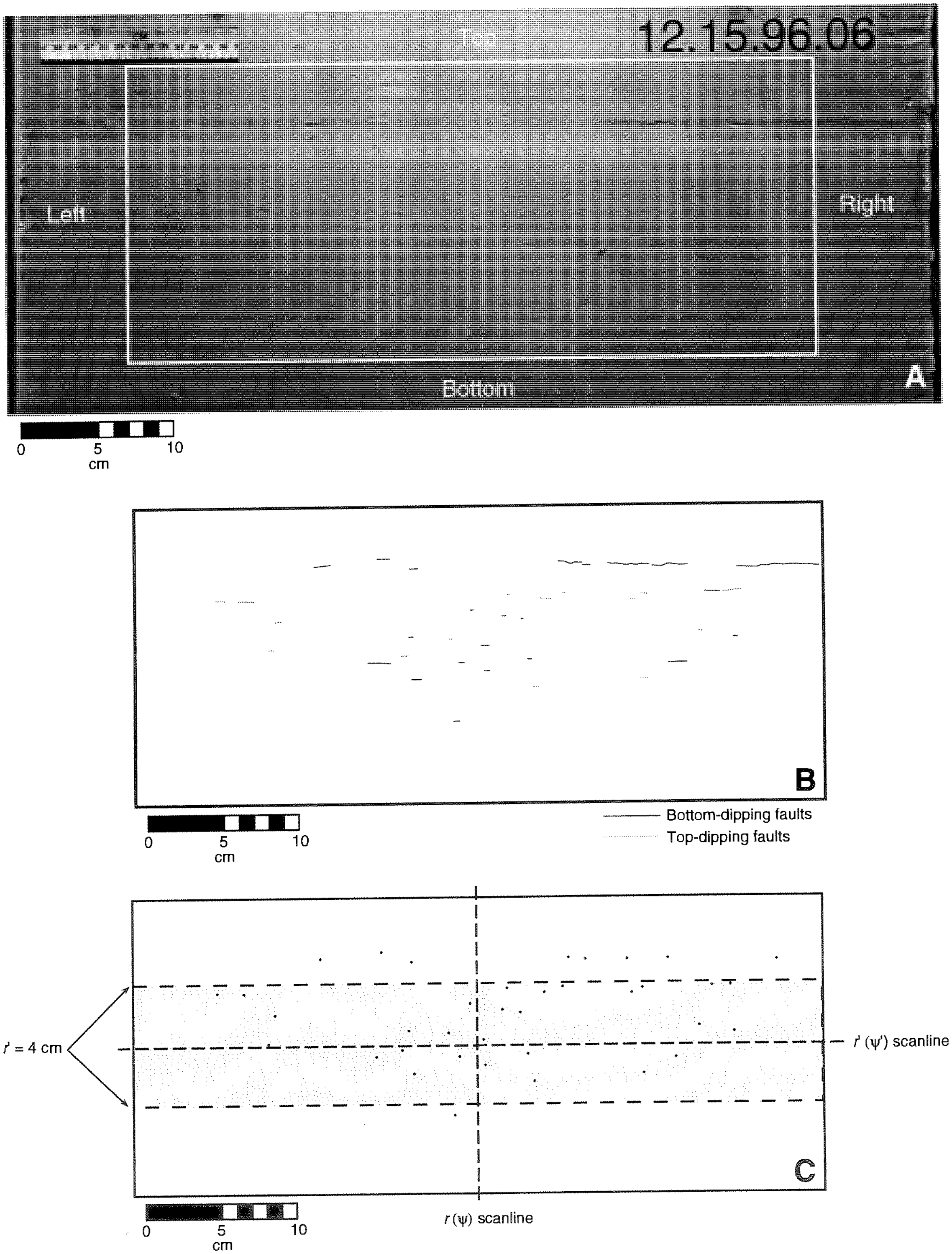

Figure 4.3: Time 6. A is the image of the model surface; the study area is outlined with the white box. B is the fault map derived from the image in A, C is the centroid map derived from B.

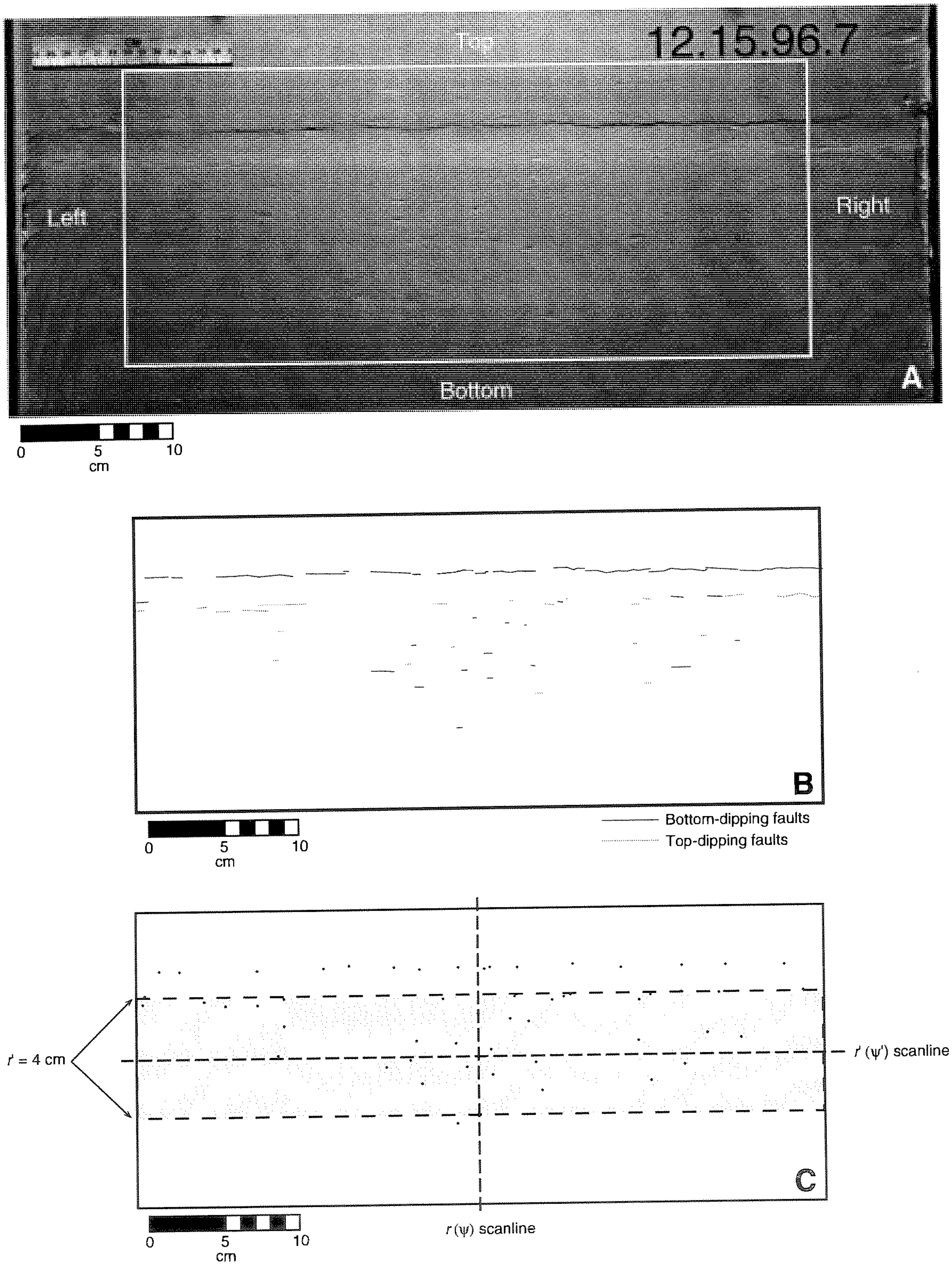

Figure 4.4: Time 7. A is the image of the model surface; the study area is outlined with the white box. B is the fault map derived from the image in A, C is the centroid map derived from B.

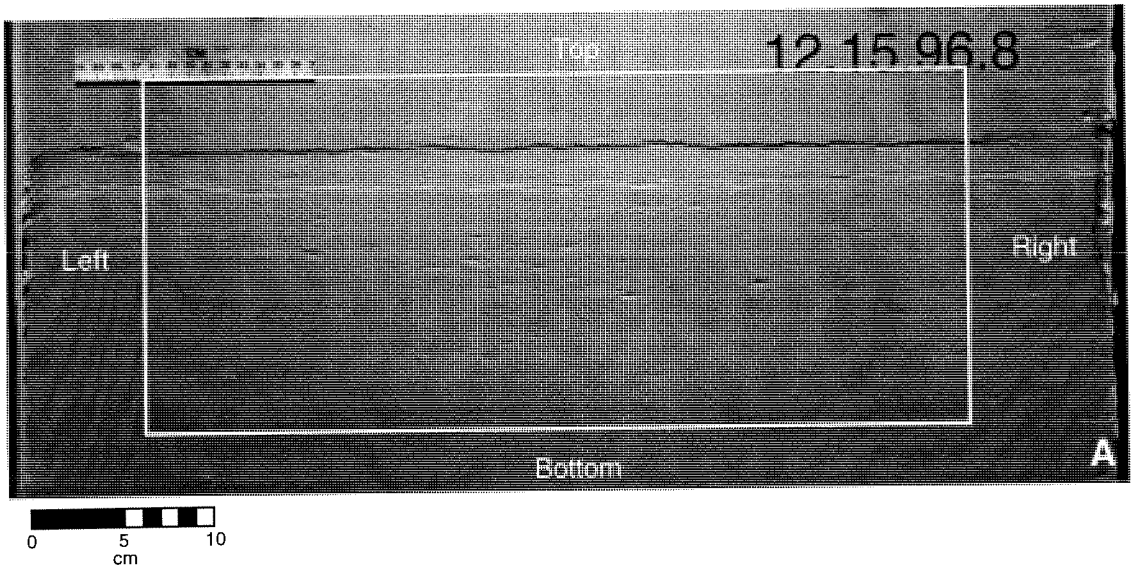

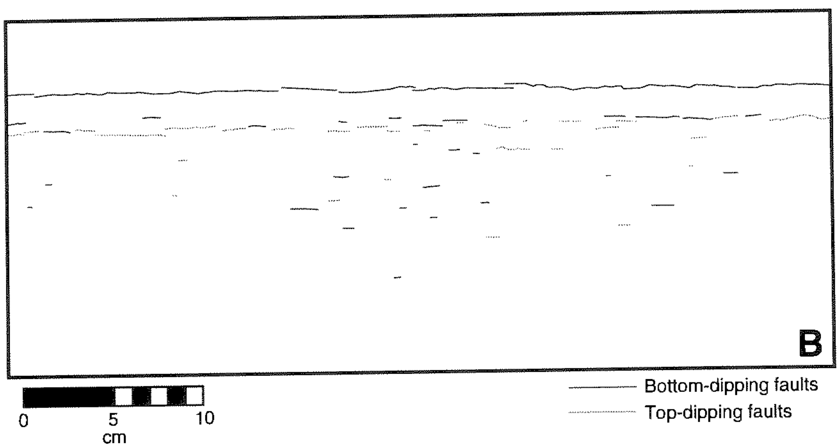

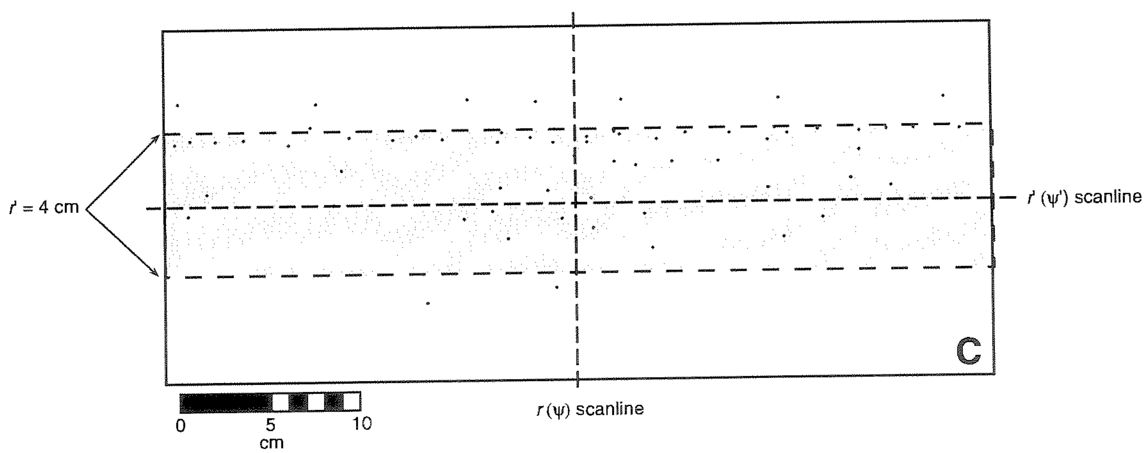

Figure 4.5: Time 8. A is the image of the model surface; the study area is outlined with the white box. B is the fault map derived from the image in A, C is the centroid map derived from B.

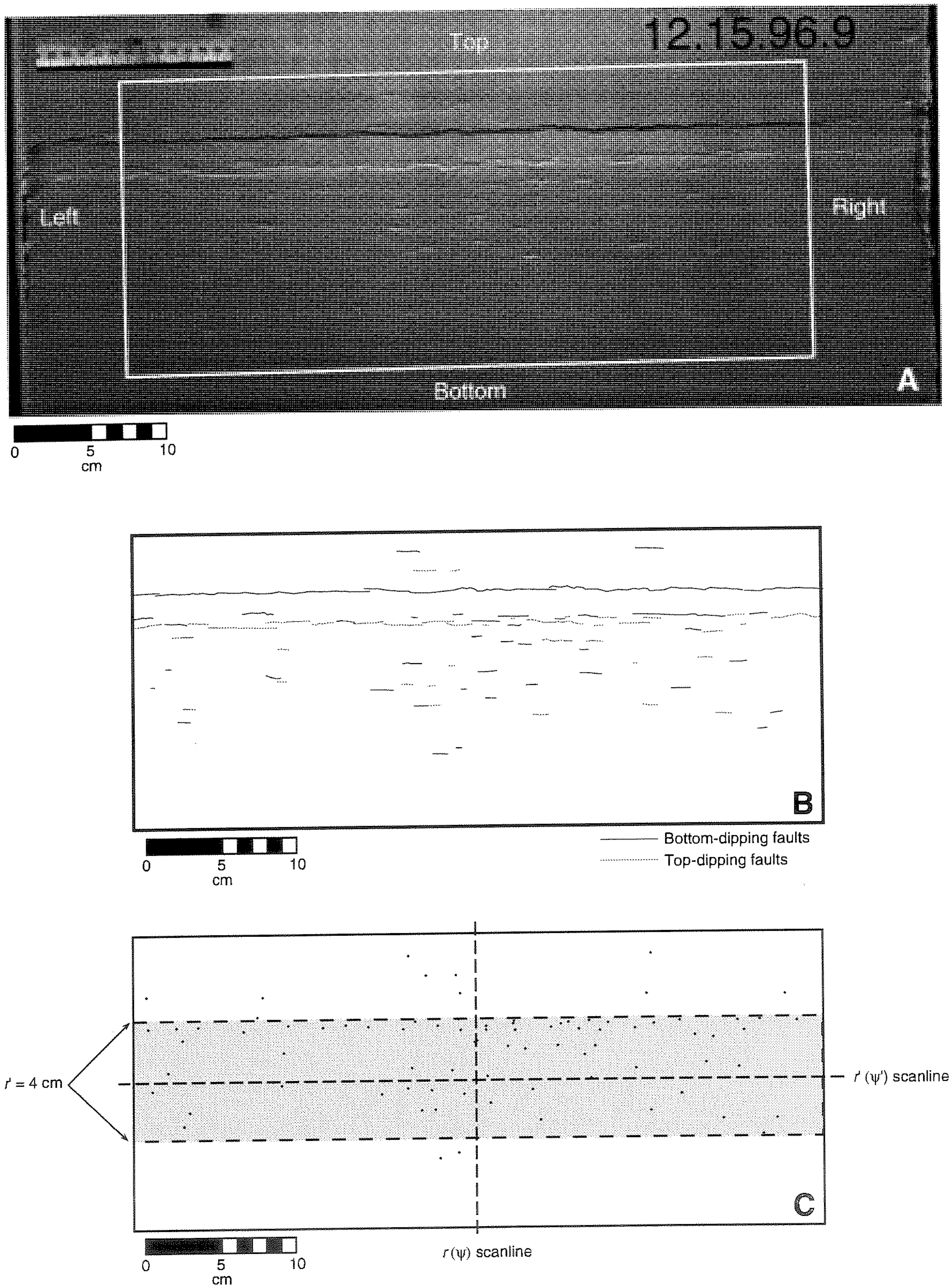

Figure 4.6: Time 9. A is the image of the model surface; the study area is outlined with the white box. B is the fault map derived from the image in A, C is the centroid map derived from B.

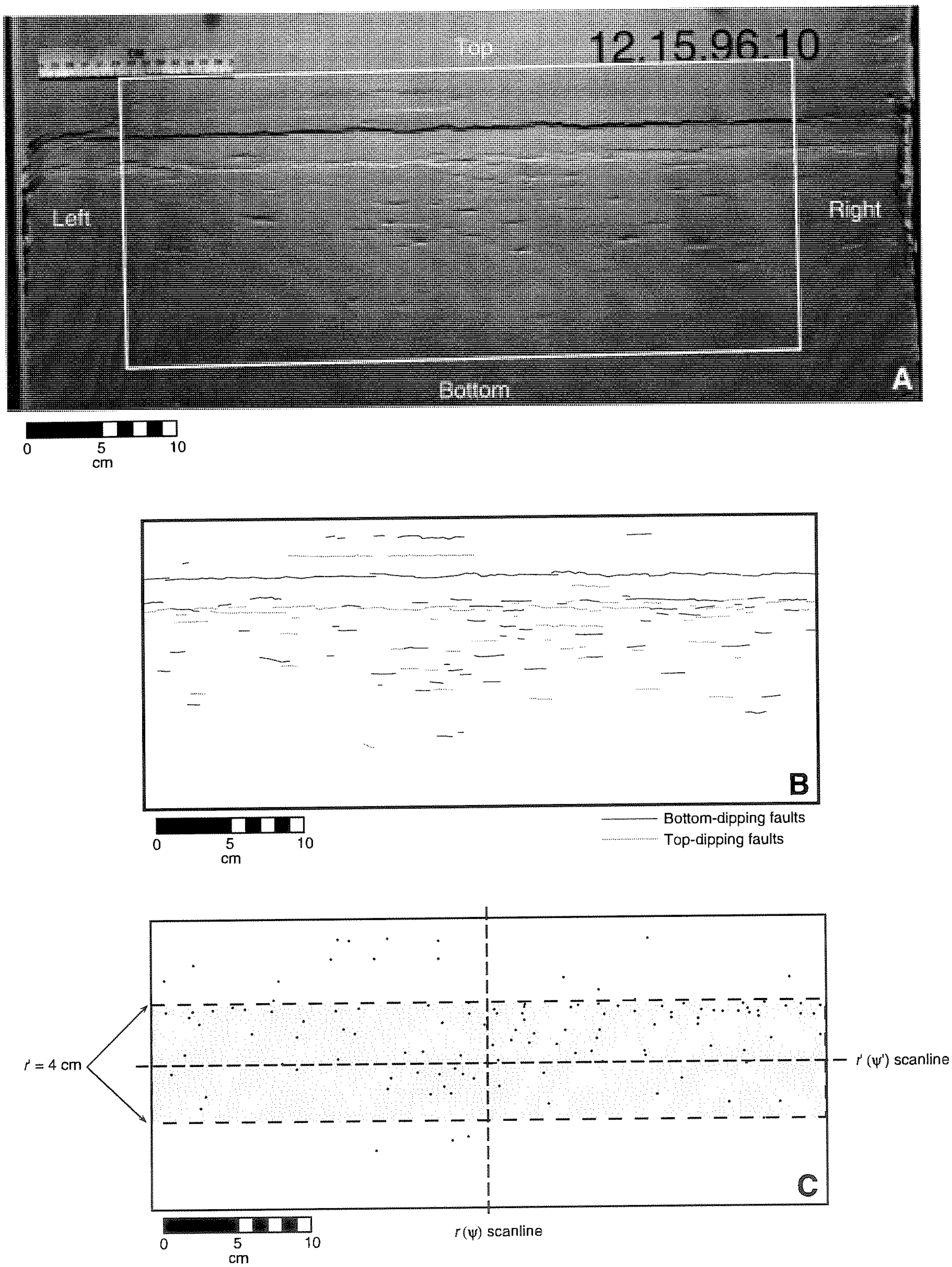

Figure 4.7: Time 10. A is the image of the model surface; the study area is outlined with the white box. B is the fault map derived from the image in A, C is the centroid map derived from B.

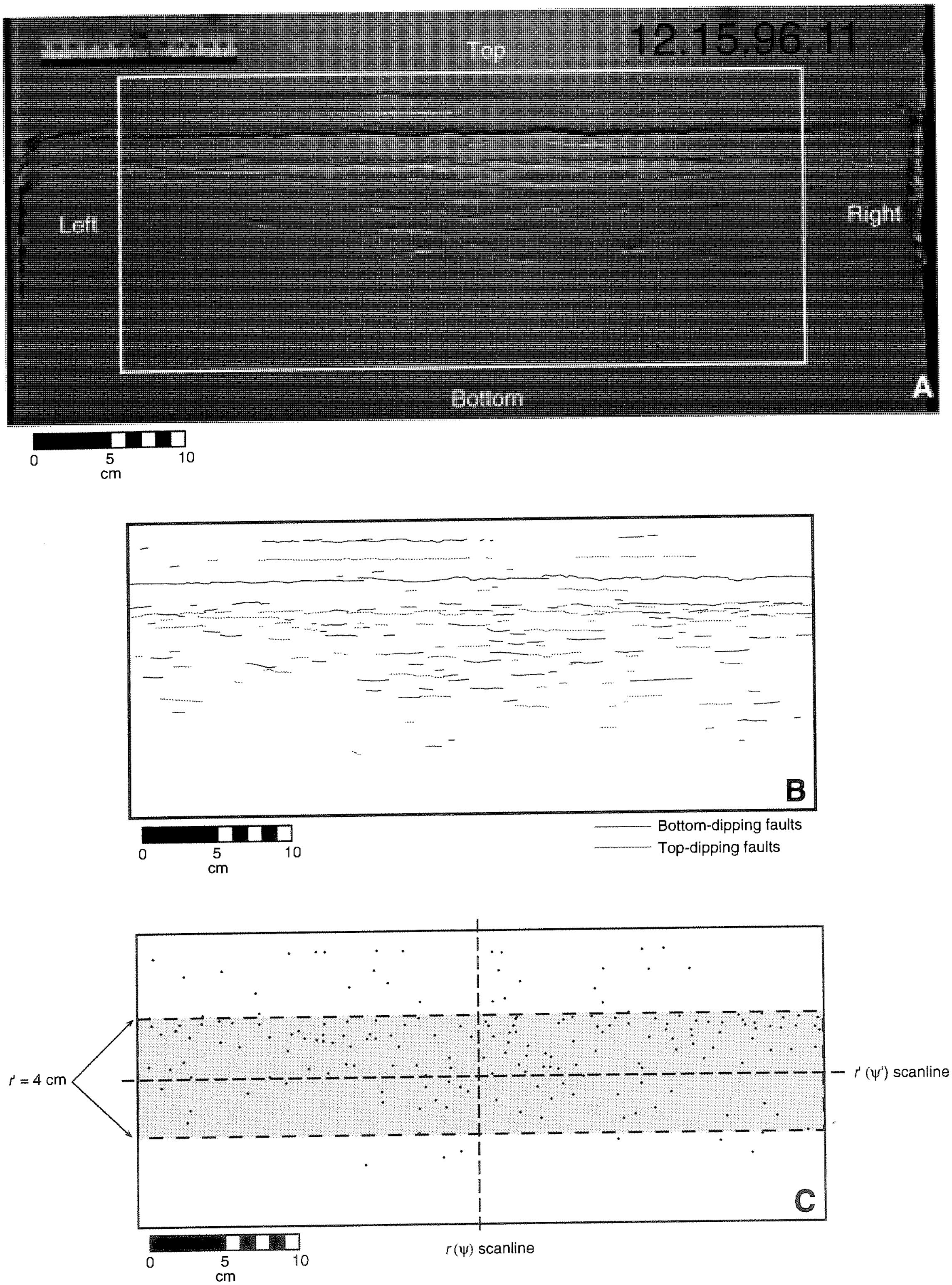

Figure 4.8: Time 11. A is the image of the model surface; the study area is outlined with the white box. B is the fault map derived from the image in A, C is the centroid map derived from B.

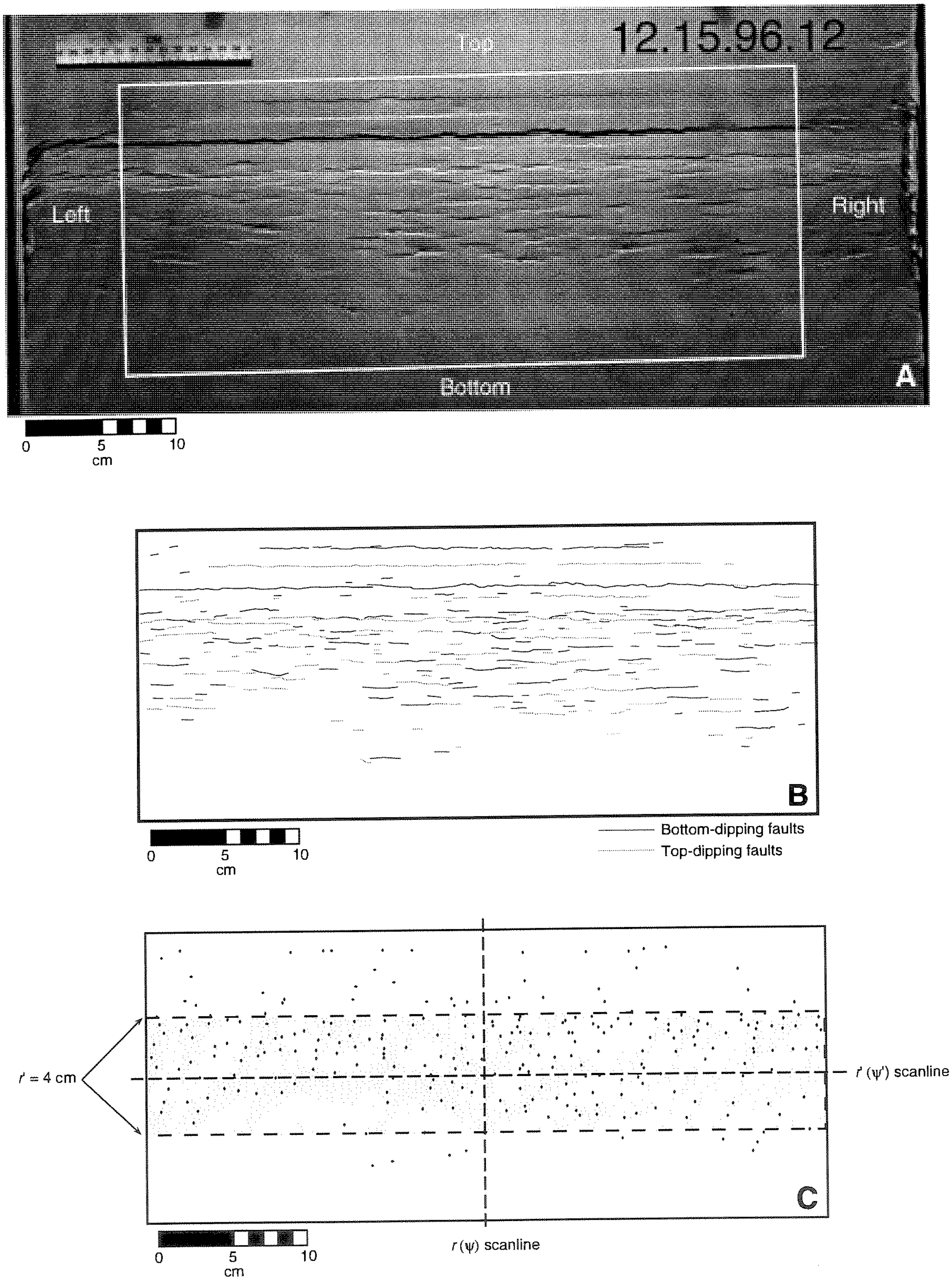

Figure 4.9: Time 12. A is the image of the model surface; the study area is outlined with the white box. B is the fault map derived from the image in A, C is the centroid map derived from B.

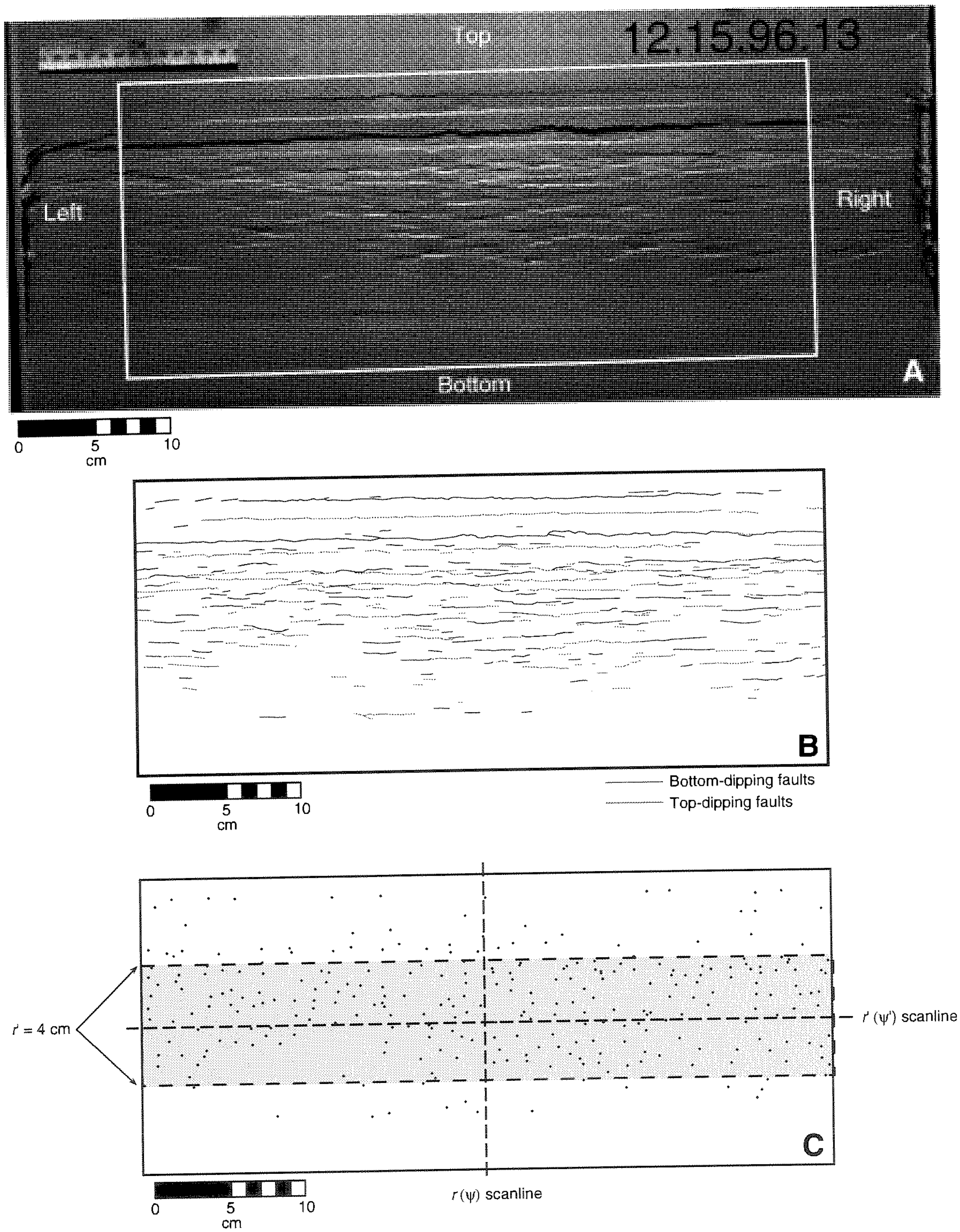

Figure 4.10: Time 13. A is the image of the model surface; the study area is outlined with the white box. B is the fault map derived from the image in A, C is the centroid map derived from B.

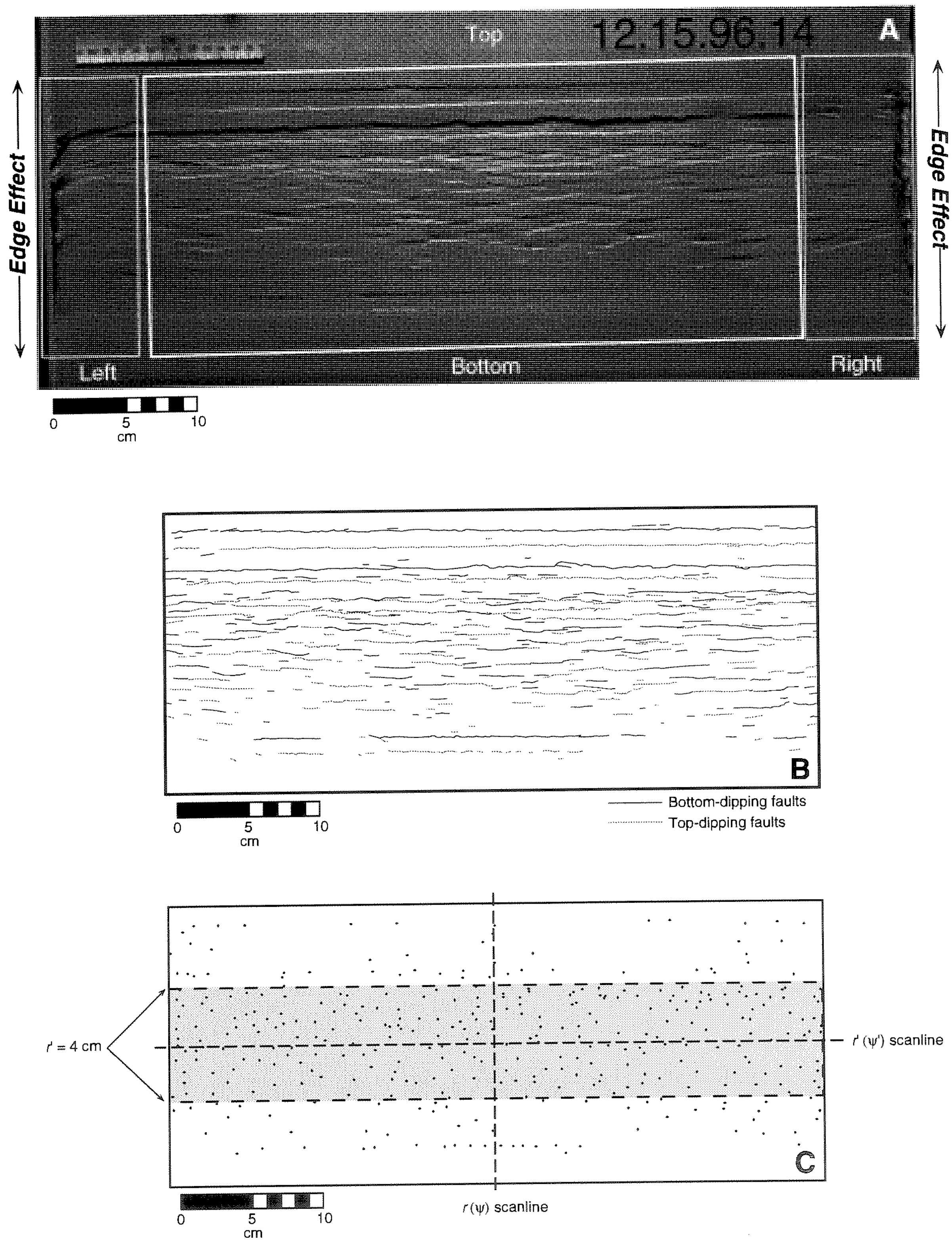

Figure 4.11: Time 14. A is the image of the model surface; the study area is outlined with the white box. B is the fault map derived from the image in A, C is the centroid map derived from B.

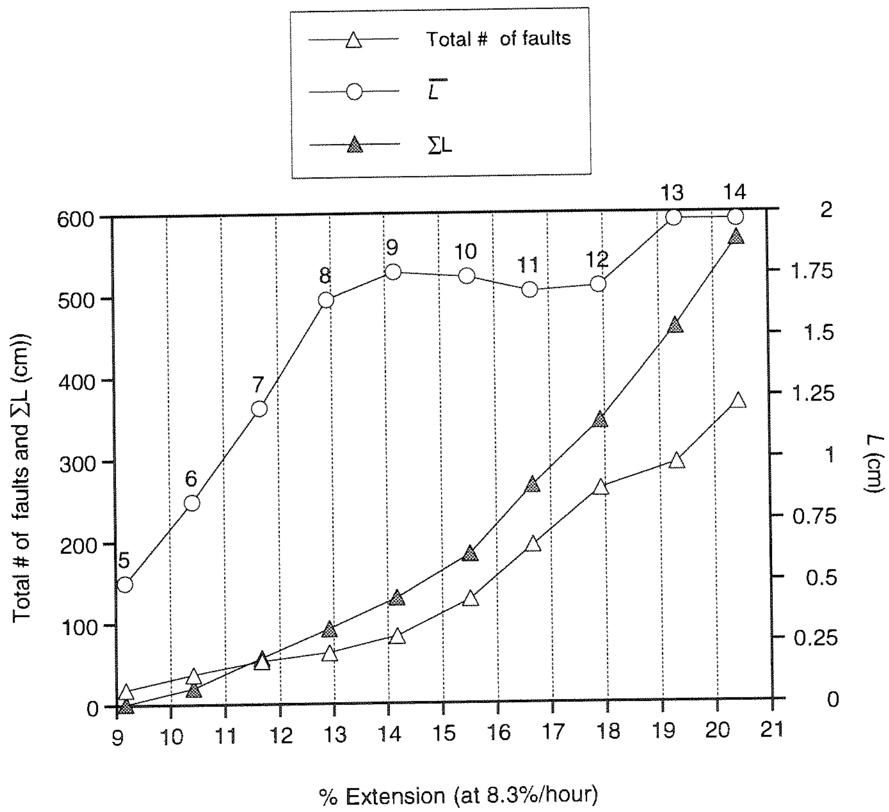

Figure 4.12: Number of faults, average length, and summed length through time (a constant strain rate of 1 cm/hr makes strain a proxy for time). Numbers above symbol are the time step.

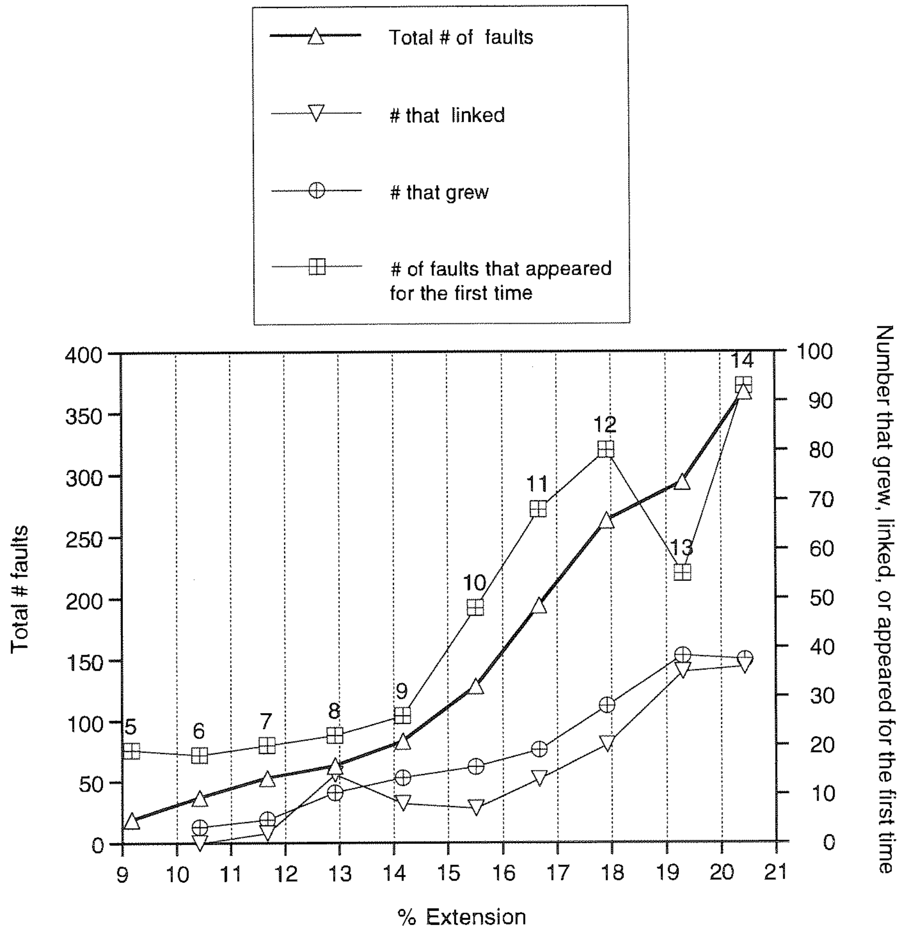

Figure 4.13: Absolute numbers of faults through time, unnormalized. Note that all numbers are increasing.

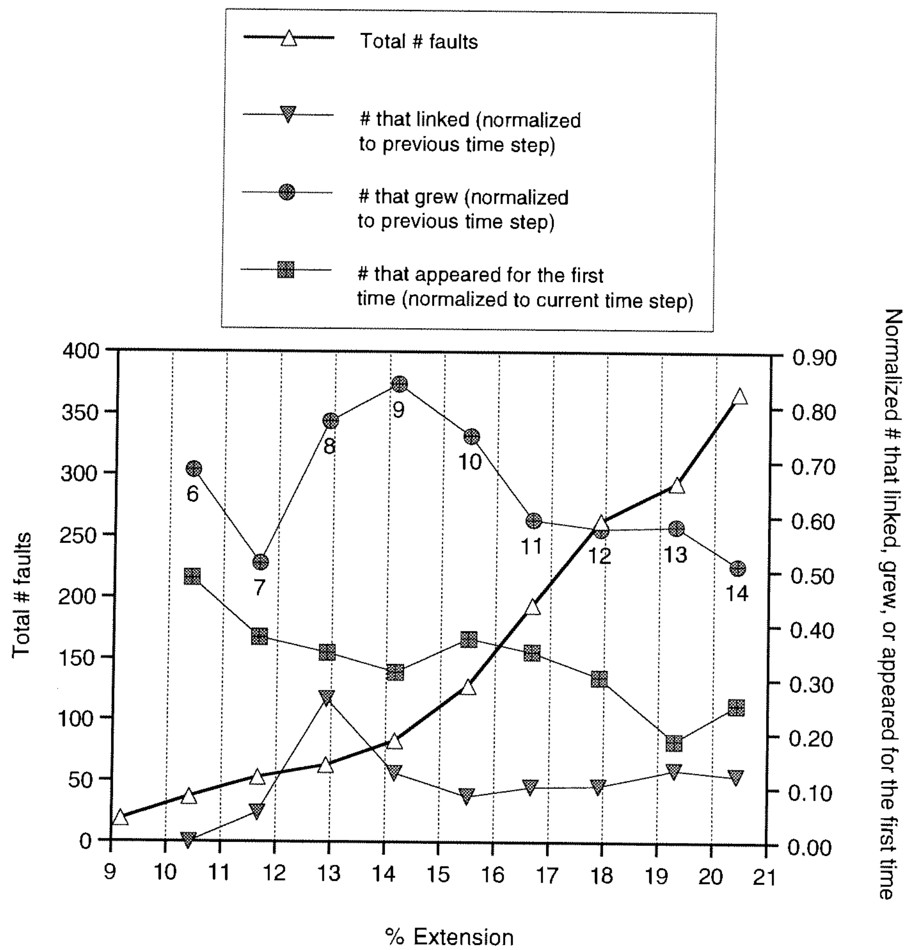

Figure 4.14: Total number of faults, and normalized number of faults that grew, linked, or appeared for the first time. See text for explanation of the normalization.

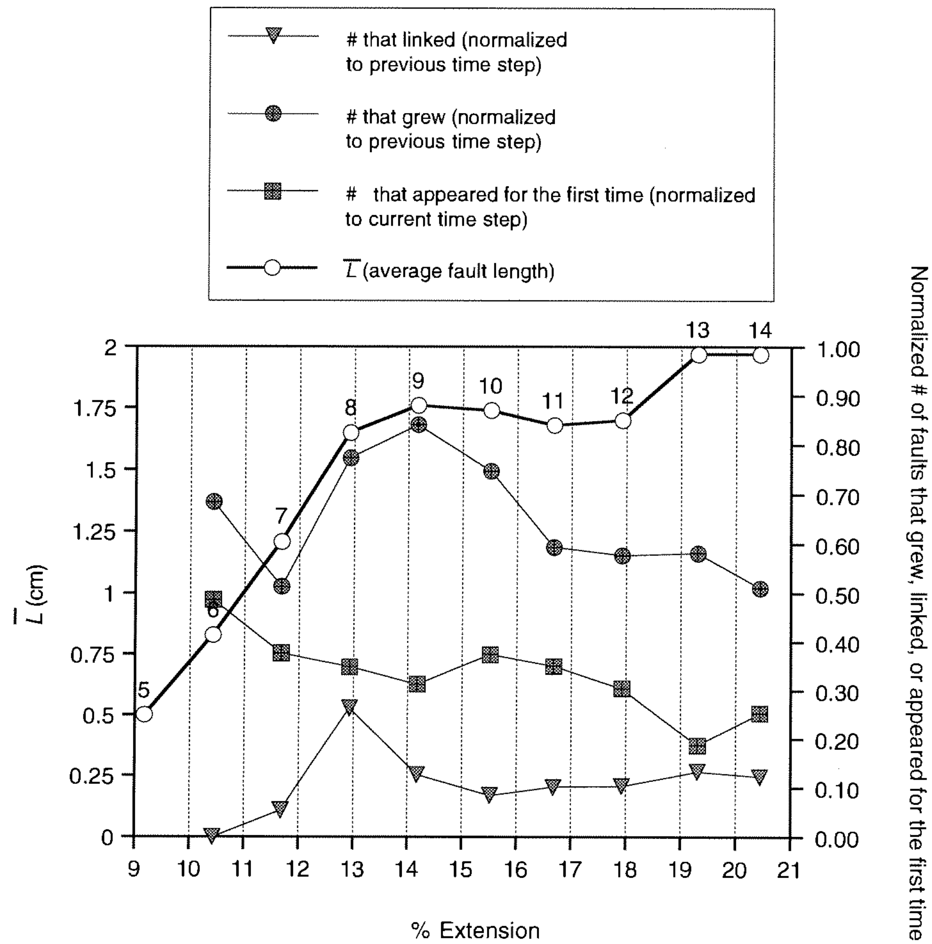

Figure 4.15: Average fault length and normalized numbers of faults through time.

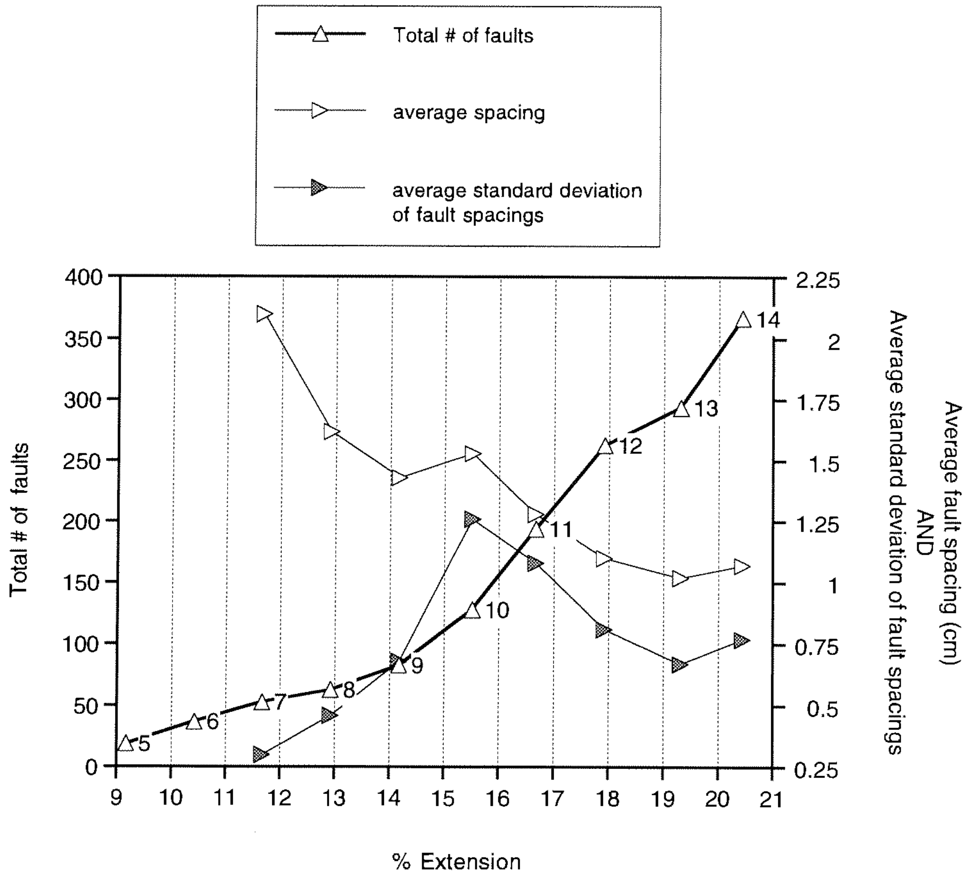

Figure 4.16: Total number of faults and fault spacing data through time.

Figure 4.17: Cumulative frequency diagram of fault lengths through time. All time steps suffer from some form of censoring or truncation. Data used for equation fits are colored black. Note the change in the form of the plots between time steps 7 and 8. Time steps 8 - 14 plot as virtually straight lines in log-linear space, which is consistent only with an exponential distribution.

Power-Law	▷	Time 5	$R^2 = 0.967$	C = 1.412
	◁	Time 6	$R^2 = 0.964$	C = 0.947
	▲	Time 7	$R^2 = 0.994$	C = 0.694
Exponential	✚	Time 8	$R^2 = 0.980$	$\lambda = 1.055$
	✚	Time 9	$R^2 = 0.980$	$\lambda = 1.043$
	▽	Time 10	$R^2 = 0.984$	$\lambda = 1.078$
	◇	Time 11	$R^2 = 0.988$	$\lambda = 0.946$
	△	Time 12	$R^2 = 0.998$	$\lambda = 0.888$
	□	Time 13	$R^2 = 0.990$	$\lambda = 0.723$
	○	Time 14	$R^2 = 0.995$	$\lambda = 0.653$

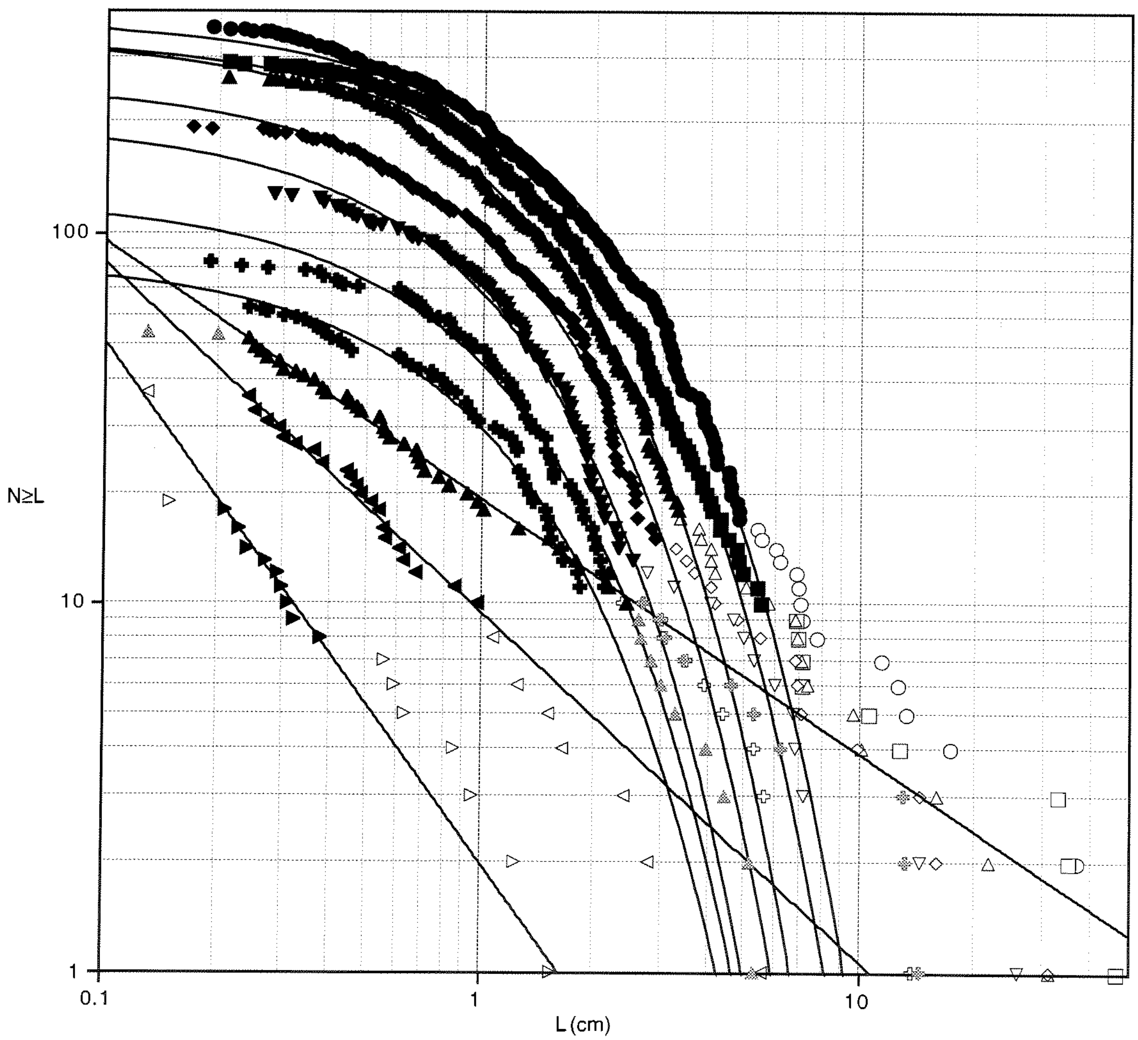

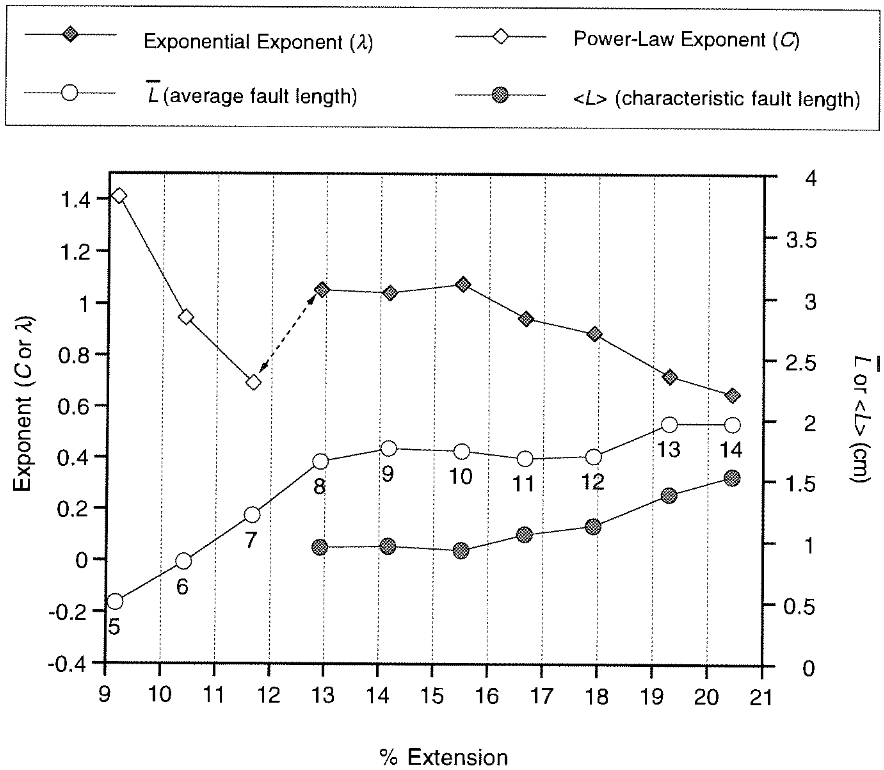

Figure 4.18: Cumulative frequency exponents, average lengths, and characteristic lengths through time. See text for full explanation.

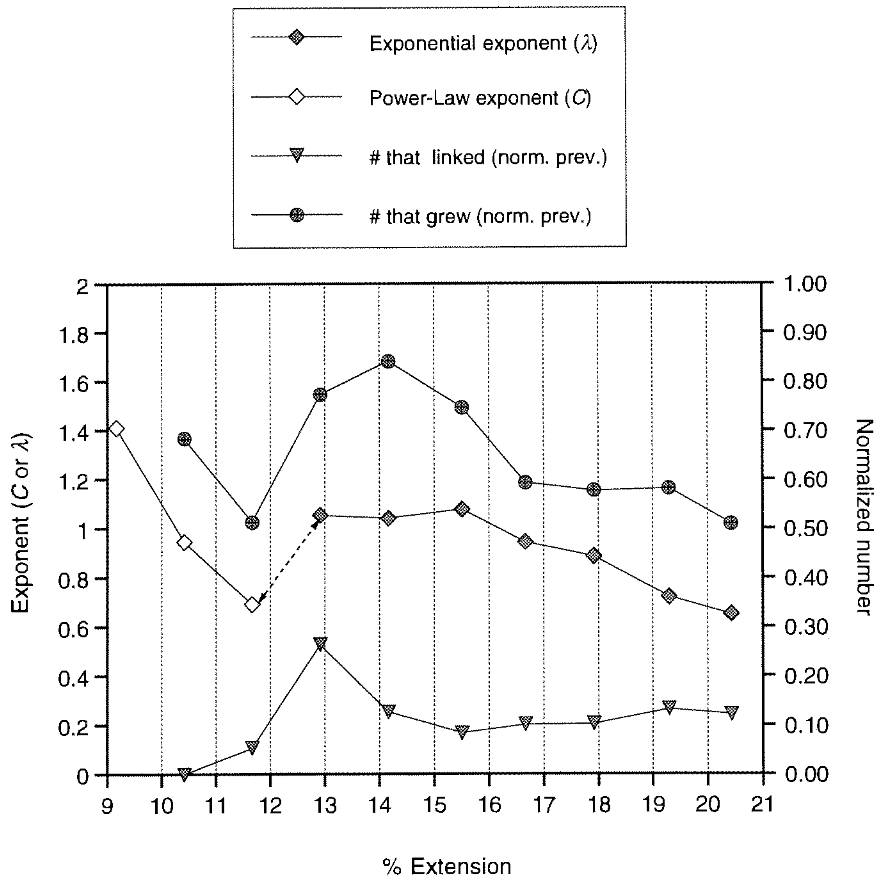

Figure 4.19: Cumulative frequency exponents, and normalized number of faults that linked and grew through time. See text for explaination of normalization.

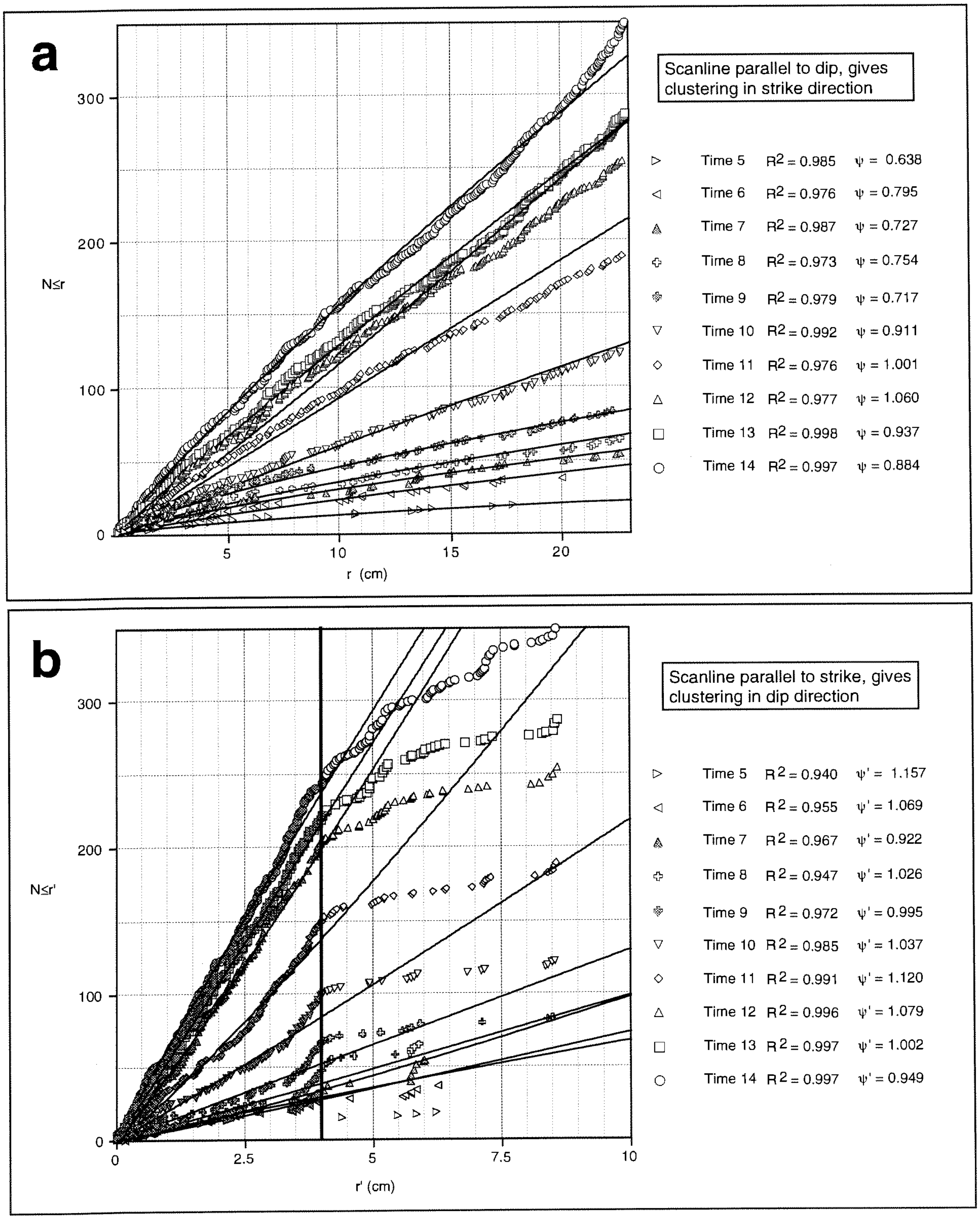

Figure 4.20: Results of scanline-based cluster analysis for scanlines oriented parallel to the extension direction (A, e.g. Dawers and Malinverno, 1997) and parallel to the strike direction (B). All data in (A) were used for curve-fitting. Data used for curve-fitting in (B) are shaded. Note inflection in N≤r' in B at r'≈4 cm. See text for full explanation, Figure 21 for a summary.

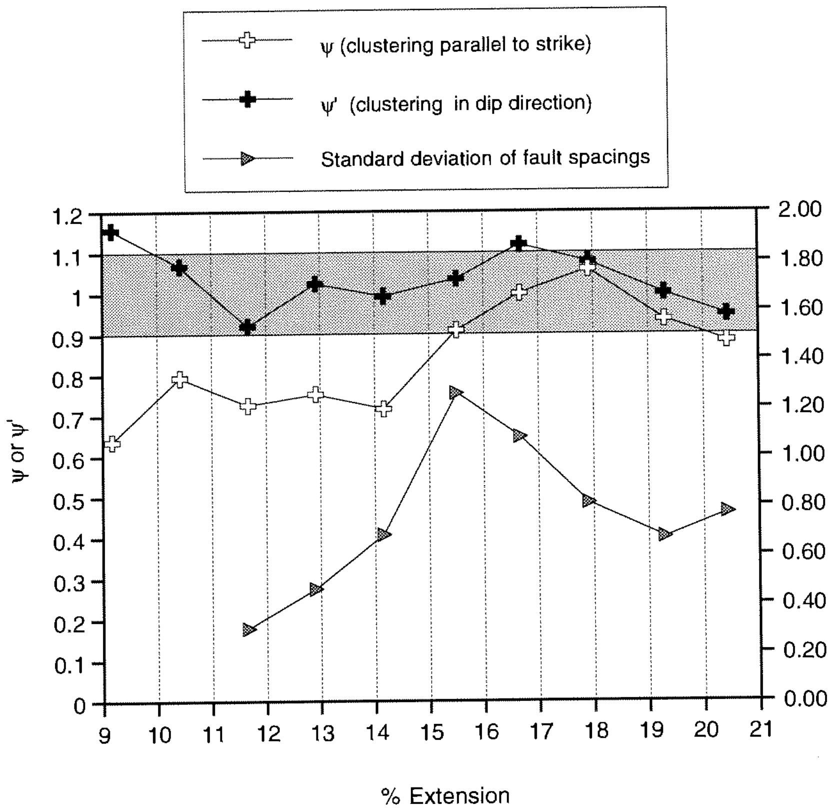

Figure 4.21: Scanline-based clustering dimensions and standard deviation of fault spacings through time. Shaded box represents a range of clustering dimensions interpreted as "random" (uniform) spatial distributions. Note the shift in the standard deviation trend is coincident with ψ entering the shaded region. See text for complete discussion.

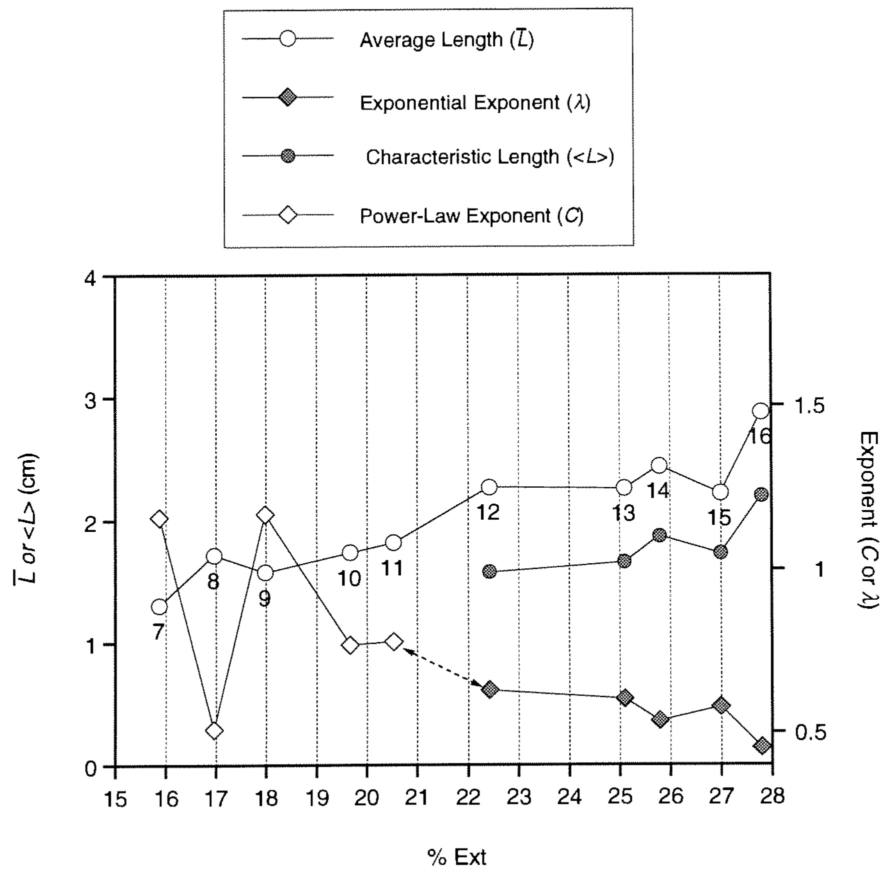

Figure 4.22: Length and exponent data through time for model 02.02.97.

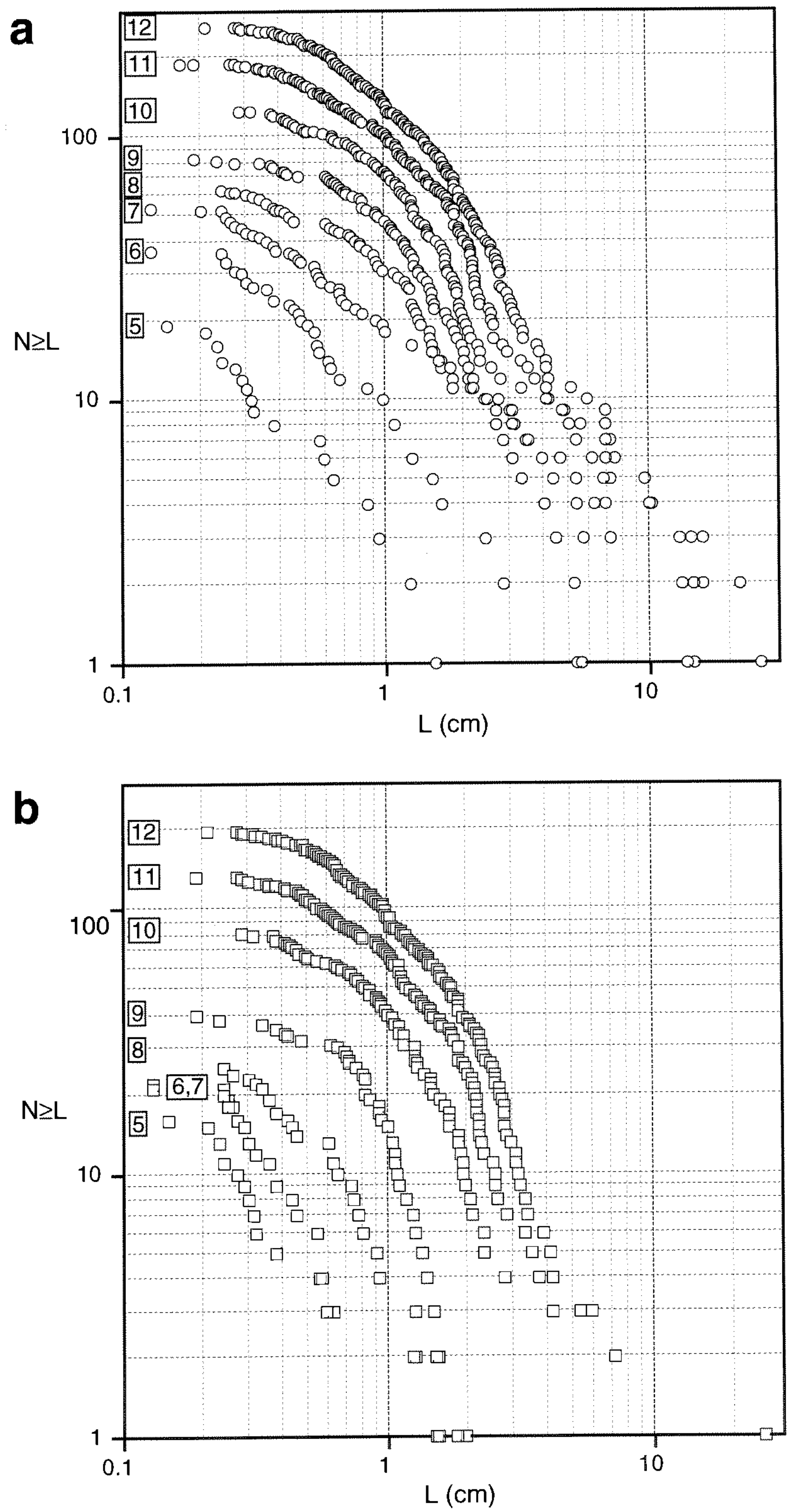

Figure 4.23: Cumulative frequency analysis of fault lengths for time steps 5 - 12 before (a) and after (b) faults believed to be related to edge effects are parsed from the data. Parsing appears to generally degrade the plots, although the degradation decreases with time. The change from a power-law to exponential distribution of fault sizes is still apparent.

REFERENCES CITED

Abrahams, A.D., 1985, Lithologic control of bedrock meander dimensions in the Appalachian Valley and Ridge Province: A comment: Earth Surface Processes and Landforms, v. 10, p. 635-638.

Ackermann, R.V., Schlische, R.W., and Young, S.S., 1995, Anti-clustering of microfaults around larger normal faults: Differential strain accommodation in the Danville basin: Eos-American Geophysical Union Transactions, v. 76, n. 46 (supplement), p. 574.

Ackermann, R.V., Johnson, L.A., Patiño, L.C., Schlische, R.W., 1996, Fracture partitioning in the Cow Branch Formation, Danville rift basin: Influence of mechanical stratigraphy on Mohr-Coulomb failure: Geological Society of America Abstracts with Programs, v. 28, n. 3, p. 33.

Ackermann, R.V., and Schlische, R.W., 1997, Anticlustering of small normal faults around larger faults: Geology, *in review.*

Ackermann, R.V., Schlische, R.W., Patiño, L.C., Johnson, L.A., and Young, S.S., 1997, A Lagerstätte of rift-related tectonic structures from the Solite Quarry, Dan River/Danville rift basin: *in* LeTourneau, P.M., and Olsen, P.E. (eds.), *Triassic-Jurassic Rift Basin Geoscience Conference Special Volume,* Columbia University Press,*in review.*

Ashley, G.M., and Renwick, W.H., 1982, Channel geometry, flow characteristics, and sediment transport in a bed-rock floored river: Geological Society of America Abstracts with Programs, v. 14, p. 435.

Ashley, G.M., and Renwick, W.H., 1983, Channel morphology and process at the riverine-estuarine transition, the Raritan River, New Jersey: Special Publications of the International Association of Sedimentologists, v. 6, p. 207-218.

Baker, V.R., 1984, Flood sedimentation in bedrock fluvial systems, *in* Koster, E.H., and Steel, R.J., (eds.), 1984, *Sedimentology of Gravels and Conglomerates*: Canadian Society of Petroleum Geologists Memoir 10, p. 87-98.

Barientos, S.E., Stein, R.S., and Ward, S.N., 1987, Comparison of the 1959 Hebgen Lake, Montana, and the 1983 Borah Peak, Idaho, earthquakes from geodetic observations: Seismological Society of America Bulletin, v. 77, p. 784-808.

Barnett, J.A.M., Mortimer, J., Rippon, J.H., Walsh, J.J., and Watterson, J., 1987, Displacement geometry in the volume containing a single normal fault: American Association of Petroleum Geologists Bulletin, v. 71, p. 925-937.

Braun, D.D., 1983, Lithologic control of bedrock meander dimensions in the Appalachian Valley and Ridge Province: Earth Surface Processes and Landforms, v. 8, p. 223-237.

Brownlow, A.H., 1979, Geochemistry: Prentice Hall, 498 p.

Burbank, D.W., Leland, J., Fielding, E., Anderson, R.S., Brozovic, N., Reid, M.R., and Duncan, C., 1996, Bedrcok incision, rock uplift and threshhold hillslopes in ths northwestern Himalayas: Nature, v. 379, p. 505-510.

Canavan, W.A., and Kochel, R.C., 1990, Statistical applications to channel morphology for a bedrock stream in central Vermont: Geological Society of America Abstracts with Programs, v. 22 (7), p. 110.

Cartwright, J.A., Trudgill, B.D., and Mansfield, C.S., 1995, Fault growth by segment linkage: an explanation for scatter in maximum displacement and trace length data from the Canyonlands: Journal of Structural Geology, v. 17, p. 1319-1326.

Cladouhos, T.T., and Marrett, R., 1996, Are fault growth and linkage models consistent with power-law distributions of fault lengths?: Journal of Structural Geology, v. 18, p. 281-294.

Cloos, E., 1955, Experimental analysis of fracture patterns: Bulletin of the geological Society of America, v. 66, p. 241-256.

Cloos, E., 1968, Analysis of Gulf Coast fracture patterns: American Association of Petroleum Geologists Bulletin, v. 52, 420-444.

Cloos, H., 1929, Kunstische Gebirge I: Natur und Museum, v. 59, p. 225-243.

Cowie, P. A., and Scholz, C. H., 1992a, Displacement-length scaling relationship for faults: data synthesis and discussion: Journal of Structural Geology, v. 14, p. 1149-1156.

Cowie, P. A., and Scholz, C. H., 1992b, Physical explanation for displacement-length relationship of faults using a post-yield fracture mechanics model: Journal of Structural Geology, v. 14, p. 1133-1148.

Cowie, P.A., Scholz, C.H., Edwards, M., and Malinverno, A., 1993, Fault strain and seismic coupling on mid-ocean ridges: Journal of Geophysical Research, v. 98, p. 17,911-17,920.

Cowie, P.A., Vanneste, C., and Sornette, D., 1993, Statistical physics model for the spatiotemporal evolution of faults: Journal of Geophysical Research, v. 98, p. 21,809-21,821.

Cowie, P.A., Malinverno, A., Ryan, W.B.F., and Edwards, M.H., 1994, Quantitative fault studies on the East Pacific Rise: A comparison of sonar imaging techniques: Journal of Geophysical Research, v. 99, no. B8, p. 15205-15218.

Cowie, P.A., Sornette, D., and Vanneste, C., 1995, Multifractal scaling properties of a growing fault population: Geophysical Journal International, v. 122, p. 457-469.

Cowie, P.A., Knipe, R., and Main, I.G., 1996, Introduction to the special issue (Scaling Laws for Fault and Fracture Populations—Analyses and Applications): Journal of Structural Geology, v. 18, p. v. to xi.

Das, S., and Scholz, C., 1982, Off-fault aftershock clusters caused by shear stress increase?: Seismological Society of America Bulletin, v. 71, p. 1669-1675.

Davis, G.H., 1984, Structural Geology of Rocks and Regions: Wiley, 492 p.

Dawers, N.H., Anders, M.H., and Scholz, C.H., 1993, Growth of normal faults: Displacement-length scaling: Geology, v. 21, p. 1107-1110.

Dawers, N.H., and Anders, M.H., 1995, Displacement-length scaling and fault linkage: Journal of Structural Geology, v. 17, 607-614

Dawers, N.H., and Anders, M.H., 1997, Fault size distribution on the Volcanic Tableland, California: Implications for the small-scale fault contribution to total strain: Journal of Structural Geology, *in review*.

Dawers, N.H., and Malinverno, A., 1997, Fault size distribution on the Volcanic Tableland, California: Implications for the small-scale fault contribution to total strain: Journal of Structural Geology, *in review*.

Dolan, R.E., Howard, A., and Trimble, D., 1978, Structural control on rapids and pools in Colorado River in the Grand Canyon: Science, v. 202, p. 629-631.

Dunne, W.M., and Hancock, P.L., 1994, Paleostress analysis of small-scale brittle structures: *in Continental Deformation*, P.L. Hancock, ed., Pergamon, p. 101-120.

Eisenstadt, G., Vendeville, B.C., and Withjack, M.O., 1995, Introduction to experimental modeling of tectonic processes, Geological Society of America short course manual, Denver, USA, 110 p.

Elliott, D., 1976, Energy balance and deformation mechanisms of thrust sheets: Philosophical Transactions, Royal Society of London, v. A283, p. 289-312.

Feigenson, M.D., and Carr, M.J., 1985, Determination of major, trace, and rare-earth elements in rocks by DCP-AES: Chemical Geology, v. 51, p. 19-27.

Fisher, J.J, Frohlich, R.K., Savarese, J.G., and Mulhare, M.J., 1988, Hydrocarbon contamination beneath glacial till in bedrock wells detected by hydrogeology, remote sensing and geophysical techniques, *in* Symposium Proceedings of the International Conference on Fluid Flow in Fractured Rocks: Georgia State University, Atlanta, GA, p. 501-513.

Frasier, N.C., Grimaldi, D.A., Olsen, P.E., and Acsmith, B., 1996, A Triassic Lagerstätte from eastern North America: Nature, v. 380, p. 615-619.

Gibson, J.R., Walsh, J.J., and Watterson, J., 1989, Modelling of bed contours and cross-sections adjacent to planar normal faults: Journal of Structural Geology, v. 11, p. 317-328.

Gillespie, P. A., Walsh, J. J., and Watterson, J., 1992, Limitations of dimension and displacement data from single faults and the consequences for data analysis and interpretation: Journal of Structural Geology, v. 14, p. 1157-1172.

Gillespie, P.A., Howard, C.B., Walsh, J.J., and Watterson, J., 1993, Measurement and characterisation of spatial distributions of fractures: Tectonophysics, v. 226, p. 113-141.

Gordon, N.D., McMahon, T.A., and Finlayson, B.L., 1992, Stream Hydrology: An Introduction for Ecologists: John Wiley and Sons, New York, 526 pp.

Gross, M.R., 1993a, The effects of mechanical stratigraphy on failure mode and fracture spacing in the Monterey Formation of coastal California (unpublished PhD thesis): University Park, Pennsylvania, The Pennsylvania State University, 183 p.

Gross, M.R., 1993b, The origin and spacing of cross joints: examples from the Monterey Formation, Santa Barbara Coastline, California: Journal of Structural Geology, v. 15, p. 737-751.

Gross, M.R., 1995, Fracture partitioning: Failure mode as a function of lithology in the Monterey Formation of Coastal California: Geological Society of America Bulletin, v. 107, p. 779-792.

Gross, M.R., Fischer, M.P., Engelder, T., and Greenfield, R.J., 1995, Factors controlling joint spacing in interbedded sedimentary rocks: integrating numerical models with field observations from the Monterey Formation, USA: *in* Ameen, M.S. (*ed.*), *Fractography: fracture topography as a tool in fracture mechanics and stress analysis*: Geological Society Special Publication No. 92, p. 215-233.

Gross, M.R., Becker, A., and Gutiérrez-Alonso, G., 1997, Transfer of displacement from multiple slip zones to major detachment in an extensional regime: Example from the Dead Sea Rift, Israel: Geological Society of America Bulletin: *in press.*

Gross, M.R., Gutiérrez-Alonso, G., Bai, T., Wacker, M.A., and Collinsworth, K.B., 1997b, Influence of mechanical stratigraphy and kinematics on fault scaling relations: Journal of Structural Geology, v. 19, p. 171-183.

Gupta, A., and Scholz, C.H., 1996, Three-dimensional geometry of small normal faults: Geological Society of America Abstracts with Programs, v. 28, no. 3, p. 60-61.

Gupta, A., and Scholz, C.H., 1996, Validity of Elastic Models in Predicting Fault Displacement Fields: Eos-American Geophysical Union Transactions, v. 77, n. 46 (supplement), p. 484.

Harden, D.R., 1985, The distribution and geometry of incised river meander in the central Colorado plateau: Geological Society of America Abstracts with Programs, v. 14 (7), p. 407.

Herman, G.C., 1996, Structural analyses of pre-Cretaceous bedrock geology in the New Jersey region [Unpublished Ph.D. Dissertation]: Rutgers University, New Brunswick, NJ.

Hobbs, D.W., 1967, The formation of tension joints in sedimentary rocks: an explanation: Geological Magazine, v. 104, 550-556.

Horton, R.E., 1945, Erosional Development of streams and their drainage basins; Hydrophysical approach to quantitative morphology: Bulletin of the Geological Society of America, v. 56, p. 274-370.

Howard, A.D., 1967, Drainage analysis in geologic interpretation: A summation: The American Association of Petroleum Geologists Bulletin, v. 51, p. 2246-2259.

Howard, A.D., 1980, Thresholds in river regimes, *in Thresholds in Geomorphology*, Coates, D.R., and Vitek, J.D., eds., Allen and Unwin, Winchester, Mass., p. 227-258.

Howard, A.D., and Kerby, G., 1983, Channel changes in badlands: Geological Society of America Bulletin, v. 94, p. 739-752.

Howard, A.D., Dietrich, W.E., and Seidl, M.A., 1994, Modeling fluvial erosion on regional to continental scales: Journal of Geophysical Research, v. 99, No. B7, p. 13,971-13,986.

Hubbert, M.K., 1937, Theory of scale models as applied to the studies of geologic structures: Geological Society of America Bulletin, v. 48, p. 1459-1520.

Jackson, J.A., and White, N.J., 1989, Normal faulting in the upper continental crust: observations from regions of active extension: Journal of Structural Geology, v. 11, p. 15-36.

Johnson, G.A., 1988, Detailed mapping of groundwater flow in an anisotropic crystalline bedrock formation, *in* Symposium Proceedings of the International Conference on Fluid Flow in Fractured Rocks: Georgia State University, Atlanta, GA, p. 85-100.

Jones, B.D., 1994, Structure and Stratigraphy of the Hopewell Fault Block, Newark Basin, New Jersey and Pennsylvania [Unpublished M.S. Thesis]: Rutgers University, New Brunswick, NJ.

Kakimi, T., 1980, Magnitude-frequency relation for displacement of minor faults and its significance in crustal deformation: Bulletin of the Geological Survey of Japan, v. 31, p. 467-487.

Kent, D.V., and Olsen, P.E., 1997, Magnetostratigraphy and paleopoles from the Late Triassic Dan River-Danville basin: Interbasin correlation of continental sediments and a test of the tectonic coherence of New rift basins in eastern North America: Geological Society of America Bulletin, *in press*.

King, G.C.P., Stein, R.S., and Rundle, J.B., 1988, The growth of geological structures by repeated earthquakes; 1. conceptual framework: Journal of Geophysical Research, v. 93, p. 13307-13318.

Krantz, R. W., 1988, Multiple fault sets and three-dimensional strain: Journal of Structural Geology, v. 10, p. 225-237.

Ladeira, F.L., and Price, N.J., 1981, Relationships between fracture spacing and bed thickness: Journal of Structural Geology, v. 3, p. 179-183.

Larsen, P.H., 1988, Relay structures in a Lower Permian basement-involved extension system, East Greenland: Journal of Structural Geology, v. 10, p. 3-8.

Lama, R.D., and Vutukuri, V.S., 1978, Handbook on Mechanical Properties of Rock Testing Techniques and Results: Series on Rock and Soil Mechanics II & III, Trans Tech Clausthal.

Little, T.A., 1996, Faulting-related displacement gradients and strain adjacent to the Awatere strike-slip fault in New Zealand: Journal of Structural Geology, v. 18, p. 321-340.

Lyttle, P.T., and Epstein, J.B., 1987, Geologic map of the Newark 1° x 2° quadrangle, New Jersey, Pennsylvania, and New York: United States Geologic Survey Map I-1715.

Main, I., 1996, Statistical physics, seismogenesis, and seismic hazard: Reviews of Geophysics, v. 34, p. 433-462.

Malinconico, 1996, Paleo-maximum thermal structure of the Triassic Taylorsville (Virginia) basin: evidence for border fault convection and implications for duration of syn-rift sedimentation and long-term elevated heat flow, *in* LeTourneau, P.M., and Olsen, P.E., (eds.), *Aspects of Triassic-Jurassic Rift Basin Geoscience*: State Geological and Natural History Survey of Connecticut Miscellaneous Reports 1, p. 25-26.

Malinverno, A., 1997, On the power law size distribution of turbidite beds: Basin Research, *in review*.

Marrett, R., and Allmendinger, R.W., 1991, Estimates of strain due to brittle faulting: sampling fault populations: Journal of Structural Geology, v. 13, p. 735-738.

Marrett, R., and Allmendinger, R. W., 1992, Amount of extension on "small" faults: An example from the Viking graben: Geology, v. 20, p. 47-50.

McClay, K.R., 1996, Recent advances in analogue modelling: uses in section interpretation and validation, *in* Buchanan, P.G., and Nieuwland, D.A., (eds.), *Modern developments in structural interpretation, validation and modelling*: Geological Society Special Publication 99, p. 201-225.

McGrath, A., 1992, Fault propagation and growth; A study of the Triassic and Jurassic from Watchet and Kilve, North Somerset [M.Sc. thesis]: London, Royal Holloway, University of London.

McMillan, R. A., 1975, The orientation and sense of displacement of strike-slip faults in continental crust [B.S. thesis]: Ottawa, Ontario, Carleton University.

Miller, J.R., 1991, The influence of bedrock geology on knickpoint development and channel-bed degradation along downcutting streams in south-central Indiana: Journal of Geology, v. 99, p. 591-605.

Muraoka, H., and Kamata, H., 1983, Displacement distribution along minor fault traces: Journal of Structural Geology, v. 5, p. 483-495.

Muszala, S., 1996, Seismic Refraction Study of a Portion of the Newark Basin, Rutgers University, Busch Campus, Piscataway, New Jersey [Unpublished Senior Honors Thesis]: Rutgers University, New Brunwick, NJ.

Narr, W., and Suppe, J., 1991, Joint spacing in sedimentary rocks: Journal of Structural Geology, v. 13, p. 1037-1048.

Nelson, J.W., 1988, Influence of joints and fractures upon the hydrogeology of a karst terrain, *in* Symposium Proceedings of the International Conference on Fluid Flow in Fractured Rocks: Georgia State University, Atlanta, GA, p. 432-446.

Nicol, A., Walsh, J.J., Watterson, J.,Gillespie, P.A., 1996, Fault size distributions - are they really power-law?: Journal of Structural Geology, v. 18, p. 191-199.

Nicol, A., Watterson, J., Walsh, J.J., and Childs, C., 1996, The shapes, major axis orientations and displacement patterns of fault surfaces: Journal of Structural Geology, v. 18, p. 235-248.

Peacock, D. C. P., 1991, Displacements and segment linkage in strike-slip fault zones: Journal of Structural Geology, v. 13, p. 1025-1035.

Peacock, D.C.P., and Sanderson, D.J., 1991, Displacements, segment linkage, and relay ramps in normal fault zones: Journal of Structural Geology, v. 13, p. 721-733.

Pickering, G., Bull, J.M., and Sanderson, D.J., 1995, Sampling power-law distributions: Tectonophysics, v. 248, p. 1-20.

Pollard, D.D., and Aydin, A., 1988, Progress in understanding jointing over the past century: Geological Society of America Bulletin, v. 100, p. 1181-1204.

Olsen, P.E., Kent, D.V., Cornet, B., Witte, W.K., and Schlische, R.W., 1996, High-resolution stratigraphy of the Newark rift basin (early Mesozoic, eastern North America): Geological Society of America Bulletin, v. 108, p. 40-77.

Olsen, P.E., Schlische, R.W., and Gore, P.J.W., eds, 1989, Tectonic, depositional, and paleoecological history of early Mesozoic rift basins, eastern North America: International Geological Congress Field Trip T-351, Washington, D.C., American Geophysical Union, 174 p.

Opheim, J. A., and Gudmundsson, A., 1989, Formation and geometry of fractures, and related volcanism, of the Krafla fissure swarm, northeast Iceland: Geological Society of America Bulletin, v. 101, p. 1608-1622.

Orabone, K.D., *(in prep).*, 1997, Fracture Patterns in Newark Basin Bedrock and Their Relationship to Groundwater Flow [M.S. thesis]: Rutgers University, New Brunswick, NJ.

Rives, T., Razack, M., Petit, J.P., and Rawnsley, K.D., 1992, Joint spacing: analogue and numerical simulations: Journal of Structural Geology, v. 14, p. 925-937.

Schlische, R.W., 1990, Aspects of the Structural and Stratigraphic Evolution of Early Mesozoic Rift Basins of Eastern North America [Unpublished Ph.D. Dissertation]: Columbia University, New York City, NY.

Schlische, R.W., 1991, Half-graben basin filling models: new constraints on continental extensional basin development: Basin Research, v. 3, p. 123-141.

Schlische, R.W., 1992, Structural and stratigraphic development of the Newark extensional basin, eastern North America; Implications for the growth of the basin and its bounding structures: Geological Society of America Bulletin, v. 104, p. 1246-1263.

Schlische, R.W., 1993, Anatomy and evolution of the Triassic-Jurassic continental rift system, eastern North America: Tectonics, v. 12, p. 1026-1042.

Schlische, R.W., 1995, Geometry and Origin of fault-related folds in extensional settings: American Association of Petroleum Geologists Bulletin, v. 79, p. 1661-1678

Schlische, R.W., Young, S.S., Ackermann, R.V., and Gupta, A., 1996, Geometry and scaling relations of a population of very small rift-related normal faults: Geology, v. 24, p. 683-686.

Schlische, R.W., 1997, Progress in Understanding the Structural Geology, Basin Evolution, and tectonic History of the Eastern North American Rift System: *in* LeTourneau, P., and Olsen, P.E., (eds.), *Triassic-Jurassic Rift Basin Geoscience Conference Special Volume,* Columbia University Press,*in review.*

Scholz, C. H., 1990, The mechanics of earthquakes and faulting: New York, Cambridge University Press, 439 p.

Scholz, C. H., and Cowie, P. A., 1990, Determination of total strain from faulting using slip measurements: Nature, v. 346, p. 837-838.

Scholz, C.H., Dawers, N.H., Yu., J.-J., Anders, M.A., and Cowie, P.A., 1993, Fault growth and fault scaling laws: preliminary results: Journal of Geophysical Research, v. 85, p. 21,951-21,961.

Schumm, S.A., Mosley, M.P., and Weaver, W.E., 1987, Experimental Fluvial Geomorphology: John Wiley, New York, p. 225-251.

Seidl, M.A., and Dietrich, W.E., 1992, The problem of channel erosion into bedrock: CATENA Supplement 23, p. 101-124.

Seidl, M.A., Dietrich, W.E., and Kirchner, J.W., 1994, Longitudinal profile development into bedrock: An analysis of Hawaiian channels: Journal of Geology, v. 102, p. 457-474.

Seidl, M.A., Finkel, R.C., Caffee, M.W., Hudson, G.B., and Dietrich, W.E., 1997, Cosmogenic isotope analysis applied to river longitudinal profile evolution: Problems and interpretations: Earth Surface Processes and Landforms, v. 22, p. 195-209.

Seidl, M.A., 1998, Directions in bedrock channel research: Past, Present, and Future: *in prep.*

Shepard, R.G., and Schumm, S.S., 1974, Experimental study of river incision: Geological Society of America Bulletin, v. 85, p. 257-268.

Sims, D., 1993, The rheology of clay: a modeling material for geologic structures: Eos-American Geophysical Union Transactions, v. 74, n. 46 (supplement), p. 569.

Steele, W.M., Atkins, R.L., Brackett, D.A., and Schmitt, T.J., 1988, Orientations of fractures measured from sonic televiewer logs of selected crystalline-rock wells in the Piedmont and Blue Ridge physiographic provinces of Georgia, *in* Symposium Proceedings of the International Conference on Fluid Flow in Fractured Rocks: Georgia State University, Atlanta, GA, p. 162-187.

Stewart, I.S., and Hancock, P.L., 1994, Neotectonics: *in Continental Deformation*, P.L. Hancock, ed., Pergamon, p. 370 - 410.

Suppe, J., 1985, Principles of Structural Geology: Prentice Hall, 537 p.

Swan, A.R.H., and Sandilands, M., 1995, Introduction to Geological Data Analysis: Blackwell Science, Oxford, 446 p.

Trudgill, B., and Cartwright, J., 1994, Relay-ramp forms and normal fault linkages, Canyonlands National Park, Utah: Geological Society of America Bulletin, v. 106, p. 1143-1157.

Vermilye, J., 1996, The growth of faults and fractures [unpublished Ph.D. thesis]: Columbia University, New York.

Villemin, T, Angelier, J., and Sunwoo, C., 1995, Fractal distribution of fault length and offsets: Implications of brittle deformation evaluation—Lorraine Coal Basin: *in* Barton, C.C. and La Pointe, P.R. (eds.), *Fractals in the earth sciences*, New York, Plenum Press, p. 205-226.

Walsh, J. J., and Watterson, J., 1987, Distributions of cumulative displacement and seismic slip on a single normal fault surface: Journal of Structural Geology, v. 9, p. 1039-1046.

Walsh, J. J., and Watterson, J., 1988, Analysis of the relationship between displacements and dimensions of faults: Journal of Structural Geology, v. 10, p. 239-247.

Watterson, J., 1986, Fault dimensions, displacement, and growth: Pure and Applied Geophysics, v. 124, p. 365-373.

Watterson, J., Walsh, J. J., Gillespie, P. A., and Easton, S., 1996, Scaling systematics of fault sizes on a large scale range fault map: Journal of Structural Geology, v. 18, p. 199-214.

Withjack, M.O., and Jamison, W.R., 1986, Deformation produced by oblique rifting: Tectonophysics, v. 126, p. 99-124.

Withjack, M.O., Schlische, R.W., and Olsen, P.E., 1997, Inversion and fill-in-the-blank: AAPG Bulletin, *in press*.

Wolman, M.G., Church, M., Newbury, R., Lapointe, M., Frenette, M., Andrews, E.D., Lisle, T.E., Buchanan, J.P., Schumm, S.A., and Winkley, B.R., 1990, The riverscape, *in* Wolman, M.G., and Riggs, H.C., (eds.), *Surface Water Hydrology*: Geological Society Decade of North American Geology Series, vol. O-1: Boulder, Geological Society of America, p. 281-328.

Wohl, E.E., 1990, Bedrock benches and boulder bars: Floods in the Burdekin Gorge of northeastern Australia: Geological Society of America Abstracts with Programs, v. 22 (7), p. 110.

Wohl, E.E., 1992, Bedrock benches and boulder bars: Floods in the Burdekin Gorge of Australia: Geological Society of America Bulletin, v. 104, p. 770-778.

Wohl, E.E., 1993, Bedrock channel incision along Piccaninny Creek, Australia: Journal of Geology, v. 101, p. 749-761.

Wohl, E.E., Greenbaum, N., Schick, A.P., and Baker, V.R., 1994, Controls on bedrock channel incision along Nahal Paran, Israel: Earth Surface Processes and Landforms, v. 19, p. 1-13.

Wohl, E.E., Greenbaum, N., Schick, A.P., and Baker, V.R., 1994, Controls on bedrock channel incision along Nahal Paran, Israel: Earth Surface Processes and Landforms, v. 19, p. 1-13.

Wojtal, S.F., 1994, Fault scaling laws and the temporal evolution of fault systems: Journal of Structural Geology, v. 16, p. 603-612.

Wojtal, S.F., 1996, Changes in fault displacement populations correlated to linkage between faults: Journal of Structural Geology, v. 18, p. 265-279.

Yelderman, J.C., Jr., Barrett, D.P., and Barquest, B.A., 1988, The effects of structures and weathering fractures on shallow ground water systems, *in* Symposium Proceedings of the International Conference on Fluid Flow in Fractured Rocks: Georgia State University, Atlanta, GA, p. 487-500.

Zernitz, E.R., 1932, Drainage patterns and their significance: Journal of Geology, v. 40, p. 498-521.

CURRICULUM VITAE

Education
- Ph.D. in Geological Sciences, Rutgers University, October 1997
- M.S. in Geological Sciences, Rutgers University, October 1994
  - Thesis: "Effects of Sustained Elevated Discharges from Intrabasin Flow Diversion on the Fluvial Geomorphology of East Branch Perkiomen Creek, Bedminster, Pennsylvania", 202 p.
- B.S. in Geology (with college honors), Dickinson College, May 1992
  - Concentrations in Philosophy and German
  - Senior Honors Thesis: "An Examination of the Factors Governing the Development of Karst Topography in the Cumberland Valley of Pennsylvania", 110 p.

Positions held
- Geologist Intern with the Structural and Stratigraphic Process Group, Mobil Exploration and Producing Technical Center, Dallas, TX; June - December 1996
- Teaching Assistant for Introductory Geology, Structural Geology, and Field Geology, Rutgers University: 1992 - 1997
- Assistant Network (Macintosh) Administrator, Department of Geological Sciences, Rutgers University: May 1995 - June 1996
- Assistant Geologist, Roy F. WESTON Inc., Edison, NJ: 1992 - 1993

Journal Articles
Ackermann, R.V., and Schlische, R.W., 1997, Anticlustering of small normal faults around larger faults: Geology, in press.

Ackermann, R.V., Schlische, R.W., Patiño, L.C., Johnson, L.A., and Young, S.S., 1997, A Lagerstätte of rift-related tectonic structures from the Solite Quarry, Dan River/Danville rift basin: Triassic-Jurassic Rift Basin Geoscience Conference Special Volume, Columbia University Press, in review.

Schlische, R.W., and Ackermann, R.V., 1997, Integrating Computers into the Field Geology Curriculum: Journal of Geoscience Education, in review.

Schlische, R.W., Young, S.S., Ackermann, R.V., and Gupta, A., 1996, Geometry and scaling relations of a population of very small rift-related normal faults: Geology, v. 24, p. 683-686.

Ackermann, R.V., Schlische, R.W., and Olsen, P.E., 1995, Synsedimentary collapse of portions of the lower Blomidon Formation, Fundy rift basin, Nova Scotia: Canadian Journal of Earth Sciences, v. 32, p. 1965-1976.

Schlische, R.W., and Ackermann, R.V., 1995, Kinematic significance of sediment-filled fissures in the Fundy Basin, Canada: Journal of Structural Geology, v. 17, p. 987-996.

Manuscripts in preparation
Ackermann, R.V., Schlische, R.W., and Withjack, M.O., 1997, Systematics of an evolving population of normal faults, *for Journal of Structural Geology.*

Ackermann, R.V., Seidl, M.A., and Schlische, R.W., 1997, First-order structural controls on modern drainage networks of the Mesozoic Newark rift basin, *for Journal of Geology.*

Field guides/Other
Potter, N. Jr., Ackermann, R.V., and others, 1992, Stream Meanders in Carlisle, Pennsylvania: Studies in Geology, Dickinson College, v. 2, 31 p.

Potter, N., Hanson, H., Ackermann, R.V., Dokter, G.N., Lev, S., Pezzoli, L., and Troy, T., 1991, Analysis of in-situ strain indicators in the Weverton conglomerate at

Hammond's Rocks: Field Guide, 56th Annual Field Conference of Pennsylvania Geologists, p. 193-214.

Abstracts

Ackermann, R.V., Seidl, Michele A., and Schlische, Roy W., 1997, First-order regional structural controls on modern drainage networks within the Newark rift basin, New Jersey: Geological Society of America Abstracts with Programs, v. 29, v. 19, n. 1, p. 25.

Schlische, R.W., and Ackermann, R.V., 1997, Geometry, scaling laws, and spatial distribution of small tectonic normal faults, Danville rift basin, North Carolina and Virginia: 36th U.S. Rock Mechanics Symposium, June 29 - July 2, 1997, New York, NY, *in press*.

Ackermann, R.V., Schlische, R.W., Patiño, L.C., Johnson, L.A., and Young, S.S., 1996, Deformation within the Solite Quarry, Danville basin: Small normal faults, fracture partitioning, and the spatial-temporal evolution of normal fault systems: Triassic-Jurassic Rift Basin Geoscience Conference, November 9 - 10, 1996, Rocky Hill, CT: State Geological and Natural History Survey of Connecticut, Hartford, Connecticut, Miscellaneous Reports 1, p. 1.

Ackermann, R.V., Johnson, L.A., Patiño, L.C., Schlische, R.W., 1996, Fracture partitioning in the Cow Branch Formation, Danville rift basin: Influence of mechanical stratigraphy on Mohr-Coulomb failure: Geological Society of America Abstracts with Programs, v. 28, n. 3, p. 33.

Schlische, R.W., and Ackermann, R.V., 1996, From field data collection to final map: Integrating computers into the Field Geology curriculum: Geological Society of America Abstracts with Programs, v. 28, n. 3, p. 97.

Ackermann, R.V., Schlische, R.W., and Young, S.S., 1995, Anti-clustering of microfaults around larger normal faults: Differential strain accommodation in the Danville basin: Eos-American Geophysical Union Transactions, v. 76, n. 46 (supplement), p. 574.

Schlische, R.W., Young, S.S., and Ackermann, R.V., 1995, Geometry and scaling relations of a population of rift-related normal faults: Eos-American Geophysical Union Transactions, v. 76, n. 46 (supplement), p. 574.

Ackermann, R.V., Schlische, R.W., and Olsen, P.E., 1995, Evaporite dissolution and associated collapse features of the Fundy basin: Paleoenvironmental implications: Geological Society of America Abstracts with Programs, v. 27, No.1, p. 25.

Schlische, R.W., and Ackermann, R.V., 1995, Rift basin inversion around the margins of the North Atlantic: Implications for the age of initiation of sea-floor spreading: Geological Society of America Abstracts with Programs, v. 27, No.1, p. 80.

Young, S. S., Schlische, R.W., and Ackermann, R.V., 1995, Micro-normal fault populations in Mesozoic rift basins: Length displacement scaling relations:Geological Society of America Abstracts with Programs, v. 27, No. 1, p. 94.

Ackermann, R.V., Ashley, G.M., and Schlische, R.W., 1994, Response of a bedrock-influenced river to sustained elevated discharge: Anthropogenic induced change: Geological Society of America Abstracts with Programs, v. 26, No. 7, p. 234.

Ackermann, R.V., and Ashley, G.M., 1994, Channel response to sustained elevated discharge: East Branch Perkiomen Creek, Bedminster, Pennsylvania: Geological Society of America Abstracts with Programs, v. 26, No. 3, p. 1.

Ackermann, R.V., Schlische, R.W., and Olsen, P.E., 1993, Triassic buried interstratal karst, Fundy Basin, Nova Scotia, Canada: Geological Society of America Abstracts with Programs, v. 25, No. 6, p. 69.

Ackermann, R.V., 1993, An examination of the factors governing the development of karst topography in the Cumberland Valley of Pennsylvania: Geological Society of America Abstracts with Programs, v. 25, No. 2, p. 1.